

Study of High-Energy Emission from High Mass X-ray Binaries

Samuel Mc Keague, BSc

Supervised by Prof Masha Chernyakova




A thesis presented for the degree of Doctor of Philosophy

SCHOOL OF PHYSICAL SCIENCES
DUBLIN CITY UNIVERSITY

January 2022

Declaration

I hereby certify that this material, which I now submit for assessment on the programme of study leading to the award of Ph.D. degree is entirely my own work, and that I have exercised reasonable care to ensure that the work is original, and does not to the best of my knowledge breach any law of copyright, and has not been taken from the work of others save and to the extent that such work has been cited and acknowledged within the text of my work.

Signed: 

ID No.: 13313491

Date: Tuesday 4th January, 2022

Dedication

I wish to dedicate my thesis to all my friends and family who have supported me over the course of my research.

To my mum and dad Trish and George, my sister Beth and my friend Dylan who put up with me during my most stressful periods while at home during the Covid pandemic. To my friends who provided me comfort and showed understanding and patience on all the game nights and Zoom chats I missed.

And finally to all my fellow postgraduate students, who experience the same fears and concerns on the most stressful days but push hard to cross the finish line.

Acknowledgements

This research project was made possible by funding from the ESA PRODEX. I want to give special thanks to Prof. Masha Chernyakova for her continuing support and guidance over the course of my research.

Thanks to Dr. Denys Malyshev for his advice, assistance and support on my work conducting analysis of Fermi-LAT data.

Thanks to Prof. Joern Wilms, Dr. Thomas Dauser, Maximilian Lorenz, the SIXTE team and the XIFU consortium for their support on my research with Athena XIFU.

Thanks to Dr. Alicia López Oramas, the CTA Galactic Transients work group and the CTA consortium for their help and for allowing me to participate in the research of CTA.

The work presented here on analysis of data from Fermi-LAT was made possible with the support of the Irish Centre for High-End Computing (ICHEC) and the access provided to Fionn and Kay.

This research has made use of the SIXTE software package (Dauser et al., 2019) provided by ECAP/Remeis observatory (<https://github.com/thdauser/sixte>).

This research made use of ctools, a community-developed analysis package for Imaging Air Cherenkov Telescope data. ctools is based on GammaLib, a community-developed toolbox for the scientific analysis of astronomical gamma-ray data. This research has made use of the CTA instrument response functions provided by the CTA Consortium and Observatory.

Publications & Presentations

- Chernyakova, M., Malyshev, D., Mc Keague, S., et al. 2020, New insight into the origin of the GeV flare in the binary system PSR B1259-63/LS 2883 from the 2017 periastron passage, *Monthly Notices of the Royal Astronomical Society*, 497, 648–655.
- Chernyakova, M., Malyshev, D., van Soelen, B., et al. 2021, Multi-wavelength properties of the 2021 periastron passage of PSR B1259-63, *Universe. Papers:*
- López-Oramas, A. et al. 2021. Prospects for Galactic transient sources detection with the Cherenkov Telescope Array, 37th International Cosmic Ray Conference (ICRC2021).
- Bošnjak, Ž. et al. 2021, Multi-messenger and transient astrophysics with the Cherenkov Telescope Array, arxiv: 2106.03621.
- López-Oramas, A. et al. Galactic Transient Sources with the Cherenkov Telescope Array. Writing in Progress.
- Presented at the 9th XIFU Consortium Meeting on the 15th April 2019. Irish Contributions to X-IFU Simulations.
- Presented at the Irish National Astronomers Meeting (INAM) on the 4th September 2019. Simulated spectra of the high-mass X-ray binary Vela X-1 with Athena X-IFU.
- Participated in the DCU Postgraduate BOC Poster Competition 2019.
- Participated in the DCU Postgraduate BOC Poster Competition 2020.

Contents

Abstract	1
1 Introduction: High Mass X-ray Binaries	2
1.1 Accretion	4
1.1.1 Roche-lobe Overflow	7
1.1.2 Stellar Wind Accretion	9
1.1.3 Be Star Binaries	11
1.2 Physical Processes in HMXBs	12
1.2.1 Wind Collisions & Bow Shocks	12
1.2.2 Radiation-Driven Stellar Winds	14
1.3 Microquasars	16
1.4 Gamma-ray Binaries	17
1.5 Summary & Discussion	19
2 Radiation Processes of High Mass X-ray Binaries	20
2.1 Synchrotron	21
2.2 Inverse Compton	23
2.3 Bremsstrahlung	25
2.3.1 Thermal Bremsstrahlung	26
2.3.2 Relativistic Bremsstrahlung	27
2.3.3 Bremsstrahlung Cooling	27
2.4 Summary & Discussion	28
3 Telescopes and Future Missions	29
3.1 Fermi Gamma-ray Space Telescope	30
3.2 Athena X-ray Telescope	33
3.3 Cherenkov Telescope Array	35
3.4 Data Analysis Software	39
3.4.1 Fermitools	39
3.4.2 SIXTE	40
3.4.3 CTOOLS	41
3.5 Summary & Discussion	41
4 Fermi Analysis of PSR B1259-63	43
4.1 PSR B1259-63	43
4.2 2017 Periastron Analysis	46
4.2.1 Modelling Fermi-LAT Data	46
4.2.2 Discussion of 2017 Modelling	52
4.2.3 Summary and Conclusions	59

4.3	2021 Periastron Observations	59
4.3.1	Discussion of 2021 Preliminary Results	60
4.3.2	Summary & Conclusions	61
5	Athena XIFU Simulations of Vela X-1	64
5.1	Vela X-1	65
5.2	X-IFU Simulations of Vela X-1	67
5.3	XSTAR Eclipse Simulations	71
5.3.1	XSTAR Emission Lines	71
5.3.2	Simulations of XSTAR Models	75
5.3.3	Revising XSTAR Model and Simulation Parameters	77
5.4	X-IFU Simulations Discussion	80
5.5	Summary & Conclusions	86
6	Sensitivity of CTA on HMXBs	88
6.1	SS433	88
6.1.1	GeV Detections with Fermi-LAT	89
6.1.2	TeV Detection with HAWC	89
6.2	CTA Simulations	90
6.3	Summary & Conclusions	95
7	Conclusions and Future Projects	96
7.1	New Insight of PSR B1259-63	96
7.2	Modelling Eclipsing HMXB with Athena X-IFU	97
7.3	Demonstration of the Sensitivity of CTA	98
A	Using XSTAR	100

List of Figures

1.1	Artist impression of a XRB, GRO J1655-40, where matter is directly accreted from the massive star onto the compact object (Credit: ESA, NASA, Felix Mirabel).	2
1.2	Simple illustration of the Roche lobe boundaries and intersection in XRBs.	6
1.3	Illustration of the Roche lobe boundaries where the donor star is overflowing the Roche lobe so matter is streamed to the compact object. This typically results in an accretion disc (Credit: Moscow Institute of Physics and Technology Press Office).	8
1.4	Illustration of stellar wind-fed accretion in HMXBs (Credit: Sara Bergenius).	9
1.5	Corbet diagram for NS showing three populations of HMXBs: (1) sgHMXB powered by wind-fed accretion. (2) sgHMXB where accretion is a result of filling the Roche-lobe. (3) HMXBs where the massive companion is a Be star with a disc (Chaty 2011).	12
1.6	Hubble Space Telescope image of the bow shock created in the Orion nebula by the collision of the stellar winds from LL Orionis and the nebula flow (Credit: NASA).	13
1.7	A diagram illustrating the principle behind line-driven stellar winds, where UV photons are absorbed by matter from stellar outflow and then re-emitted and this process repeats (Kudritzki & Puls 2000). . .	15
1.8	Illustration of the proposed models for gamma-ray binary systems. Left: Rotation-powered pulsar model. Right: Accretion-powered microquasar model (Dubus 2013).	19
2.1	Diagram illustrating the helical motion experienced by charged particles in a magnetic field that causes synchrotron emission. Figure is a remade version of a figure from Rybicki & Lightman (1986).	21
2.2	Spectrum of single electron as a result of synchrotron emission where $x = \nu/\nu_c$ (Blumenthal & Gould 1970).	23
2.3	Sketch of the two frames of reference to consider when inverse Compton occurs between a photon and a relativistic electrons (Rybicki & Lightman 1986).	24
2.4	Scattered photon distribution function of IC in the Thomson scattering limit (Blumenthal & Gould 1970).	26
3.1	Diagram illustrating the opacity of Earth's atmosphere for electromagnetic radiation at different wavelengths (Credit: NASA).	29
3.2	Artist concept of the Fermi telescope spacecraft (Credit: NASA). . .	30

3.3	Diagram of the Fermi-LAT illustrating the pair production detection method. (Credit: NASA's Goddard Space Flight Centre).	31
3.4	The effective area of Fermi-LAT with respect to energy under the latest IRFs (P8R3) assuming normal incidence photons (Bruehl et al. 2018).	32
3.5	Point Spread Function (PSF) of Fermi-LAT showing the 68% and 95% containment angles (angular resolution) for the front and back of the detector (Bruehl et al. 2018).	32
3.6	Illustration of the current model for the completed Athena space observatory (Credit: X-IFU Consortium).	33
3.7	A diagram of the layout of SPO that will be used for the mirror on Athena. The images on the right show pictures of the SPO material that will be used (Wille et al. 2015).	34
3.8	Effective area of Athena X-IFU compared to one of the XRISM Resolve instrument, both being imaging spectrometers. The effective area of three dispersive spectrometers are also shown: two currently in operation, XMM-Newton RGS and Chandra HETG, and Arcus proposed to NASA as a MIDEX and currently completing its Phase A concept study (Credit: X-IFU Consortium).	35
3.9	Diagram showing how CTA and other IACT capture the Cherenkov effect. The Cherenkov flashes caused by the particle shower are captured by snapshots on the telescope detectors. Comparing the direction of the snapshot on multiple telescopes allows the for the location and direction of the incident photon to be re-created (Credit: R. White (MPIK), K. Bernlohr (MPIK), DESY).	36
3.10	Differential sensitivity comparison between CTA, currently operational IACTs (MAGIC, VERITAS, H.E.S.S.), HAWC and Fermi-LAT. (Credit: CTA Consortium & Observatory).	37
3.11	From left to right shows the SST, MST (two prototype designs are being tested) and LST for CTA (Credit: Gabriel Pérez Diaz, IAC).	38
3.12	All-sky map for energies > 1 GeV made from the first 5 years of Fermi-LAT observations where the central band marks the plane of the Milky Way galaxy (Credit: NASA/DOE/Fermi LAT Collaboration).	40
4.1	Sketch of the orbit of PSR B1259-63 around the periastron (Aharonian, F. et al. 2005). The colour gradient shows the integral TeV flux of H.E.S.S. observations from Aharonian, F. et al. (2005).	44
4.2	Sketch of the colliding winds and the stream of accelerated particles from the pulsar wind on one side and the stellar wind/circumstellar disc on the other. As seen in systems such as PSR B1259-63 (Credit: Chernyakova, M. INAM 2021).	45
4.3	Maps of the region surrounding PSR B1259-63 using observational data from the 2017 periastron (57968 – 58118 MJD). Left: Binned counts map of the region where PSR B1259-63 is located with a 15° radius. Right: Test Significance map of the 20° region (see highlighted square in the left count map). This was calculated using a source model with all sources from the 4FGL catalogue within 20° of the location of PSR B1259-63.	47

4.4	Evolution of multiwavelength PSR B1259-63 spectral characteristics over the different periastron passages. <i>Panel a:</i> Fermi-LAT flux measurements in the $E > 100$ MeV energy range with a weekly bin size. Flux is given in $10^{-6} \text{ cm}^{-2} \text{ s}^{-1}$. <i>Panel b:</i> 1-10 keV X-ray flux in units of $10^{-11} \text{ erg cm}^{-2} \text{ s}^{-1}$. <i>Panel c:</i> X-ray slope. <i>Panel d:</i> $H\alpha$ equivalent width.	49
4.5	Daily-binned light curve of the 2017 periastron passage. The highlights indicate the time periods that were used for spectral analysis and modelling; the details are given in Table 4.2. The different periods are shown as: prfl1 = Red, prfl2 = Magenta, avfl = Yellow, pkfl = Green.	51
4.6	A sketch of the geometry of the proposed model (not to the scale) for the period of GeV flare (Chernyakova et al. 2020). Red sphere presents the Be star with the disc shown with yellow semi-transparent circle. Stellar/pulsar winds interaction cone is shown with cyan. PSR B1259-63 pulsar orbit is illustrated with black line. The unshocked pulsar electrons (magenta) are strongly accelerated in the region close to the cone's tip (blue region; "strongly shocked electrons") and weakly accelerated at the rest of the cone surface (cyan region; "weakly shocked electrons"). The flight directions of these electrons are shown with cyan/magenta arrows. The clumps of stellar wind are shown with yellow spheres.	53
4.7	Comparison of the cooling times to acceleration and escape time for various radiation processes in the case of avfl model, see text for details.	54
4.8	GeV emission of PSR B1259-63 during the periods twenty days before (blue points, prfl1) and after (red points, prfl2) the periastron. Blue and red curves show best fit models in 100 MeV – 2 GeV energy range, see Table 4.3. Shaded regions show 1σ confidence range for fitted models.	57
4.9	<i>Left:</i> Broad band spectrum emission of PSR B1259-63 during the 20 days before (blue points) and after (red points) the periastron period. Green X-ray points are NuSTAR observations of the 2014 periastron from (Chernyakova et al. 2015) <i>Right:</i> Broad band spectrum emission of PSR B1259-63 during the GeV flare. Blue points represent the flare averaged over the whole duration, and red points correspond to the sum of peak periods. The TeV points shown are taken from Aharonian, F. et al. (2005), and the shaded regions at TeV energies represent the range of multi-years H.E.S.S. measurements reported in Fig. 2 of H. E. S. S. Collaboration et al. (2020). The shaded regions at X-ray energies represent the range of fluxes observed by SWIFT in 2017 before (left panel), and after (right panel) the GeV flare. In both panels dashed lines show an IC component, solid magenta line corresponds to synchrotron emission of strongly shocked electrons, dash-dotted line shows the bremsstrahlung component and black solid line corresponds to overall model emission.	58

4.10	Evolution of PSR B1259-63 flux over the different periastron passages (Chernyakova et al. 2021). Dashed lines correspond to the periastron and to the moments of disappearance (first non-detection) and reappearance (first detection) of the pulsed emission, as observed in 2010 (Abdo et al. 2011). Dotted lines correspond to the first appearance of the detection in GeV band at a day time scale in 2010 and 2021. <i>Panel a:</i> flux measurements in the $E > 100$ MeV energy range with a weekly bin size. Flux is given in $10^{-6} \text{ cm}^{-2} \text{ s}^{-1}$. <i>Panel b:</i> absorbed 1-10 keV X-ray flux in units of $10^{-11} \text{ erg cm}^{-2} \text{ s}^{-1}$. Scaled 5.5-GHz radio data from 2021 are also shown in this panel with a gold dashed line for comparison. <i>Panel c:</i> radio flux densities in mJy. <i>Panel d:</i> $H\alpha$ equivalent width.	62
4.11	Left: Fermi-LAT weekly (green points) and daily (magenta upper limits and red points – detection's with $TS > 4$) light curves of PSR B1259-63 at energies 0.1 – 10 GeV. The dotted line present the flux corresponding to spin-down luminosity of PSR B1259-63 ($L_{sd} = 8.2 \cdot 10^{35} \text{ erg/s}$). Right: Blue points: Fermi-LAT light curve at > 0.1 GeV range for the period MJD 59310–59363 ((+55; +108) days after the periastron) with adaptive time binning (to have 9 photons per time bin in 1° radius circle around PSR B1259-63 position at 0.1–10 GeV). The light curve covers the period of the highest flux of the source in the GeV band. Red points correspond to a daily lightcurve, same as in the left panel (Chernyakova et al. 2021).	63
5.1	Sketch of the Vela X-1 showing the photoionization and accretion wake over three orbital phases (Malacaria et al. 2016). The position of the observer is such that the pulsar lies between the observer and the supergiant at $\phi = 0.5$ and the supergiant eclipses the pulsar and wakes at $\phi = 0.0$	66
5.2	To-scale diagram of Vela X-1 (Grinberg et al. 2017) based on hydrodynamical simulations of the system by Manousakis (2011).	66
5.3	Simulated X-IFU 10 ks observation spectrum of Vela X-1 at three orbital phases. Red: $\phi = 0.00$, Green: $\phi = 0.25$, Blue: $\phi = 0.50$	68
5.4	Phasecurve of Vela X-1 used for the initial X-IFU simulations for a period of 774490 s and flux in the energy range of 0.2 – 12.0 keV. Blue points represent the main simulated phases (0.00, 0.25, 0.50). . .	69
5.5	Comparison of Chandra observations and Athena simulations in 1.0–10.0 keV energy range. Left: X-ray spectrum of Vela X-1 from the Chandra HETGS with 83 ks (eclipse) and 29 ks observations from Watanabe et al. (2006). Right: Simulated X-IFU spectrum of the same models from 10 ks observations. Colours indicates the orbital phase: Red=0.00 (Eclipse), Green=0.25, Blue=0.50.	70
5.6	Comparison of the spectral quality of the Iron $K\alpha$ line in the Vela X-1 spectrum from 6.3-6.5 keV with different exposure times (Black: $\phi = 0.00$, Red: $\phi = 0.25$, Green: $\phi = 0.50$). Top-Left: 1 ks, Top-Right: 2 ks, Bottom-Left: 5 ks, Bottom-Right: 10 ks.	72
5.7	Comparison of the fitted width error of the $K\alpha$ Iron line in the simulated X-IFU Vela X-1 spectra with different exposure times.	72

5.8	Spectra from simulated 5 ks observations with X-IFU of the XSTAR model lines. Due to the high column density applied to the line models in XSPEC, lines at lower energies are not visible. Spectra are shown in the energy range 1.5 – 8.0 keV. Red: $\phi = 0.00$, Green: $\phi = 0.25$, Blue: $\phi = 0.50$	78
5.9	Plots of the integrated luminosity of the emission lines of the XSTAR models, using the Al XII line. Top-Left: Luminosity map with no eclipse. Top-Right: Eclipse at superior conjunction ($\phi = 0.00$). Bottom-Left: Partial eclipse ($\phi = 0.98$). Bottom-Right: Partial eclipse ($\phi = 0.02$).	79
5.10	Plots of the integrated luminosity of the emission lines of the updated XSTAR model, using a Fe XVIII line. Top-Left: $\phi = 0.85$. Top-Middle: $\phi = 0.90$. Top-Right: $\phi = 0.95$. Bottom-Left: $\phi = 0.05$. Bottom-Middle: $\phi = 0.10$. Bottom-Right: $\phi = 0.15$	80
5.11	Spectra of 5 ks observations using lines from XSTAR models. Red: $\phi = 0.05$, Green: $\phi = 0.25$, Blue: $\phi = 0.50$	82
5.12	Top: Spectra of 5 ks observations using lines from XSTAR models. Centre-Left: $\phi = 0.05$. Centre-Middle: $\phi = 0.06$. Centre-Right: $\phi = 0.07$. Bottom-Left: $\phi = 0.08$. Bottom-Middle: $\phi = 0.09$. Bottom-Right: $\phi = 0.10$	83
5.13	Example of the radial luminosity of different lines as defined by the XSTAR model. Top-Left: O VIII, 0.637 keV. Top-Right: Fe XVIII, 6.422 keV. Bottom-Left: Cl XVII, 2.962 keV. Bottom-Right: Fe XXV, 6.664 keV.	84
5.14	Plot of the input and measured line normalization for the Al XII line at 1.598 keV from 5 ks simulations. Errorbars represent the 90% confidence range of the fitted normalization values.	85
5.15	Plots of the event counts in narrow emission lines (red points) and the input flux (blue line) at different orbital phases with simulations of the revised XSTAR model. Left: Fe lines from the emission line complex at 6.4 – 6.5 keV. Right: Oviii line at 0.653 keV, one of the brightest lines in the model.	86
6.1	TS map centred on SS433. Map is based on analysis of 9 yrs of Fermi-LAT data by Rasul et al. (2019). Blue circles represent the lobe positions according to Abeysekara et al. (2018), the red cross represents the position of SS433 and the red circles represent the optimised extension (solid circle) with the 1σ uncertainty (dashed circles).	90
6.2	TeV image of the SS433 region based on 1017 days of HAWC data from Abeysekara et al. (2018). The east and west lobes observed in X-ray are indicated (e1, e2, w1 & w2) and the location of the binary source (red cross).	91
6.3	Comparison of the flux error ratio from 100 simulations at different exposure times using the North and South IRFs.	93

6.4	Histograms of the measured flux based on 100 CTA simulations of the central source of SS433 in a uncrowded region (left) and a crowded region (right). The top right of each plot gives the average flux and the 1σ error of the flux from the 100 simulations. The green shading represents the 3σ range of the simulations.	94
6.5	Comparison of the flux 1 sigma ratio from 100 simulations at different photon fluxes using the North and South IRFs.	94

List of Tables

1.1	List of systems classified as gamma-ray binaries according to Chernyakova & Malyshev (2020).	17
4.1	Details on the time of each periastron and definitions of each GeV flare period (calculations based on Shannon et al. (2014)).	46
4.2	Details of the time periods used for spectral analysis during the 2017 periastron. $t_p = \text{MJD } 58018.1$ corresponds to the time of 2017 periastron passage.	48
4.3	Spectral model parameters from the binned likelihood analysis of different phases of the 2017 periastron from 0.1 - 2.0 GeV. The model used is the PLSuperExpCutoff where $dN/dE = N_0(E/E_c)^{\gamma_1} \exp(-(E/E_0)^{\gamma_2})$	51
4.4	Details of the models. D is a distance from the Be star to the emission region (Chernyakova et al. 2020). Effective luminosity L of the pulsar wind electrons (without considering beaming effects) is measured in units of spin-down luminosity $L_{sd} = 8.2 \times 10^{35} \text{ erg/s}$	57
5.1	Log of Chandra observations used by Watanabe et al. (2006) for modelling the line emissions of Vela X-1 at three orbital phases. Phases are defined such that inferior conjunction occurs at orbital phase 0.50 and superior conjunction (eclipse) occurs at phase 0.00.	67
5.2	List of the continuum parameters used in X-IFU simulations of Vela X-1. Values for the column density and photon index are taken from Watanabe et al. (2006).	67
5.3	Emission lines present in the eclipse (phase = 0.00) spectral model from Watanabe et al. (2006).	71
5.4	Emission lines present in the non-eclipse (phase = 0.25, 0.50) spectral model from Watanabe et al. (2006).	73
5.5	Key parameters of the XSTAR model used for X-IFU simulations. All elemental abundances were left at the default value.	77
5.6	Details of the phase-dependent spectrum for XSTAR models as defined in the SIMPUT used for X-IFU simulations. Relative flux was based on the orbital phase with the highest flux ($\phi = 0.25 \& 0.75$).	77
5.7	Key parameters of the XSTAR model used for X-IFU simulations to better replicate the accretion wake of Vela X-1. All elemental abundances were left at the default value.	80
5.8	Details of the variable spectrum for XSTAR models as defined in the SIMPUT used for X-IFU simulations. Relative flux was based on the calculated flux of the models in XSPEC.	81

6.1	Extension models used for the East and West lobes of SS433 in CTA simulations.	91
6.2	Comparison of the detectability of the western and eastern lobes of SS433 for various source extensions and exposure times using the North site IRFs (prod3b-v2).	92
6.3	Comparison of the detectability of the western and eastern lobes of SS433 for various source extensions and exposure times using the South site IRFs (prod3b-v2).	92

Abbreviations

- EM = Electromagnetic
- XRB = X-ray Binary
- LMRB = Low-Mass X-ray Binary
- IMRB = Intermediate-Mass X-ray Binary
- HMXB = High-Mass X-ray Binary
- SgHMXB = HMXB with a Supergiant star
- BeXRB = HMXB with a Be-star
- NS = Neutron Star
- BH = Black Hole
- HE = High-Energy
- VHE = Very High-Energy
- EM = Electromagnetic
- eV = Electron Volts ($1 \text{ eV} = 1.60218 \times 10^{-19} \text{ J}$)
- erg = CGS unit of energy ($1 \text{ J} = 10^7 \text{ erg}$)
- RLO = Roche-lobe Overflow
- LAT = Large Area Telescope
- X-IFU = X-ray Integral Field Unit
- SPO = Silicon Pore Optics
- TES = Transition Edge Sensors
- CTA = Cherenkov Telescope Array
- IACT = Imaging Atmospheric Cherenkov Telescope
- SIXTE = Simulation of X-ray Telescopes
- SIMPUT = Simulation Input
- SED = Spectral Energy Distribution
- TS = Test Statistic

Study of High-Energy Emission from High Mass X-ray Binaries

Samuel Mc Keague

Abstract

Since their discovery, the study of High Mass X-ray Binaries (HMXBs) has revealed an extremely powerful and energetic environment that is capable of accelerating particles to Very High Energies (VHE). With the advent of more advanced gamma-ray astronomy technology in the last decade a small number of HMXBs have been detected at GeV and TeV energies which has led to the classification of gamma-ray binary systems.

One of these systems, PSR B1259-63, has been intensively studied in the past decade to understand the origins of the off-set GeV flaring during orbital periastron. An analysis I have conducted of Fermi-LAT observations of the 2017 passage, along with comparison to previous observations, has led to new insight of the GeV flare origin where the energy is released from unshocked and weakly shocked electrons of the pulsar wind as a beaming effect in the direction of the observer.

With current X-ray telescopes, resolving the multiple X-ray emission sources and high variability of HMXBs requires extremely long observations and even then, may not be resolvable. The Athena X-ray Integral Field Unit (X-IFU), currently in development, will be capable of significantly higher resolution observations on both the energy and time scale. Vela X-1 is an archetypical HMXB where the spectra exhibit many emission lines that vary during the orbital eclipse of the binary companion. X-IFU will have the ability to detect changes in the emission line profile and possibly discover new emission lines. I have simulated X-IFU observations of Vela X-1 with theoretical line profiles modelled with XSTAR.

The Cherenkov Telescope Array (CTA) will provide an order of magnitude greater sensitivity of the TeV observations of HMXBs. In my work I have studied the capability of CTA to detect variability from microquasars depending on their fluxes and observation exposure.

Chapter 1

Introduction: High Mass X-ray Binaries

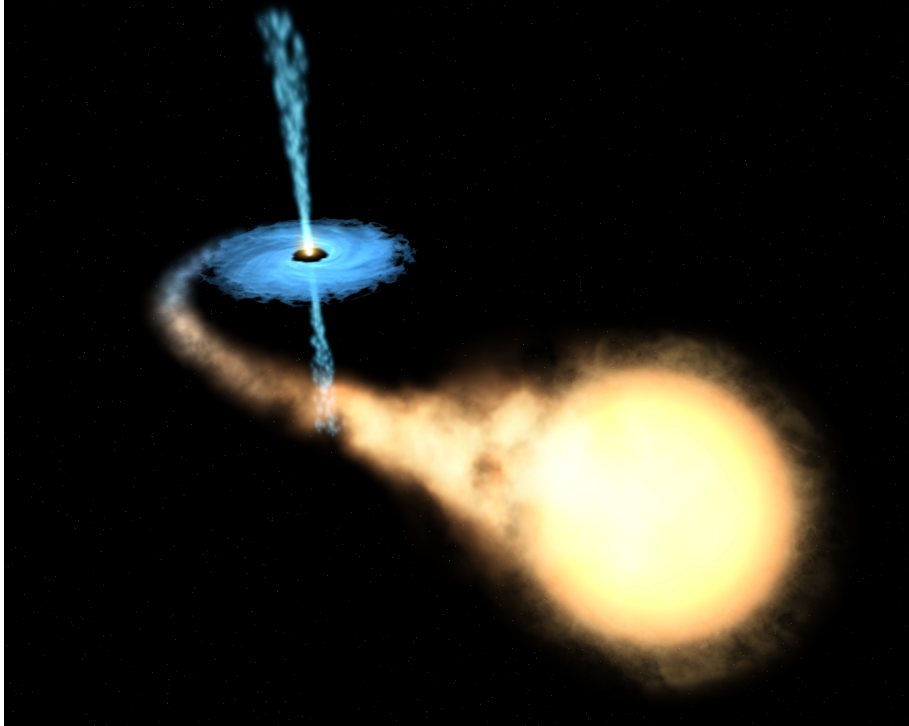


Figure 1.1: Artist impression of a XRB, GRO J1655-40, where matter is directly accreted from the massive star onto the compact object (Credit: ESA, NASA, Felix Mirabel).

In our Galaxy, over 50% of observed X-ray emissions originate from X-ray binary star systems (Grimm et al. 2003). X-ray binaries (XRBs) are binary star systems where electromagnetic (EM) emission is most prominent at X-ray energies. The systems are comprised of a compact source, that being a white dwarf (WD), neutron star (NS) or a black hole (BH), which pulls material from a donor companion star via accretion (see Sec. 1.1). XRBs can be divided in sub-classes depending on the

nature of the donor companion star. Low-Mass X-ray Binaries (LMXBs) have a donor star with a mass of $< 1 M_{\odot}$ (M_{\odot} = solar mass), High-Mass X-ray Binaries (HMXBs) have a donor star with a mass of $> 10 M_{\odot}$ and Intermediate-Mass X-ray Binaries (IMXBs) covers masses between LMXBs and HMXBs. The most active class of these systems are HMXBs. These sources are comprised of a compact object, either a NS or a BH with a massive O/B spectral type companion star. The strong X-ray emission from these systems is a result of accretion of matter from the massive companion onto the compact object (Chaty 2011). An illustration of a HMXB is shown in Fig. 1.1.

In the case of HMXBs, the accretion process can occur as a result of three different circumstances, depending on the nature of the donor star and the geometry of the system (Chaty 2011). Two of these processes occur in Supergiant X-ray binaries (SgHMXBs) which have a companion that is an early spectral stage supergiant star with a steady wind outflow. The remaining process occurs in Be X-ray binaries (BeXRBs), where the massive companion is a spectral type Be star with a circumstellar disc accompanied by a compact object. Firstly, in SgHMXBs, accretion is a result of the donor companion overflowing its Roche lobe, leading the formation of an accretion disc. Secondly, also in SgHMXBs, the stellar wind outflow of the supergiant is accreted by the compact object. Finally, in BeXRBs, the compact object, in a highly eccentric orbit, crosses the circumstellar disc of the Be star causing a period of accretion.

Since their discovery, HMXBs have been sources of intense study and remain so to this day. Accretion is the most efficient method for energy production in the Universe and HMXBs each provide a laboratory to observe and study the accretion processes (see Sect. 1.1). This also results in HMXBs being highly variable with complex environments. Resolving the X-ray emissions of these systems has proven difficult, even with the advances in X-ray astronomy since their discovery, because they have multiple regions of X-ray emission including the accretion disc, the surrounding hot corona, stellar wind collision, photoionization regions and the presence of relativistic jets. They are often highly variable systems due to flaring and orbital variation. Origins of flaring in these systems is difficult to understand with current X-ray instruments as they do not have the resolution and sensitivity to analyse the spectrum during these flares. Thus we have to look to the possibilities of future X-ray missions to advance our understandings of these systems (see Sect. 3.2 & Ch. 5).

Some systems, such as microquasars (see Sect. 1.3) also exhibit different spectral states that affects the broadband high-energy spectrum. In the last decade a few HMXBs have been detected at gamma-ray energies, both high-energy (HE, $E > 100$ MeV) and very high-energy (VHE, $E > 100$ GeV), and the origin of these emissions

are still under debate (see Sect. 1.4). Observations at GeV are available from the Fermi Telescope (Sect. 3.1) so analysis of observational data from gamma-ray binaries is essential to develop a better understanding of the HE emission (Ch. 4). It's difficult to resolve detections of HMXBs at VHE with the current TeV arrays, so the upcoming new TeV array is of great interest to potentially learn a lot more about VHE emission from these systems (see Sect. 3.3 & Ch. 6).

1.1 Accretion

The principal mechanism that results in the release of high-energy emission from XRBs is the accretion of stellar material. Equations presented here on accretion physics are referenced from “Ch. 18: Close Binary Star Systems” from Carroll & Ostlie (2007). Accretion is the accumulation of material onto a massive object by the gravitational attraction of matter. Many celestial objects, such as planets and stars, are formed as a result of accretion. In the case of XRBs, gravitational potential energy is released in the form of heat and EM radiation from matter falling onto the compact object. This energy release is therefore represented by (Eq. 1.1):

$$E_{acc} = \frac{GMm}{R} \quad (1.1)$$

where M and R is the mass and radius of the accreting body and m is the mass accreted falling from infinity. From this equation, the energy released is proportional to M/R and therefore the accretion caused by compact objects such as NS and BH will be extremely efficient. For example, compare the energy output by the accretion of matter onto a white dwarf (WD) against the same accretion on a NS. A WD and NS both typically have a mass of $\sim 1 M_{\odot}$ but a WD has a radius on the scale of $\sim 0.01 R_{\odot}$ while a NS has a typical radius little more than $10^{-5} R_{\odot}$ (Shipman 1979). Using these values in Eq. 1.1, the energy output from NS accretion is $\sim 10^3$ times greater than that of an WD for the same accreted mass.

The luminosity of an accreting body, given that the mass and radius of the body is constant, is dependent on the rate of matter accreted. Thus the luminosity can be derived using the rate of mass accreted \dot{m} as show in the following Eq. 1.2.

$$L_{acc} = \frac{dE_{acc}}{dt} = \frac{GM}{R} \frac{dm}{dt} = \frac{GM\dot{m}}{R} \quad (1.2)$$

Applying Eq. 1.2 to a HMXB with a NS and an observed luminosity of 10^{38} erg, the rate of accreted mass is $\sim 10^{-8} M_{\odot}\text{yr}^{-1}$. However, there is a limit to the luminosity of any given system as a result of accretion. This limit will be reached when the gravitational force on accreted matter is matched by the outward force of radiation

emitted. The gravitational force is simply represented by Newton's Gravitational Law (Eq. 1.3).

$$F_{grav} = \frac{GMm}{r^2} \quad (1.3)$$

The radiation force using the momentum p transferred from photons to electrons where $p = h\nu/c$ and the number of photon-particles scatterings per second. For luminosity L , the number of photons, with frequency ν , crossing a radius r per second can be calculated by $\frac{L}{4\pi r^2 h\nu}$. Using the Thomson scattering cross-section σ_T , the rate of scatterings that occur can be calculated by $\frac{L\sigma_T}{4\pi r^2 h\nu}$. Taking the rate of scatterings and the momentum transferred by photons, the outward force exerted by radiation can be calculated using Eq. 1.4.

$$F_{rad} = \frac{L\sigma_T}{4\pi r^2 c} \quad (1.4)$$

Thus when F_{grav} is equal to F_{rad} , the accretion luminosity limit can be calculated, see Eq. 1.5 & 1.6. This is known as the Eddington luminosity.

$$F_{grav} = F_{rad} \Rightarrow \frac{GMm_p}{r^2} = \frac{L\sigma_T}{4\pi r^2 c} \quad (1.5)$$

$$L_{Edd} = \frac{4\pi c GMm}{\sigma_T} \quad (1.6)$$

The spectrum of the emitted radiation as a result of accretion on a compact object is dependent on the temperatures associated with the system. When accreted matter falls onto the surface of a compact object, the energy released heats the surface of the object. Any radiation that results from the surface of the compact object can be approximated as blackbody radiation. For a blackbody source, the blackbody luminosity of the source can be calculated by:

$$L = 4\pi r^2 \sigma T_{BB}^4 \quad (1.7)$$

where σ is the Stefan-Boltzmann constant and T_{BB} is the effective blackbody temperature. Rearranging this equation for an observed source with luminosity L the blackbody temperature is calculated by Eq. 1.8.

$$T_{BB} = \left(\frac{L_{acc}}{4\pi r^2 \sigma} \right)^{1/4} \quad (1.8)$$

There is also a temperature more directly associated with the accretion energy. Consider that most material accreted is going to be comprised of mostly free protons and electrons. According to the kinetic theory of gases, the kinetic energy of both the population of protons and electrons is $E = 2(\frac{3}{2}kT_{th})$. The corresponding potential

energy relating to the accretion (Eq. 1.1) is calculated by $E = \frac{GM(m_p+m_e)}{R}$ but as the mass of the proton m_p is much greater than that of the electron m_e so the mass accreted can be rounded to m_p . These two equations can be used in order to calculate the thermal temperature T_{th} associated with the accretion energy (Eq. 1.9 & Eq. 1.10).

$$\frac{GMm_p}{r} = 3kT_{th} \quad (1.9)$$

$$T_{th} = \frac{GMm_p}{3kr} \quad (1.10)$$

The last temperature to consider is the temperature of photons emitted from accretion and this can be approximated with $h\nu \sim kT_{rad}$ where T_{rad} is the temperature of the radiation. With these temperatures in mind, the emitted spectrum from accretion onto a compact object is generally $T_{BB} \leq T_{rad} \leq T_{th}$. Using the previously mentioned values for the radius and luminosity of an accreting NS, the resultant spectrum due to accretion is in the range of $1 \text{ keV} \leq h\nu \leq 50 \text{ MeV}$.

The rate at which matter is accreted depends on the source of material. In XRBs, accretion material is provided by the companion source. The rate is also dependent on the geometry of the system with regards to the Roche lobe of the compact object. In a binary system, the Roche lobe defines the region of each object where orbiting material is gravitationally bound to it (see Fig. 1.2 for example sketch).

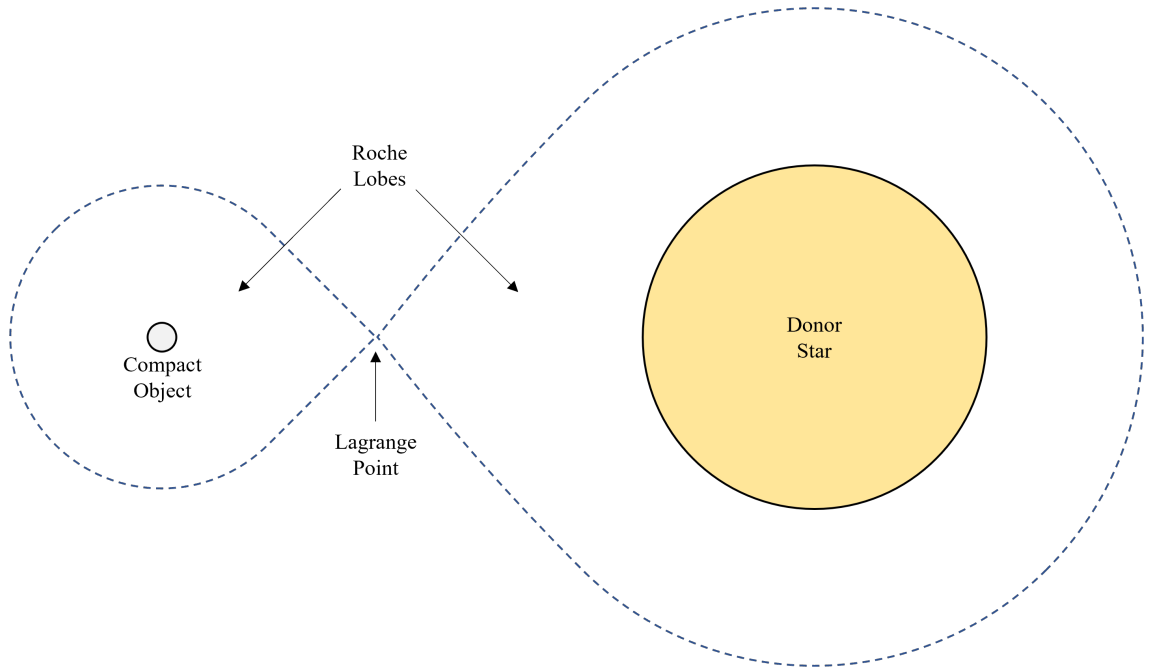


Figure 1.2: Simple illustration of the Roche lobe boundaries and intersection in XRBs.

1.1.1 Roche-lobe Overflow

If the separation between both objects is such that the donor star is larger than the Roche lobe then matter begins to be accreted directly from the outer layers of the star (see Fig. 1.3). This is known as Roche lobe overflow (RLO). Matter that is accreted in this manner conserves angular momentum from its star of origin, causing the matter to miss the compact object. As the stream of accreted material begins to circulate around the compact object, the material forms a disc of accreted material referred to as an accretion disc. Matter within the disc loses angular momentum due to collisions and this friction also converts kinetic energy of the material into heat. The loss of angular momentum eventually causes material to fall onto the compact object, resulting in the energy release described by Eq. 1.1. The total mass of the disc is typically significantly less than accreting body. Thus, there is no effect of self-gravity and the disc material travels has a Keplerian orbit, where $v = \sqrt{GM/r}$. From this the kinetic energy E_{disc} of the disc can be derived and shown to be half the accretion energy E_{acc} at the radius of the compact object (Eq. 1.11).

$$E_{disc} = \frac{1}{2}mv^2 = -\frac{GMm}{2r} = \frac{E_{acc}}{2} \quad (1.11)$$

As a result, the matter in the inner disc orbits at a higher velocity than at the outer disc which creates a temperature gradient where the inner regions of the disc are much hotter than the outer regions. In XRBs, this gradient causes a difference of peak emission wavelength in the disc, with emission of X-rays in the inner disk and optical emission in the outer disc. The radial gradient of the disc temperature can be derived from conservation of energy in the disc. Energy radiated from an annulus of the disc dr , dE , at radius r in the time dt is equal to the energy that passes any boundary of the annulus at radius r (Eq. 1.12).

$$dE = \frac{dE}{dr}dr = \frac{d}{dr} \left(-\frac{GMm}{2r} \right) dr = \frac{GM\dot{m}}{2r^2}dr \quad (1.12)$$

In Eq. 1.12 $m = \dot{m}dt$ for matter entering and leaving the annulus and also assumes that $\dot{m}dt$ is constant. The luminosity of the annulus dL is related to the radiated energy within time dt , $dLdt = dE$, and to the Stefan-Boltzmann law (as previously used for the blackbody luminosity) where the area of the disk on both sides is $A = 2(2\pi r dr)$, thus $dL = 4\pi r \sigma T^4 dr$. Using these equations to solve for the temperature T gives the radial temperature of the disc shown in Eq. 1.13.

$$T_{disc} = \left(\frac{GM\dot{m}}{8\pi\sigma R^3} \right)^{1/4} \left(\frac{R}{r} \right)^{3/4} \quad (1.13)$$

In NS HMXBs, the presence of an accretion disc can be inferred by their position

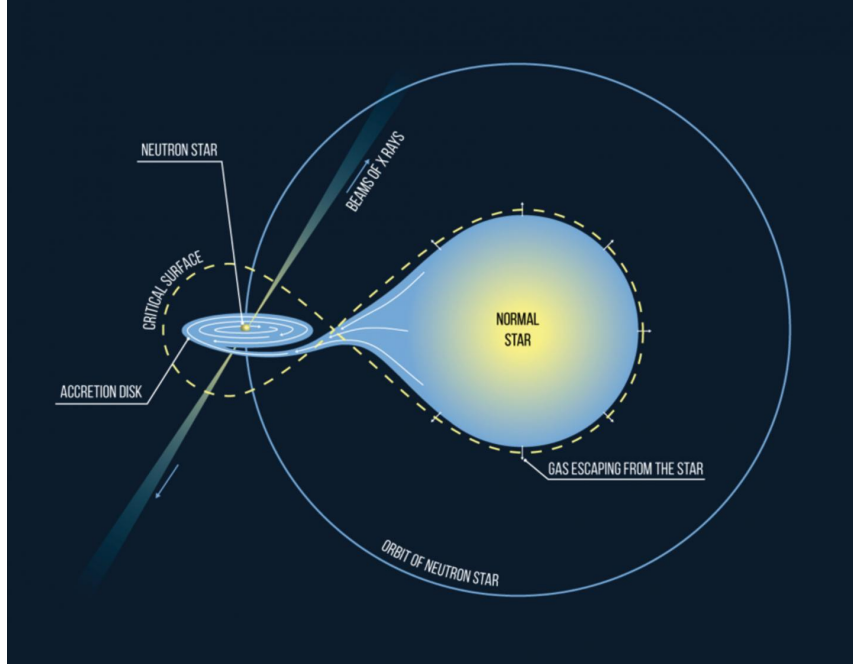


Figure 1.3: Illustration of the Roche lobe boundaries where the donor star is overflowing the Roche lobe so matter is streamed to the compact object. This typically results in an accretion disc (Credit: Moscow Institute of Physics and Technology Press Office).

on Corbet diagram (Corbet 1986) which plots the spin period and the orbital period of the binary system (see Fig. 1.5). In this plot there is a group of bright HMXB that occupy a particular area. These systems are generally considered to be HMXB that form accretion discs (Kretschmar et al. 2019).

While the formation of accretion discs in HMXBs has often been ascribed to RLO, this is not entirely understood in terms of what timescale discs can exist and how the mass loss rate varies. RLO on the full thermal timescale of the donor star leads to a mass loss rate on the scale of $10^{-3} M_{\odot}/\text{yr}$, which will extinguish the X-ray emission of the HMXB (Kretschmar et al. 2019). However, prior to filling the Roche lobe, a phase can begin where atmospheric RLO sets in, which for a hydrogen core donor star could last for thousands of years with a low mass loss rate $< 10^{-8} M_{\odot}/\text{yr}$ (Savonije 1978). Additionally, a stable RLO phase where the mass loss rate is $< 10^{-5} M_{\odot}/\text{yr}$ could last for $> 2 \times 10^4$ yrs before RLO on a thermal timescale begins (Quast et al. 2019). The thermal timescale refers to the timescale in which a star will radiate away its total kinetic energy at its current luminosity. As such, RLO is highly dependent on the lifetime state of the donor star. This is also known as the Kelvin-Helmholtz timescale (Ch. 10, Carroll & Ostlie 2007). There have also been recent indications that under certain conditions, accretion discs may be able to form as a result of wind-fed accretion without the need for RLO, assuming slower wind speeds than usual (El Mellah et al. 2019).

1.1.2 Stellar Wind Accretion

While RLO is the source of accretion in LMXBs and IMXBs, there is an alternative scenario in HMXBs. The donor companion of HMXBs is typically a massive O or B spectral type star, where there is a consistent release of a stellar wind that can be captured by the compact object. In the majority of HMXBs with a supergiant companion (SgHMXB), the compact object accretes matter from the stellar wind outflow. Thus the physical characteristics of the wind has an immediate effect on the accretion rate and as a result the X-ray luminosity (Kretschmar et al. 2019). This is known as wind-fed accretion and it powers well known HMXBs such as Vela X-1 (see Sect. 5.1 for more details). The stream of accretion from stellar winds in the orbital plane of the system leads to the formation of an accretion wake. Accretion wakes initially form as a relatively thin cylinder in front of the accreting object but as more matter is accreted the wake can become more spherical and lead to the formation of shocks (Bertschinger 1987). The diagram in Fig. 1.4 shows the general structure of wind-fed accretion and where the accretion forms with respect to the accreting object.

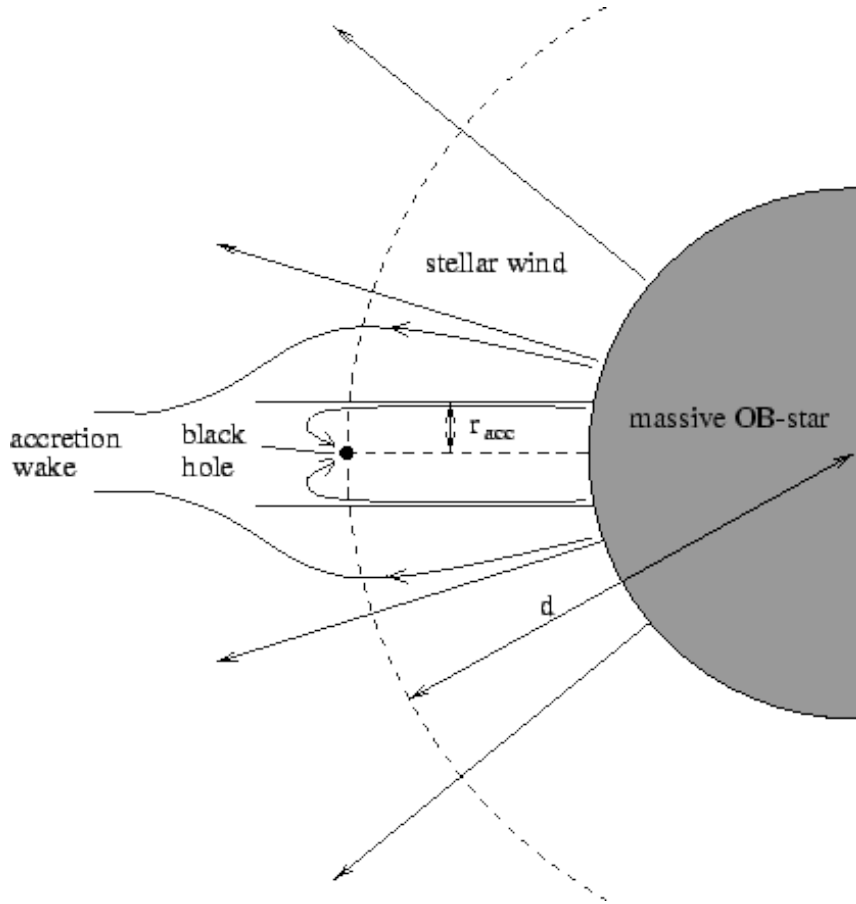


Figure 1.4: Illustration of stellar wind-fed accretion in HMXBs (Credit: Sara Berginius).

The stellar winds of hot luminous stars are driven by ultra-violet resonance lines and are known as line driven winds. The mechanics behind radiation/line driven winds are summarised in Sect. 1.2.2. The acceleration of the winds is highly dependent on ionization and chemical composition. The level of ionization is affected by the stellar parameters of the HMXB in question (e.g. Watanabe et al. 2006; Amato et al. 2021).

Stellar winds can be characterised by two main parameters, the mass loss rate \dot{M} and terminal velocity v_∞ which refers to wind velocity at large distances from the star where acceleration is no longer relevant. For massive stars, mass loss rates are typically on the order of $10^{-6} M_\odot/\text{yr}$ and terminal velocity ranges from 500-2000 km/s (Kudritzki & Puls 2000). For a static, spherically symmetrical stellar wind, mass loss rate can be derived from (Castor et al. 1975):

$$\dot{M} = 4\pi r^2 \rho(r) v(r) \quad (1.14)$$

where r is the distance from the centre of the star, $\rho(r)$ is the density at distance r and $v(r)$ is the velocity at distance r . The radial velocity can be parameterised using the so-called β -velocity law (Castor et al. 1975):

$$v(r) = v_\infty (1 - R_*/r)^\beta \quad (1.15)$$

where R_* is the stellar radius and β describes the steepness of the wind velocity profile. Both v_∞ and β are typically derived by optical and/or ultra-violet observations and spectral analysis. The value of β typically ranges from 0.5 – 1.0 (Kudritzki & Puls 2000). This law is often used due to its simplicity and it has historically proven to be a sufficient approximation to analytical wind solutions.

In sgHMXB, the flow of the stellar wind is significantly influenced by presence of the compact object. The gravity of the compact object focuses the stellar wind towards the orbital plane and the position of the compact object while the orbital movement leads to the formation of a bow shock and an accretion wake. This environment is then ionized by the X-ray emission from the compact object (Kretschmar et al. 2019). The ionization state of the stellar wind is defined as:

$$\xi(r) = L/nr^2 \quad (1.16)$$

where L is the average X-ray luminosity of the compact object and n is the gas density at the distance r from the compact object (Tarter et al. 1969). The X-ray photoionization and heating can form a Strömgren sphere where the stellar wind is no longer accelerated. At the boundary of this region, a shock is formed resulting in sheets of gas trailing the X-ray source (Fransson & Fabian 1980). Generally in

sgHMXBs, an accretion wake develops around and trails the compact object which evolves overtime, resulting in fluctuations. Even assuming a smooth wind as starting conditions the winds are likely to be heavily disrupted due to hydrodynamical effects which accounts for X-ray variability in the absence of clumps (Manousakis & Walter 2015).

1.1.3 Be Star Binaries

Be stars are younger B-type or older O-type stars of high mass ($8-15 M_{\odot}$) that feature a disc around the star's equator. Formation of the disc is a result of ejected matter from the photosphere and the rapid rotation of the Be star (see Sect. 1.2.2 for more on Be stars). Since the disc is formed as a result of matter ejected outward in a similar way to how matter is captured in the process of accretion, the disc is often referred to as a decretion disc (Kretschmar et al. 2019). HMXBs with a Be companion (BeXRB) typically have a wide and highly eccentric orbit with a NS as the compact object. BeXRBs exhibit transient and bright X-ray outbursts (Chaty 2011):

1. Type I: Periodic, occurs each time the NS crosses the decretion disc during periastron.
2. Type II: Giant outbursts that occur at any phase, with a dramatic disc expansion that shrouds the NS.
3. Missed: Outbursts with low $H\alpha$ emission, due to a small disc or inhibited accretion.
4. Shifting outburst phases: Likely due to rotation of dense structures in the decretion disc.

The circumstellar disc of the Be star is naturally truncated in BeXRBs due to the presence of the compact object. In a BeXRB where a NS has a near circular orbit the disc is truncated to a fixed size and significant accretion by the NS is unlikely. This results in persistent low level X-ray emission from the stellar wind and occasional Type II outbursts. However, BeXRBs with a highly eccentric orbit allows for periodic accretion, truncation of the disc depends on the orbital phase and at periastron the NS can move within the disc creating Type I X-ray outbursts (Okazaki & Negueruela 2001).

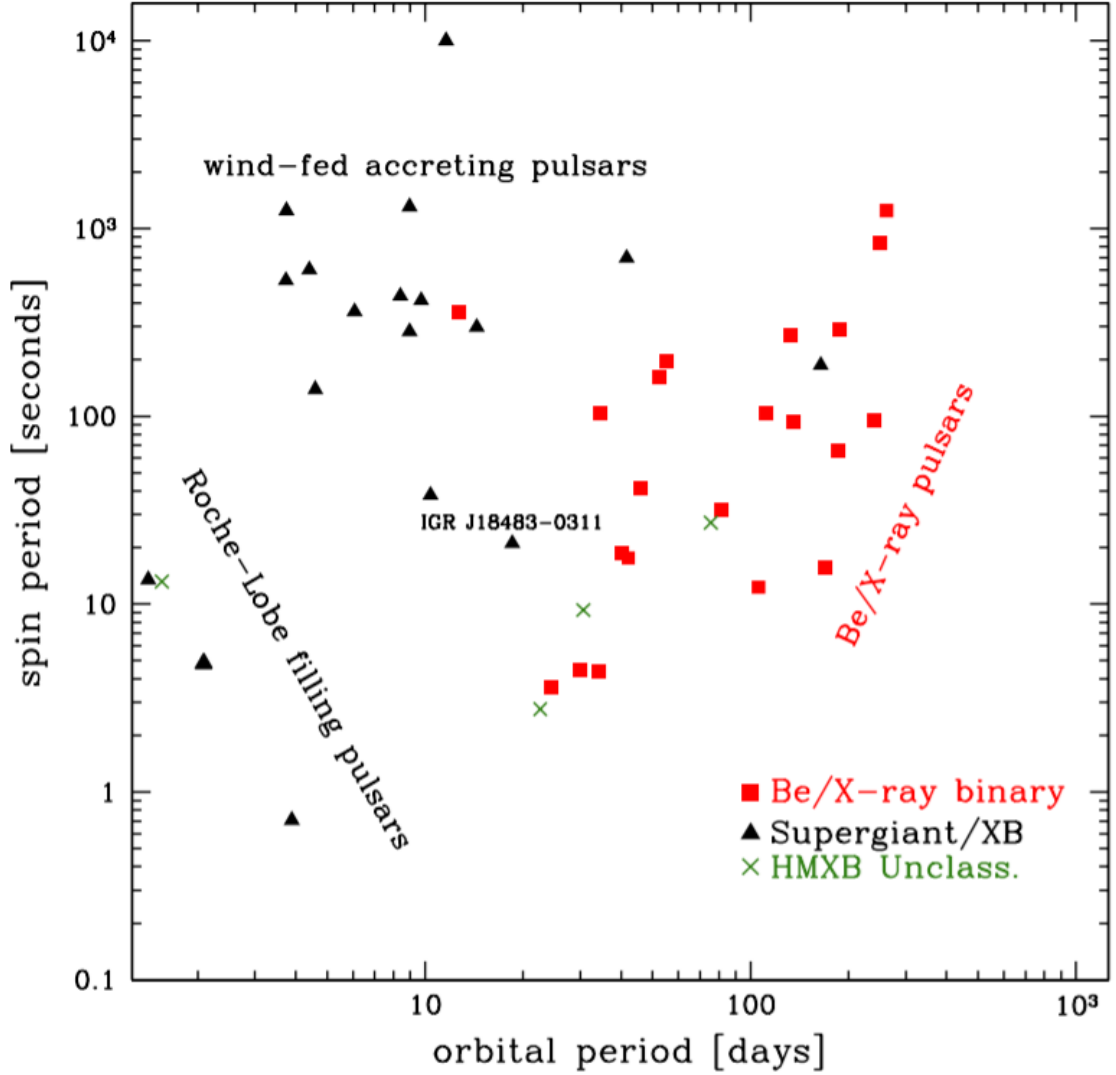


Figure 1.5: Corbet diagram for NS showing three populations of HMXBs: (1) sgH-MXB powered by wind-fed accretion. (2) sgHMXB where accretion is a result of filling the Roche-lobe. (3) HMXBs where the massive companion is a Be star with a disc (Chaty 2011).

1.2 Physical Processes in HMXBs

1.2.1 Wind Collisions & Bow Shocks

There are some known HMXBs where the systems aren't powered by accretion but instead by particle acceleration due to the formation of a bow shock from stellar wind collisions. A bow shock is formed when a celestial object interacts with a flowing ambient matter, such as stellar winds (Sparavigna & Marazzato 2010). They are also formed as the result of collisions between flows of different pressure, temperature and/or density. An example of a visible bow shock from wind collisions is shown in Fig. 1.6. These shocks play an important role in the generation of high-energy emission from highly accelerated particles in gamma-ray binaries such as PSR B1259-

63 (see Sect. 4.1) and PSR J2032+4127 (Lyne et al. 2015). In such binary systems, a bow shock boundary is formed by the collision between stellar wind outflow of massive Be-type stars and pulsar winds.



Figure 1.6: Hubble Space Telescope image of the bow shock created in the Orion nebula by the collision of the stellar winds from LL Orionis and the nebula flow (Credit: NASA).

The acceleration charged particles undergo as a result of shocks is known as Fermi acceleration (Savonije 1978). More specifically, Fermi acceleration is described as acceleration of charged particles due to repeated reflections. There are two different types of Fermi acceleration: first-order acceleration (from shocks) and second-order acceleration (from the environment of magnetized gas clouds). In the case of first-order acceleration, consider a charged particle travelling downstream through a shock. Typically, a shock has magnetic inhomogeneities that precede and follow the shock. In such a case, charged particles that encounter a change in the magnetic field can be reflected back through the shock upstream at increased velocity. If this repeats again the particle continues to greatly increase in energy through multiple reflections. The resulting particle spectrum for many particles undergoing this acceleration is a powerlaw:

$$\frac{dN(E)}{dE} \propto E^{-p} \quad (1.17)$$

where the powerlaw index $p \gtrsim 2$ depends on the nature of the shock. The reason shocks of this nature are referred to as "first-order" is because the energy gained

per shock crossing is directly proportional to the the ratio of the shock velocity to speed of light $\beta_s = v_s/c$.

1.2.2 Radiation-Driven Stellar Winds

The stellar winds from hot and luminous stars, such as O and B spectral-type stars, are driven by radiation pressure (Lamers & Cassinelli 1999). The mechanism behind the radiation driven winds of massive stars was first identified by Lucy & Solomon (1970) and extensively modelled by Castor et al. (1975). These studies found these high velocities in the winds are driven by radiation pressure on the resonance absorption lines of elements such as carbon, nitrogen, silicon and sulphur. Hence why these stellar winds are known as line-driven winds. Due to the high temperature of these massive stars, they emit high levels of ultraviolet (UV) radiation. The outer atmospheres of these stars contain many resonant absorption lines in the UV region of the EM spectrum, which are the primary driver of launching the stellar winds. Observations have shown that winds of this nature have high velocities of $v > 1000$ m/s and cause mass-loss rates of $\dot{M} \sim 10^{-6} M_{\odot}/\text{yr}$. The principle behind line-driven winds is shown in the diagram Fig. 1.7, where UV photons emitted from the star are absorbed by matter in the stellar outflow and then re-emitted.

The presence of these radiation-driven winds in massive stars can lead to the formation of a another spectral class of stars known as Be-type stars, or simply Be stars. These are stars of the B spectral class where Balmer emission lines are observed in the EM spectrum, hence the “e” in Be refers to emission lines. Classical Be stars are non-sugergiant stars (Porter & Rivinius 2003). The origins of these emission lines is tied to the stellar wind outflow and rotational speed of the star. Be stars have a high rotational speed compared to other B-type stars (Massa 1975). As a result, material ejected at the equator forms an equatorial circumstellar disc around the star.

This disc is responsible for unique observational characteristics of Be stars. Excess emission in the infrared is observed as a result from scattering of stellar photons in the disc and emission lines form by re-processing of stellar UV radiation in the disc (Porter & Rivinius 2003). The outflow from Be stars in binary systems results in the formation of bow shocks, as previously described in Sect. 1.2.1, especially during interaction between a compact source and the Be disc. The state of the disc can be determined from observed emission lines. In particular, the observed variation in the ratio between the violet and red emission peaks of the H I emission lines, known as V/R variations, is generally explained by density oscillations in the Be disc (Carciofi 2011). This V/R variation and H α emission line can be used to determine the state of the disc during disruptions in BeXRBs (Reig 2011).

The principle of radiatively driven winds

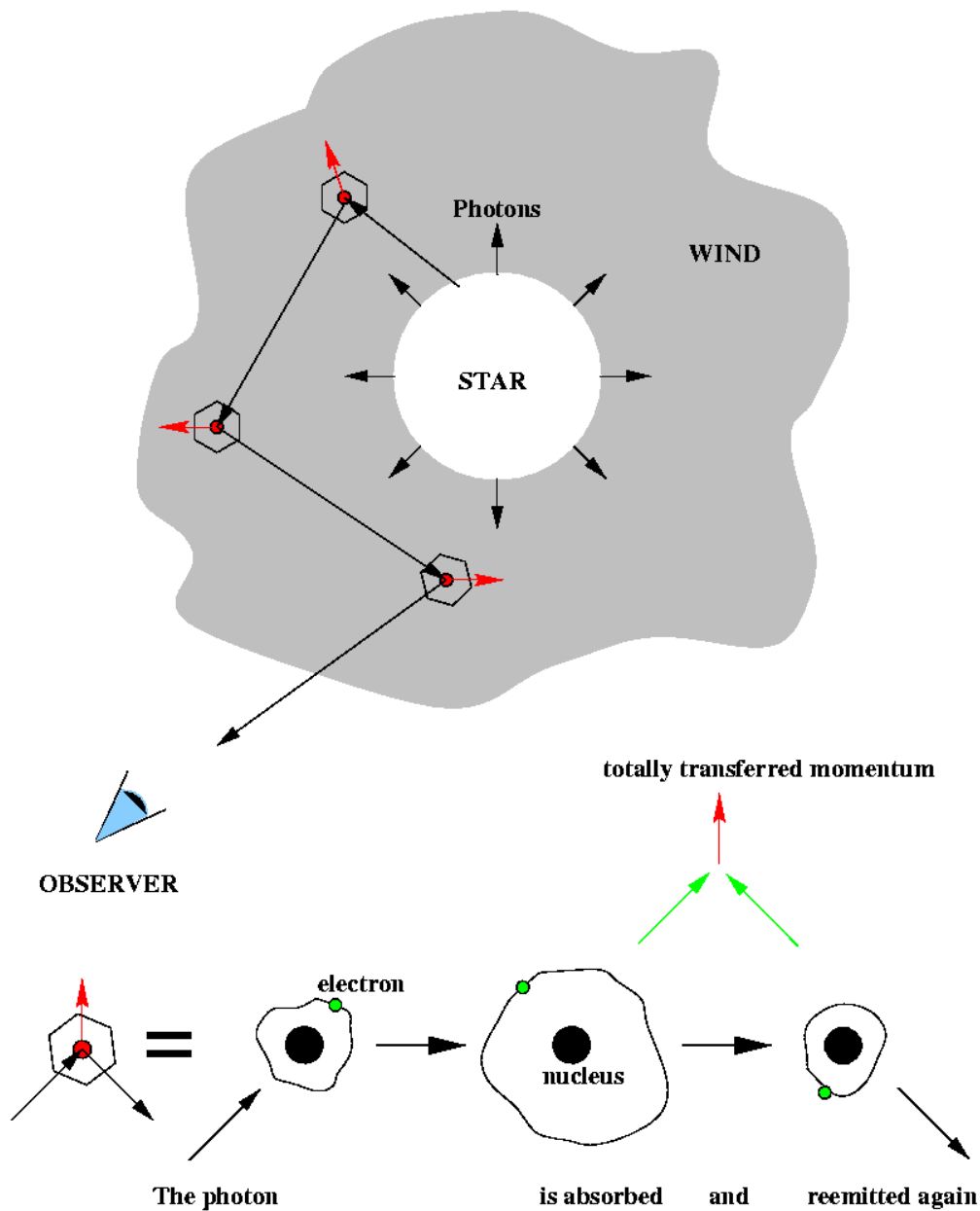


Figure 1.7: A diagram illustrating the principle behind line-driven stellar winds, where UV photons are absorbed by matter from stellar outflow and then re-emitted and this process repeats (Kudritzki & Puls 2000).

1.3 Microquasars

HMXBs where matter is being directly accreted onto the compact object from the massive companion can also form relativistic jets. These can be additionally classed as microquasars (Mirabel & Rodríguez 1998). The jets produce a stream of relativistic particles perpendicular to the plane of the accretion disc, generating strong radio emission and possibly GeV-TeV gamma-ray emission. Microquasars also exhibit multiple spectral states that affect the broadband high-energy spectrum (Chaty 2007).

As a class of HMXBs, microquasars are very bright X-ray sources due to thermal and non-thermal emissions. This is unlike quasars, which are active galactic nuclei powered by a supermassive black hole and surrounded by an accretion disc, where the strongest emission is found at optical and UV energies due to synchrotron emission or TeV due to inverse Compton emission in blazars (Katarzyński et al. 2006). In the case of a BH accreting at the Eddington limit, the characteristic blackbody temperature of the surrounding accretion disc can be approximated by $T \sim 2 \times 10^7 M^{-1/4} K$ where the mass of the BH M is given in solar masses (Mirabel & Rodriguez 1999). With this approximation, any accreting BH with a mass within several solar masses will have a disc with a characteristic temperature of $\sim 10^{6-7} K$, which results in strong thermal X-ray emission from the disc. As X-ray astronomy advanced, microquasars became an extremely useful source of study for accretion environments and relativistic jets compared to quasars, as they are galactic sources with an accretion and ejection timescale that is significantly shorter than that of a quasar (Chaty 2007).

While microquasars are a source of interest in the study of binary system accretion and relativistic astrophysics, the X-ray environment of microquasars can be rather complex due to multiple regions of X-ray emission and strong variability on multiple timescales. As well as the thermal X-rays originating from the accretion disc, the disc is surrounded by a corona that scatters the soft thermal X-rays to hard X-ray energies and a similar process can occur at the base of the jets. The difficulty in resolving these different X-ray emission regions is further compounded by the change in spectral states these systems experience.

In microquasars there are two main spectral states observed (Malzac & Belmont 2008). For luminosities on the scale of a few percent of the Eddington luminosity L_E ($L > 0.01 L_E$), the X-ray spectrum is dominated by thermal components that peak at a few keV, which is believed to originate from a geometrically thin and optically thick accretion disc. The hard X-ray spectrum in this state is non-thermal and normally presents a weak but steep powerlaw spectrum ($\Gamma \sim 2.3 - 3.5$) and extending into MeV energies. As the source in this state is observed to be bright

in soft X-ray and has a soft photon index in hard X-rays, it is called the High Soft State (HSS) (Malzac & Belmont 2008). However, if the system is in a state of low luminosity ($L < 0.01L_E$) the spectrum can be modelled as a hard powerlaw ($\Gamma \sim 1.5 - 1.9$) with a cut-off at ~ 100 keV. This results in the peak in spectrum occurring around a hundred keV. This state exhibits faint soft X-rays and has a hard spectrum, and is thus called the Low Hard State (LHS), which was first observed in black hole transients (Malzac & Belmont 2008).

With the advancements in gamma-ray astronomy from the launch of the Fermi Gamma-ray Space Telescope and ground-based arrays detecting VHE based on Cherenkov radiation, several microquasars have been detected at GeV and/or TeV energies. As of current writing these systems are Cyg X-1 (Malyshev et al. 2013), Cyg X-3 (Abdo et al. 2009) and SS 433 (Bordas et al. 2015; Abeysekara et al. 2018). The origin of these gamma-ray emissions is thought to be linked to particle acceleration caused by the jets of the microquasars and has led to microquasars being proposed as a potential model for HMXBs that are also gamma-ray binaries (Sect. 1.4).

1.4 Gamma-ray Binaries

With the advent of more advanced gamma-ray observatories and detectors since the 2000s, a small number of HMXBs have been discovered at GeV - TeV energies. These systems are classed as gamma-ray binaries and they are specifically distinguished by non-thermal emission peaks in their radiative output $\nu F_\nu > 100$ MeV. Currently there are at least nine systems that are classed as gamma-ray binaries according to Chernyakova & Malyshev (2020), which are listed in Tab. 1.1. While all these

Gamma-ray Binary	Periodicity	Citation
1FGL J1018.6-5856	16.55 days	Corbet et al. (2011)
4FGL J1405.1-6119	13.71 days	Corbet et al. (2019)
HESS J0632+057	318 days	Aharonian et al. (2007)
HESS J1832-93	-	Abramowski et al. (2015)
LMC P3	10.3 days	Corbet et al. (2016)
LS 5039	3.9 days	Aharonian (2005)
LS I +61° 303	26.496 days	Albert (2006)
PSR B1259-63	3.4 yrs	Aharonian, F. et al. (2005)
PSR J2032+4127	50 yrs	Lyne et al. (2015)

Table 1.1: List of systems classified as gamma-ray binaries according to Chernyakova & Malyshev (2020).

systems are HMXBs the only systems in which the nature of the compact object has been identified are PSR B1259-63 and PSR J2032+4127. Within both systems

the compact object is a NS, specifically a radio pulsar, in a highly eccentric orbit around a Be type companion (Johnston et al. 1992; Lyne et al. 2015). There are several young pulsars in orbit around massive stars discovered in radio surveys that have been proposed as gamma-ray binaries but they have yet to be detected at GeV or TeV energies (Dubus et al. 2017).

Based on current observations of HMXBs that have been detected at HE and/or VHE, there are two proposed models for the origins of these emissions, depending on the composition of the binary. The first model involves any HMXB with a rotation-powered pulsar and a massive companion. In such a system the relativistic wind from the pulsar interacts with the stellar wind from the massive companion, as well as the circumstellar disc if the massive companion is a Be star. The interactions between the pulsar and stellar winds create shocks that provide conditions for gamma-ray emission from non-thermal processes. However, there is currently no “standard model” for the radiative processes of such gamma-ray binaries (Dubus 2013). The second model for gamma-ray emission involves HMXBs where the massive companion star overflows the Roche lobe, in particular microquasars because of the jets that are launched from the accretion process. The highly relativistic nature of particles streamed from the jets creates an environment where gamma-rays may originate from the base of the jets at the compact objects or from shocks created by the jets interacting with the inter-stellar medium (ISM) (Dubus 2013). As mentioned previously (Sect. 1.3) there are currently only three microquasars that have had confirmed gamma-ray detections, two of which have only had confirmed detections at GeV, Cyg X-1 and Cyg X-3, while SS 433 has been detected at GeV and TeV energies with evidence that the TeV gamma-ray emissions originate from the lobes of the relativistic jets (Abeysekara et al. 2018). These systems are known as microquasars and not necessarily gamma-ray binaries because their X-ray luminosity is orders of magnitude higher than the gamma-ray luminosity (Dubus et al. 2017).

Despite over a decade of intense observations there are still a number of questions surrounding the inner workings of gamma-ray binaries. Since the nature of the compact object is unknown in most gamma-ray binaries it’s very difficult to build a “standard model” for the processes of gamma-ray emission from HMXBs. The nature of GeV and TeV emission from gamma-ray binaries does not seem to correlate well implying that both bands of the gamma-ray spectrum originate from different processes. Gamma-ray binaries are known to be highly efficient particle accelerators with, in the case of pulsar systems, gamma-ray luminosity that can match the spin-down luminosity on a daily scale and exceed it on shorter timescales by several orders of magnitude (Johnson et al. 2018). Exceeding the spin-down luminosity implies that there is some additional source of energy or an observed beaming effect. Recent

studies of the periastra of the gamma-ray binary PSR B1259-63 have provided new insight into the origin of this intense gamma-ray luminosity (see Ch. 4).

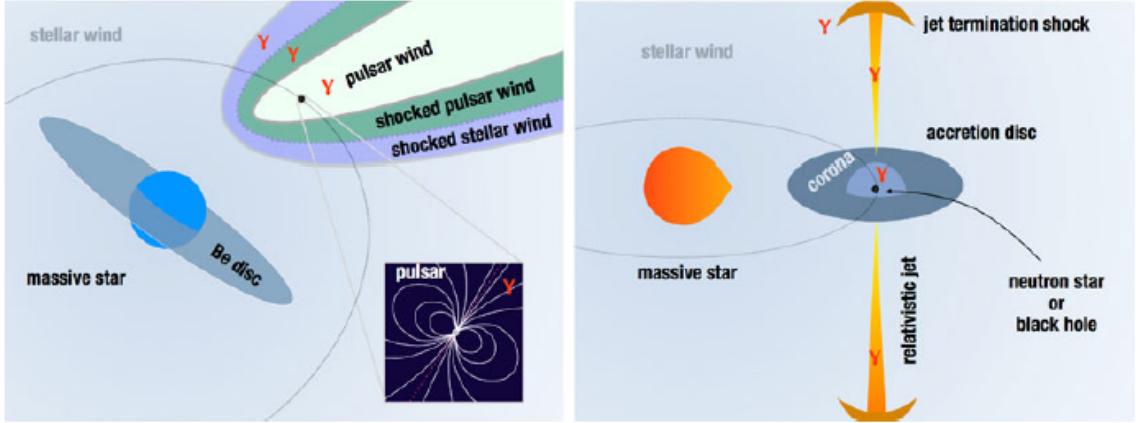


Figure 1.8: Illustration of the proposed models for gamma-ray binary systems. Left: Rotation-powered pulsar model. Right: Accretion-powered microquasar model (Dubus 2013).

1.5 Summary & Discussion

The accretion environment within XRBs, especially HMXBs, results in a hot and energetic environment that causes very luminous X-ray emission as well as the emission of other EM radiation. The emission in these systems occurs in different regions depending on the process of accretion, such as the accretion disc in RLO, an accretion wake in stellar wind accretion or destruction of the Be star disc in BeXRBs. There are also additional classes of these systems depending on the presence of additional features, such as the relativistic jets observed from microquasars or the VHE gamma-ray emission observed from gamma-ray binaries. The energetic environment and the potential presence of shocks from wind collisions can cause acceleration of particles that leads to more potential radiation processes other than the previously mentioned thermal and accretion emission. Understanding these processes is critical to fully modelling the observed emission of HMXBs.

Chapter 2

Radiation Processes of High Mass X-ray Binaries

As a result of the highly energetic environment of HMXBs, there are a number of different processes that occur causing the emission of EM radiation from accelerated charged particles at a wide range of different wavelengths. Classically, for non-relativistic particles, the power radiated by an accelerating point charge is given by the Larmor formula (see Eq. 2.1).

$$-\left(\frac{dE}{dt}\right) = \frac{2}{3} \frac{q^2 a^2}{c^3} \quad (2.1)$$

When correcting this formula for relativistic effects, the acceleration needs to be considered with regards to the components that are perpendicular a_{\perp} and parallel a_{\parallel} to the direction of the particle velocity. By considering the difference in how each component is affected by relativistic effects, the Larmor formula can be expressed relativistically by Eq. 2.2.

$$-\left(\frac{dE}{dt}\right) = \frac{2q^2}{3c^3} \gamma^4 (a_{\perp}^2 + \gamma^2 a_{\parallel}^2) \quad (2.2)$$

An important aspect of any radiation process to consider is the cooling time. This represents the timescale particles of a given energy will continue to radiate due to the radiation process. For any particle with energy E that is losing energy at a rate dE/dt the lifetime of said particle is calculated using Eq. 2.3.

$$\tau = \frac{E}{dE/dt} \quad (2.3)$$

Equations presented here for the processes of Synchrotron, inverse Compton and Bremsstrahlung radiation are cited from Blumenthal & Gould (1970) and Ch. 3 – 7 from Rybicki & Lightman (1986).

2.1 Synchrotron

When charged particles interact with an external magnetic field they experience an acceleration that is perpendicular to the direction of the magnetic field. The force on the particle caused by acceleration (Newton's 2nd Law) is equal to the Lorentz force on the particle from the magnetic field (Eq. 2.4).

$$\gamma m \frac{d\mathbf{v}}{dt} = q(\mathbf{v} \times \mathbf{B}) \quad (2.4)$$

As a result, the particles have a constant velocity in the direction of the magnetic field with an additional circular motion with a constant radius. This means the particles move in a spiral path with a constant pitch angle θ , which is the angle between the velocity of the particles \mathbf{v} and the magnetic field direction \mathbf{B} . The rotation of the particle movement has an angular gyrofrequency ω_g and a gyrofrequency ν_g that is represented by Eq. 2.5.

$$\omega_g = \frac{qB}{\gamma mc}, \nu_g = \frac{\omega_g}{2\pi} \quad (2.5)$$

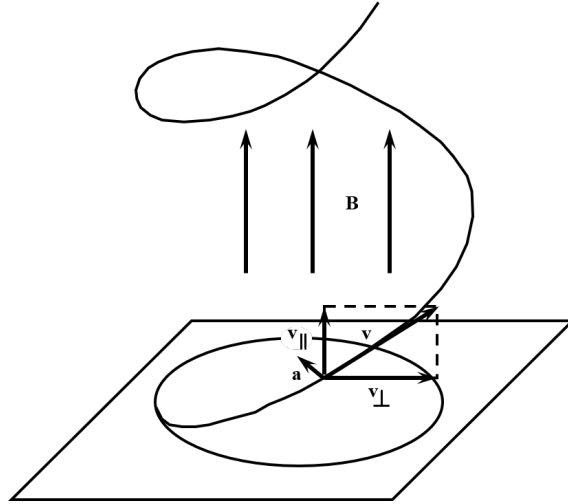


Figure 2.1: Diagram illustrating the helical motion experienced by charged particles in a magnetic field that causes synchrotron emission. Figure is a remade version of a figure from Rybicki & Lightman (1986).

In non-relativistic conditions, the radiation emitted as a result of this acceleration is called cyclotron radiation. The emission spectrum of cyclotron radiation produces a spike at a critical frequency equal to ν_g with additional lower peaks as harmonics spaced by $\Delta\nu = qB/mc$. If the particles are relativistic then the separation between harmonics becomes so small ($\Delta\nu = qB/\gamma mc$) that the emission spectrum is continuous. This is called Synchrotron radiation. The power emitted in

the form of synchrotron radiation is expressed in Eq. 2.6.

$$-\left(\frac{dE}{dt}\right) = \frac{2}{3} \frac{q^4 \beta^2 B^2 \gamma^2}{m^2 c^3} \sin^2 \theta \quad (2.6)$$

Given an isotropic distribution, the expression for synchrotron energy loss can be averaged by taking the magnetic energy density $U_B = B^2/8\pi$, the classic electron radius $r_0 = e^2/mc^2$ and the Thompson scattering cross section $\sigma_T = 8\pi r_0^2/3$. The Thomson scattering cross section is derived from the classical limit where EM waves are scattered by free electron (Rybicki & Lightman 1986). For the case of an isotropic distribution of the pitch angle, the term $\sin^2 \theta$ can be averaged to $2/3$ over all solid angles. Taking all these factors into account, the average energy loss caused by synchrotron radiation from electrons can be written as Eq. 2.7.

$$-\left(\frac{dE}{dt}\right) = \frac{4}{3} \sigma_T c U_B \beta^2 \gamma^2 \quad (2.7)$$

For any particle of energy E the lifetime of the particle undergoing synchrotron emission is shown by Eq. 2.8.

$$\tau = \frac{E}{dE/dt} = \frac{3mc}{4\sigma_T U_B \beta^2 \gamma} \quad (2.8)$$

The observed spectrum of synchrotron radiation from a single electron is characterised by a critical frequency ν_c (Eq. 2.9). Due to relativistic effects, this critical frequency is greater than the gyration frequency ν_g (Eq. 2.5) by a factor of γ^3 .

$$\nu_c = \frac{3}{2} \nu_g \gamma^3 \sin \theta = \frac{3}{2} \frac{qB \sin \theta}{mc} \gamma^2 \quad (2.9)$$

The Fourier transform of the electric field of the synchrotron pulses is proportional to the spectrum $dW/d\omega d\Omega$. By integrating the spectrum over the solid angle and remembering the previous expressions for synchrotron losses Eq. 2.6 and ν_c Eq. 2.9 the emitted spectrum of a single electron can be calculated by the following Eq. 2.10:

$$P(\nu) = \frac{\sqrt{3} q^3 B \sin \theta}{mc^2} F\left(\frac{\nu}{\nu_c}\right) \quad (2.10)$$

where if $x = (\nu/\nu_c)$ then:

$$F(x) = x \int_x^\infty K_{5/3}(z) dz. \quad (2.11)$$

$K_{5/3}$ is a modified Bessel function of order $5/3$ (Blumenthal & Gould 1970). An example of such a spectrum is shown in Fig. 2.2.

The emission spectrum of electrons sharply peaks at a frequency close to ν_{crit} .

The overall shape of the emission spectrum is dependent on the electron energy spectrum. The energy spectrum emitted as a result of synchrotron radiation $J(\nu)$ can be derived based on the electron spectrum $N(E)$ (Eq. 2.12).

$$J(\nu)d\nu = \left(-\frac{dE}{dt} \right) N(E)dE \quad (2.12)$$

From this derivation, By integrating Eq. 2.12, for an electron population with a powerlaw spectrum $N(E) = \kappa E^{-p}$, the resultant synchrotron spectrum will also be a powerlaw spectral index of $\alpha = (p - 1)/2$.

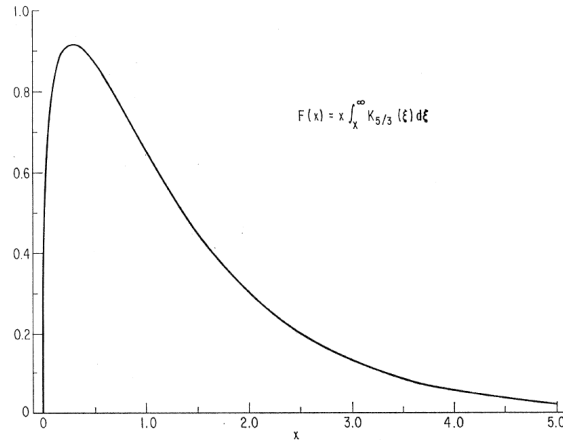


Figure 2.2: Spectrum of single electron as a result of synchrotron emission where $x = \nu/\nu_c$ (Blumenthal & Gould 1970).

2.2 Inverse Compton

Compton scattering refers to the phenomenon where a photon scatters from an interaction with a charged particle, usually electrons, which transfers energy from the photon to the particle causing an increase in wavelength. The increased wavelength of the photon λ_1 can be calculated using the following Eq. 2.13:

$$\lambda_1 - \lambda = \lambda_c(1 - \cos \theta) \quad (2.13)$$

where θ is the scattering angle of the photon and λ_c is the Compton wavelength defined by Eq. 2.14:

$$\lambda_c = \frac{h}{mc}. \quad (2.14)$$

However, the opposite can occur, under relativistic conditions, where the particle transfers energy to photon. This is known as Inverse Compton (IC) scattering. Consider the case of a photon with energy $\hbar\omega$ colliding with a relativistic electron as observed from the laboratory frame of reference S versus the rest frame for the

electron S' (see Fig. 2.3 for illustration). The energy of the photon in the frame S' is:

$$\hbar\omega' = \gamma\hbar\omega(1 + \beta \cos \theta) \quad (2.15)$$

where θ is the angle of incidence of the photon. If the energy of the rest frame photon is much less than the particle, $\hbar\omega' \ll m_e c^2$, then it undergoes Thomson scattering (see Fig. 2.4 for the distribution of photons under Thomson scattering). The rate of energy loss as a result of Thomson scattering can be calculated using:

$$-\left(\frac{dE}{dt}\right) = \sigma_T c U'_{rad} \quad (2.16)$$

where U'_{rad} is the radiation energy density in the electron rest frame. The difference between U'_{rad} and U_{rad} relates to the difference in photon arrival time at the origin of the lab frame. Through analysis this difference can be shown to be $\gamma(1 + \beta \cos \theta)$. If the radiation field in frame S is assumed to be isotropic then the total energy density seen in S' can be found by integrating the over the solid angle in S. This results in $U'_{rad} = \frac{4}{3}U_{rad}(\gamma^2 - \frac{1}{4})$. By substituting this value into Eq. 2.16 and subtracting the energy of the initial low-energy photons the total rate of energy loss due to IC is shown in Eq. 2.17.

$$-\left(\frac{dE}{dt}\right) = \frac{4}{3}\sigma_T c U_{rad} \beta^2 \gamma^2 \quad (2.17)$$

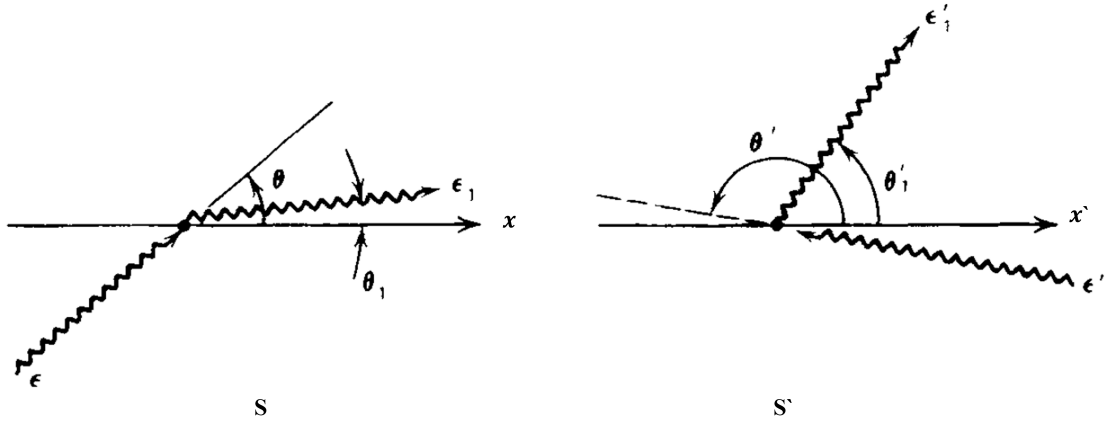


Figure 2.3: Sketch of the two frames of reference to consider when inverse Compton occurs between a photon and a relativistic electrons (Rybicki & Lightman 1986).

One may notice the expression for energy loss due to IC is almost identical to the synchrotron expression (Eq. 2.7). This is because both involve acceleration by an electric field on the particle, either due to interaction with a magnetic field in the synchrotron case or the electric fields of the incident photons in IC. As such the ratio of energy loss between synchrotron and IC is actually the ratio of the magnetic

energy density and the photon energy density (Eq. 2.18).

$$\frac{P_{synch}}{P_{ic}} = \frac{U_B}{U_{ph}} \quad (2.18)$$

Using the total energy loss of IC in Eq. 2.17, the cooling time as a result of IC losses is shown in Eq. 2.19.

$$\tau = \frac{E}{dE/dt} = \frac{3mc}{4\sigma_T U_{rad} \beta^2 \gamma} \quad (2.19)$$

Interestingly there is a fundamental lifetime limit for relativistic particles in the universe which can be calculated from this equation. The Cosmic Microwave Background (CMB) permeates throughout the Universe and thus relativistic particles can never escape its influence. The CMB is described as a perfect blackbody and so the energy density of the CMB is $U_{CMB} = aT^4 = 0.26 \text{ eV/cm}^3$. Using this value, the maximum lifetime of any relativistic particle against IC is $t_{max} = \frac{2.3 \times 10^{12}}{\gamma} \text{ yrs}$.

Determining the emission spectrum as a result of IC scattering is a complex calculation. From Blumenthal & Gould (1970), for an incident, isotropic photon field at a frequency ν_0 , the emission spectrum can be written as Eq. 2.20.

$$I(\nu) d\nu = \frac{3\sigma_T c N(\nu_0)}{16\gamma^4 \nu_0^2} \nu \left[2\nu \ln \left(\frac{\nu}{4\gamma^2 \nu_0} \right) + \nu + 4\gamma^2 \nu_0 - \frac{\nu^2}{2\gamma^2 \nu_0} \right] d\nu \quad (2.20)$$

In general, the average photon scattered through IC can be approximated to have been enhanced by a frequency of $\nu' = \gamma^2 \nu$. As a result, for a powerlaw distribution of electrons undergoing IC scattering there is a difference in the slope of the electron distribution and the emission spectrum. The same derivation used for synchrotron emission can be used for IC, as the only difference is the photon field density U_{ph} for IC in place of the magnetic field density U_B in synchrotron energy loss calculations. Thus, for an electron spectrum with slope $-p$, the IC spectrum slope is $-(p-1)/2$. This is based on the same derivation previously described for synchrotron radiation (see Sect. 2.1 and Eq. 2.12).

2.3 Bremsstrahlung

Bremsstrahlung radiation, sometimes called “braking/deceleration radiation”, is EM radiation that is produced due to the deceleration of a charged particle as the result of deflection by another charge particle. A full understanding of the intricacies of Bremsstrahlung emission requires a complicated quantum treatment. What is presented here are classical treatments to derive the energy release of Bremsstrahlung taken from Rybicki & Lightman (1986) and Aharonian (2004).

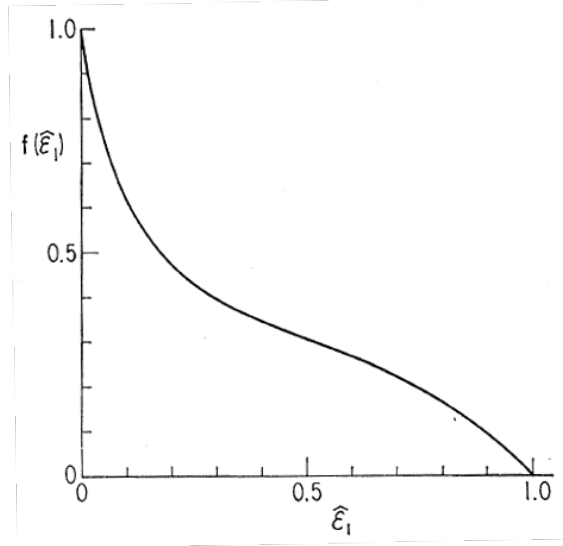


Figure 2.4: Scattered photon distribution function of IC in the Thomson scattering limit (Blumenthal & Gould 1970).

The emission of Bremsstrahlung radiation does not occur with like particles, i.e. electron-electron or proton-proton. Instead we consider electron-ion collisions where the electron is the primary radiator and as the ion/nucleus is comparatively large compared to the electron it can be treated as fixed. An important parameter in deriving Bremsstrahlung processes is the collision parameter b . This is the distance of closest approach between the electron and ion.

2.3.1 Thermal Bremsstrahlung

In the case of thermal Bremsstrahlung, there is a thermal distribution of speeds where collisions can occur. For an isotropic distribution of velocities, the probability that a particle has a velocity v in the range dv can be expressed by:

$$dP \propto v^2 \exp\left(-\frac{mv^2}{2kT}\right) dv \quad (2.21)$$

where k is the Boltzmann constant and T is the temperature. From derivations shown in Rybicki & Lightman (1986) the total power per unit volume emitted by thermal Bremsstrahlung for a population of electrons and ions of charge Ze with number densities n_e and n_i respectively is shown by:

$$\frac{dW}{dt dV} = \left(\frac{2\pi kT}{3m}\right)^{1/2} \frac{32\pi e^6}{3hmc^2} Z^2 n_e n_i \bar{g}_B. \quad (2.22)$$

The parameter \bar{g}_B is the frequency average of the velocity averaged Gaunt factor. The Gaunt factor is a specific function of the velocity of electrons and the frequency

of the emitted photons (Rybicki & Lightman 1986).

2.3.2 Relativistic Bremsstrahlung

Under relativistic conditions, a full understanding of Bremsstrahlung requires the use of quantum electrodynamics. However, the classical treatment used to describe thermal Bremsstrahlung can be used as a reasonable approximation that provides useful insight. Similar to the treatment for Compton scattering, the emission caused by relativistic Bremsstrahlung can be derived by considering a lab frame with $dW/d\omega$ and an electron rest frame with $dW/d\omega'$. From derivations by Rybicki & Lightman (1986), the emission from relativistic electrons colliding with ions with a collision parameter b is shown by Eq. 2.23:

$$\frac{dW}{d\omega} = \frac{8Z^2e^6}{3\pi b^2c^5m^2} \left(\frac{b\omega}{\gamma^2c}\right)^2 K_1\left(\frac{b\omega}{\gamma^2c}\right) \quad (2.23)$$

where K_1 is a modified Bessel function of order 1, similar to when used for the synchrotron spectrum. For a plasma with electron density n_e and ion density n_i , the previous equation can be expressed for the total emission per unit volume (erg/cm³/s) as shown in Eq. 2.24. This representation of the emission is valid as long as $\hbar\omega \ll \gamma mc^2$.

$$\frac{dW}{dt dV d\omega} \sim \frac{16Z^2e^6n_en_i}{3c^4m^2} \ln\left(\frac{0.68\gamma^2c}{\omega b_{min}}\right) \quad (2.24)$$

2.3.3 Bremsstrahlung Cooling

From Aharonian (2004), the average energy loss of electrons of energy E undergoing Bremsstrahlung losses $-(dE/dt) \propto E$. As the loss is directly proportional to the electron energy, the cooling time is therefore independent of the electron energy and can be approximated by:

$$\tau \simeq 4 \times 10^7 \left(\frac{n}{1\text{cm}^{-3}}\right) \text{yr} \quad (2.25)$$

where n is the number density of the ambient gas. This implies that Bremsstrahlung losses do not alter the initial electron spectrum. This is in stark contrast to the losses caused by synchrotron and IC (Eq. 2.8 & 2.19), where the cooling time is inversely proportional to γ . Thus while Bremsstrahlung losses will not alter the electron spectrum, both synchrotron and IC will influence the initial electron spectrum.

2.4 Summary & Discussion

Synchrotron, IC and Bremsstrahlung are all radiation processes that can occur within environments containing highly relativistic particles. Synchrotron and IC can be closely tied together due to the fundamental similarity in emission being due to particle interactions with an external EM field. In HMXBs, this close relation is important to understanding how emission at different observed energies act as counterparts in these systems. It is also critical to modelling how the spectrum of injected particles in the system, normally electron, changes due to energy losses from these processes. Observing the radiation from these processes, along with the other emission due to accretion and thermal processes, requires multiple telescopes operating across the EM spectrum. Some bands of the EM spectrum have new missions planned in the future, which may provide a new opportunity to improve our understanding of the emission from HMXBs.

Chapter 3

Telescopes and Future Missions

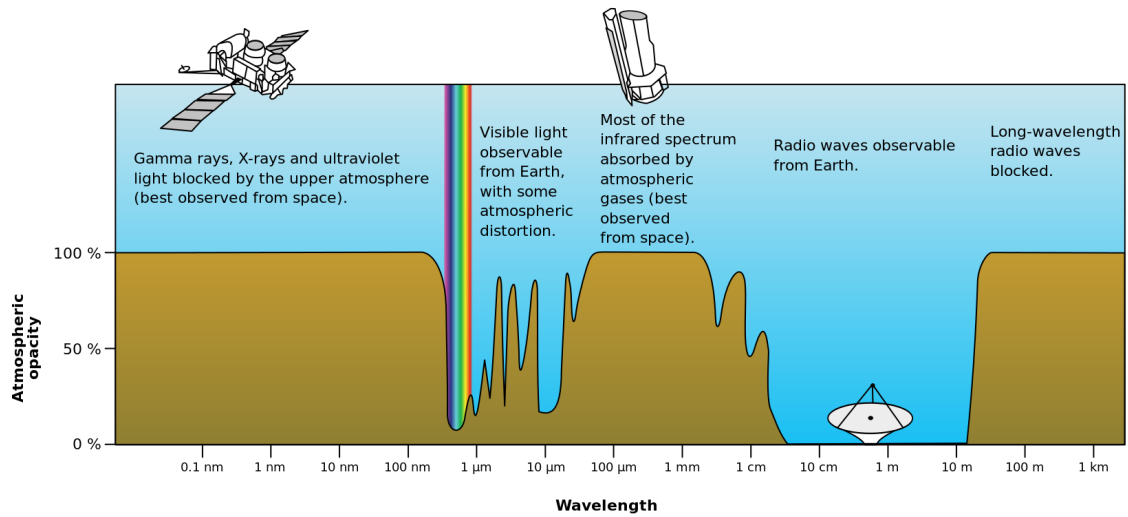


Figure 3.1: Diagram illustrating the opacity of Earth's atmosphere for electromagnetic radiation at different wavelengths (Credit: NASA).

With the advent of multi-wavelength astronomy over the course of the last century, different methods have been required to observe specific bands of the broadband spectrum. In particular, large portions of the electromagnetic spectrum can not be observed from the surface of the Earth as the Earth's atmosphere is opaque to these radiation bands, as illustrated in Fig. 3.1. At X-ray and GeV gamma-ray bands, this limitation has been combatted using orbital observatories such as Chandra and XMM-Newton for X-ray and the Fermi Space Telescope for GeV (Sec. 3.1). Due to the age of current X-ray observatories, future missions are in development to continue X-ray astronomy at new levels of resolution and sensitivity, such as XRISM and Athena (Sec. 3.2). At the VHE gamma-rays, where photons reach TeV energies, the typical flux of these sources corresponds to ~ 0.2 photons/m²/yr at 1 TeV. These statistics are so low that orbital observatories with limited fields of view become less feasible. Instead ground-based arrays are used that monitor for Cherenkov

flashes from atmospheric particle showers caused by the interactions of TeV photons within the atmosphere. Such arrays include H.E.S.S., MAGIC, VERITAS and the upcoming Cherenkov Telescope Array (Sec. 3.3).

3.1 Fermi Gamma-ray Space Telescope

The Fermi Gamma-ray Space Telescope is an orbital gamma-ray observatory in a low Earth orbit (see Fig. 3.2). It was launched on the 11th June 2008 with an original mission lifetime of five years. This was extended to ten years in 2013 and despite passing the end of the mission extension, in 2019 the mission was given another extension into 2022 with further extensions possible. Fermi contains two scientific instruments, the Large Area Telescope (LAT) (Atwood et al. 2009) and the Gamma-ray Burst Monitor (GBM) (Meegan et al. 2009). The Instrument Response Functions (IRFs) for an instrument represents the mapping between the incoming photon flux and the detected events. The current Fermi IRFs are based on the Pass 8 LAT data (Atwood et al. 2013) which was first released in June 2015. This data set was further revised to improve the model for the isotropic background (Bruel et al. 2018).

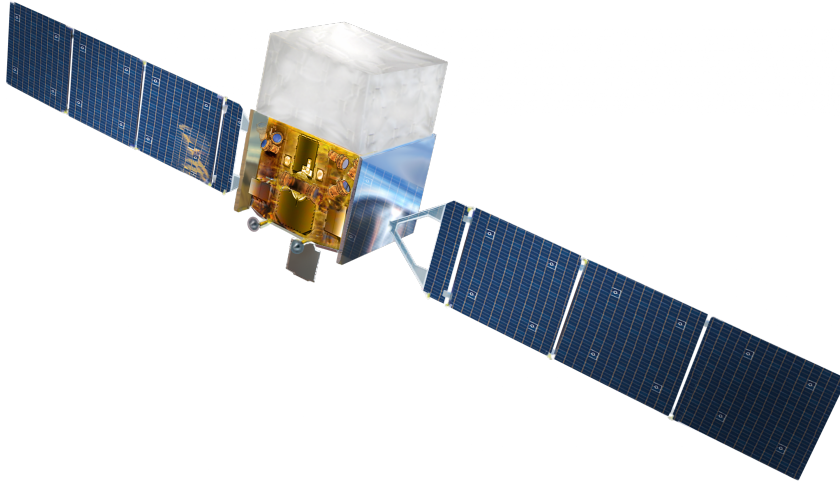


Figure 3.2: Artist concept of the Fermi telescope spacecraft (Credit: NASA).

LAT was primarily built as an instrument for resolving the gamma-ray sky, identifying gamma-ray sources and providing the ability to study the GeV spectrum of these sources. It is a gamma-ray detector based on particle pair production that detects photons in the energy range of 30 MeV up to ~ 1 TeV with a view of 20% of the sky at any given time. The pair production detection method used by Fermi-LAT is done using a detector with multiple layers of material and sensors (see Fig. 3.3). The anticoincidence detector is sensitive to charged particles to prevent interference from cosmic rays. The conversion foil consists of high atomic mass nuclei, in this case

tungsten, in order to induce pair production in the incident photons. The e^\pm pair then passes through several layers of silicon-strip particle tracking detectors before hitting a calorimeter where the energy of the pair is measured. This procedure results in a characteristic gamma-ray signature for Fermi-LAT detections, where there is no signal in the anticoincidence shield, two particles are tracked from the same point of origin within the detector and an electromagnetic shower is detected on the calorimeter.

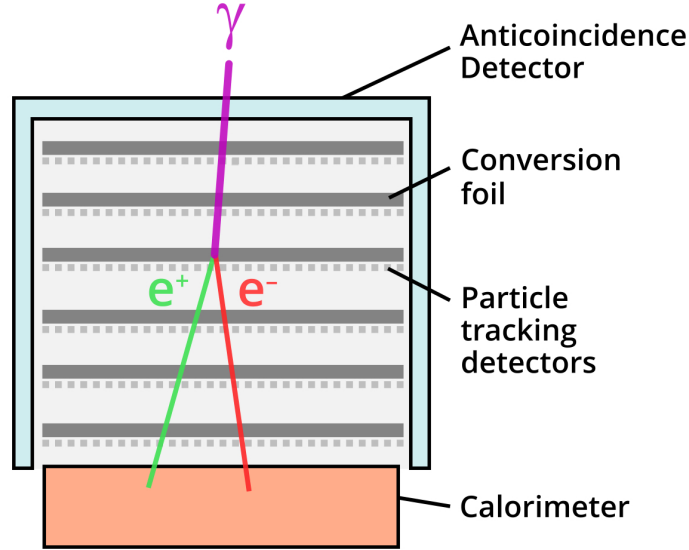


Figure 3.3: Diagram of the Fermi-LAT illustrating the pair production detection method. (Credit: NASA’s Goddard Space Flight Centre).

In the conversion plane of the incident photon, the resulting pair components undergo multiple scatterings causing an angular deflection that results in low limit to the angular resolution, especially at lower energies. The per-photon angular resolution is highly energy dependent where it is $\sim 5^\circ$ at 100 MeV, decreasing to 0.8° at 1 GeV and finally to $\sim 0.1^\circ$ at 20 GeV with an asymptotic limit based on energy variation at approximately $E^{-0.8}$. The difference in resolutions, for both the front and back portion of the detector, are shown in Fig. 3.5. This relates to the difference in effective area of Fermi-LAT with respect to energy where there is a factor of three difference between 100 MeV and 1 GeV (see Fig. 3.4). The difference in PSF between the front and back of the detector is due to a difference in the radiation length of the 12 “FRONT” and the 4 “BACK” tungsten converters causing different scattering between the portions of the instrument.

Observations with Fermi-LAT have proven invaluable in providing a new window into the study of HMXBs. The gamma-ray binary 1FGL J1018.6-5856 was discovered by searching for periodic modulations in all sources of the first Fermi-

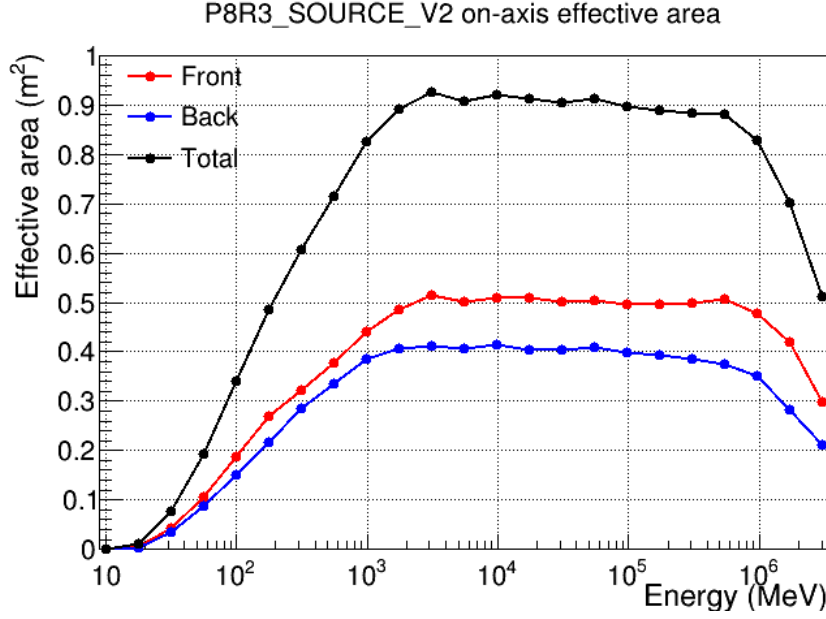


Figure 3.4: The effective area of Fermi-LAT with respect to energy under the latest IRFs (P8R3) assuming normal incidence photons (Bruel et al. 2018).

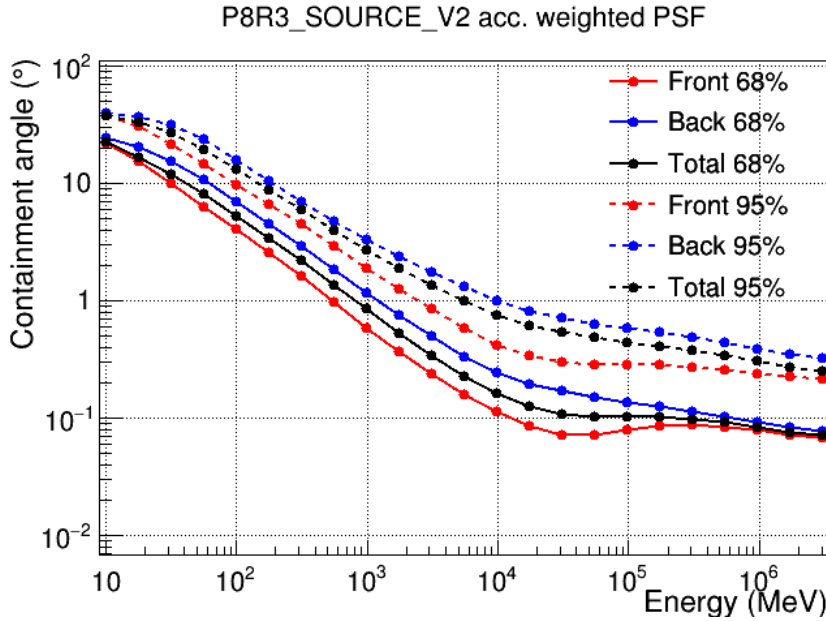


Figure 3.5: Point Spread Function (PSF) of Fermi-LAT showing the 68% and 95% containment angles (angular resolution) for the front and back of the detector (Bruel et al. 2018).

LAT source catalog (Collaboration 2012) and the system LMC P3 was not identified as a gamma-ray binary until association was found in the third Fermi-LAT catalog (Corbet et al. 2016). Fermi-LAT remains the most useful, and only, telescope for observing the GeV spectrum of gamma-ray binaries, such as the recent periastrons of PSR B1259-63 (see Ch. 4) and GeV emission detections from microquasars such as SS433 (see Section 6.1.1 for more details) (Bordas et al. 2015; Rasul et al. 2019).

3.2 Athena X-ray Telescope

The Advanced Telescope for High-ENergy Astrophysics (Athena) is a next generation X-ray telescope currently under development and scheduled for launch in the early 2030s (see Fig. 3.6 for illustration). Athena will perform pre-planned observations of up to 300 celestial regions in a year. A Target of Opportunity (ToO) mode will be capable of maneuvering the observatory for random events. The observatory will consist of a single X-ray telescope with a focal length of 12 m with an effective area of 2 m^2 at 1 keV (Nandra et al. 2013). The mirror for Athena will be based on the European Space Agency’s (ESA) Silicon Pore Optics (SPO) technology (Collon et al. 2019). SPO has a high collection area to weight ratio while still maintaining high angular resolution (see Fig. 3.7 for diagram of the Athena mirror). The mirror will be movable in order to focus the X-ray emission onto either of Athena’s two primary instruments: the Wide Field Imager (WFI) (Meidinger et al. 2017) and the X-ray Integrated Field Unit (X-IFU) (Pajot et al. 2018).

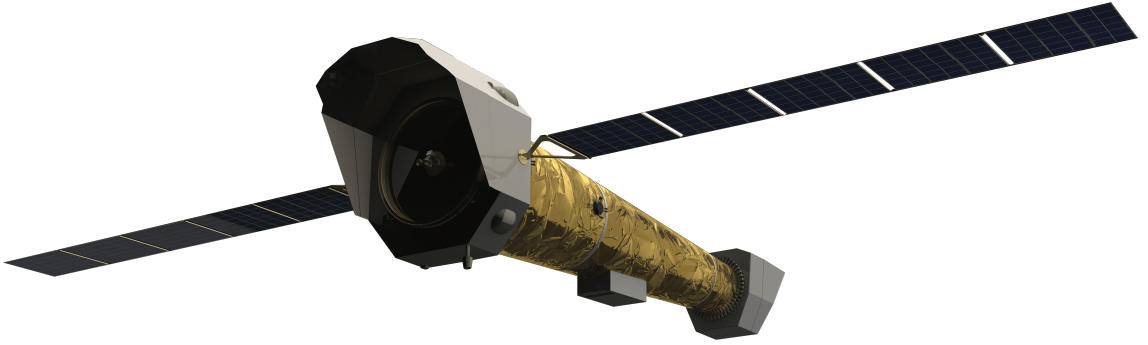


Figure 3.6: Illustration of the current model for the completed Athena space observatory (Credit: X-IFU Consortium).

X-IFU is a cryogenic X-ray imaging spectrometer and will be Athena’s primary tool for spatially resolved X-ray spectroscopy. X-IFU is planned to operate within the energy range of 0.2-12 keV with a 2.5 eV energy resolution and a $5'$ diameter field of view. The on-axis angular resolution of the detector will $5''$ with this increasing to $10''$ at a $25'$ radius. The effective area of X-IFU will be orders of magnitude higher than any currently operational instrument and still an order of magnitude higher than upcoming X-ray missions such as the X-ray Imaging and Spectroscopy Mission (XRISM) (see Fig. 3.8 for a visual comparison). The defocusing capabilities of Athena’s optics allows for the focal beam of the telescope to be spread over all the sensors of the X-IFU detector. This allows X-IFU to observe very bright X-ray sources. In order to achieve these performance requirements, X-IFU will use a large array of Transition Edge Sensors (TES) (Irwin et al. 1996) operating at $\sim 90 \text{ mK}$. TES are cryogenic energy sensors that are based on the principle of superconductivity and thus require these low temperatures to operate effectively as

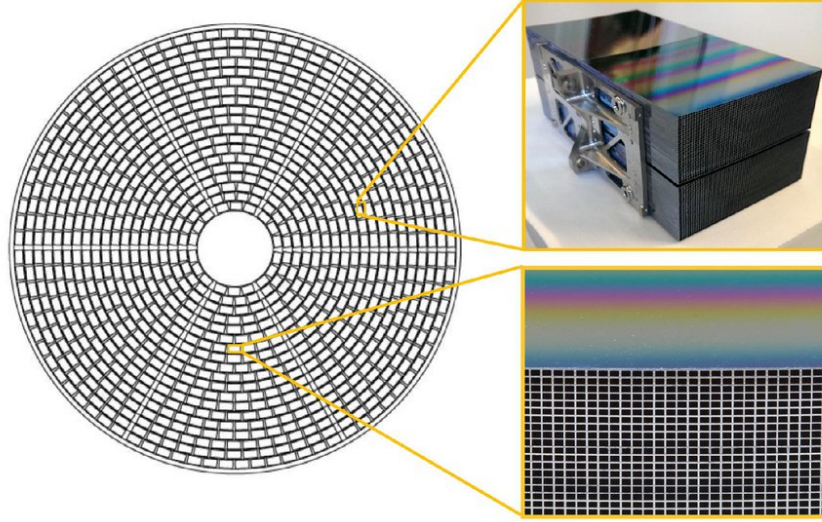


Figure 3.7: A diagram of the layout of SPO that will be used for the mirror on Athena. The images on the right show pictures of the SPO material that will be used (Wille et al. 2015).

the change in temperature due to X-ray photons is what causes detections. X-IFU successfully passed its Preliminary Requirements Reviews as of the 11th April 2019.

Athena is an ESA mission within the ESA Cosmic Vision program under the scientific theme 'The Hot and Energetic Universe'. The mission is planned to undertake three key scientific objectives (Nandra et al. 2013):

1. Determine how and when large-scale hot gas structures formed and evolved to the present day in the Universe.
2. Examine and determine the physical processes responsible for BH growth and perform a complete census of BH growth in the Universe.
3. Provide a new and unique contribution to future astrophysics by exploring all high-energy phenomena in all astrophysical contexts, both currently known and those yet undiscovered.

Under the scientific theme 'The Hot and Energetic Universe' there are a number of observatory science goals for X-IFU. The combination of wide field imaging with WFI, which will have a field of view of $40' \times 40'$ and high resolution spectroscopy with X-IFU in the X-ray band will be instrumental in answering questions relating to the structure of the dense Warm Hot Intergalactic Medium (Kaastra et al. 2013) and the accretion structure of Supermassive BHs (Dovciak et al. 2013).

In line with the third scientific objective, Athena will provide a dramatically enhanced view into the X-ray emissions of HMXBs with the ability to resolve these

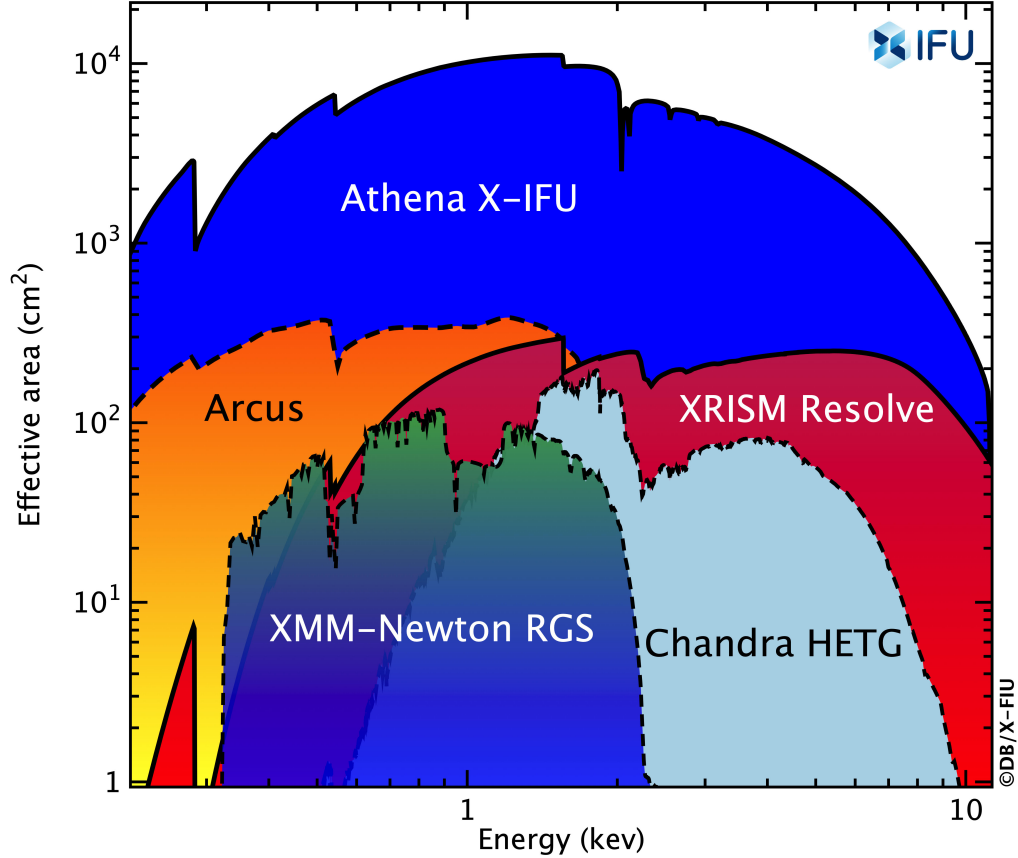


Figure 3.8: Effective area of Athena X-IFU compared to one of the XRISM Resolve instrument, both being imaging spectrometers. The effective area of three dispersive spectrometers are also shown: two currently in operation, XMM-Newton RGS and Chandra HETG, and Arcus proposed to NASA as a MIDEX and currently completing its Phase A concept study (Credit: X-IFU Consortium).

systems on much shorter timescales which may present new methods for mapping the geometry of these systems. X-IFU’s energy resolution combined with its time resolution ($10 \mu s$) and sensitivity will allow for more in depth investigation into the underlying processes of the accretion physics in HMXBs. It also has the potential of providing new methods and opportunities to examine the structure of the accretion and stellar wind interactions in systems such as Vela X-1 (e.g. Amato et al. 2021).

3.3 Cherenkov Telescope Array

The Cherenkov Telescope Array (CTA) is a new ground-based gamma-ray observatory for TeV astronomy. Upon completion, CTA will be the most advanced imaging atmospheric Cherenkov telescope (IACT) in operation. IACTs operate by imaging short flashes ($5 - 20$ ns) of Cherenkov radiation that occur due to showers of relativistic charged particles produced when a VHE gamma-ray strikes the atmosphere. VHE photons undergo pair production in the presence of atmospheric molecules.

The resulting high-energy e^\pm pair immediately cause the emission of more gamma-ray photons through bremsstrahlung radiation. These photons go on to pair produce again and thus a cascade of charged particles follows that cause flashes of Cherenkov radiation due to the particles exceeding atmospheric speed of light. These cascades, or Air Showers, exist for $\sim 10^{-4}$ s and occur between 7 – 12 km high in the atmosphere (Völk & Bernlöhr 2009). An illustration of the light pool created by these showers is shown in Fig. 3.9.

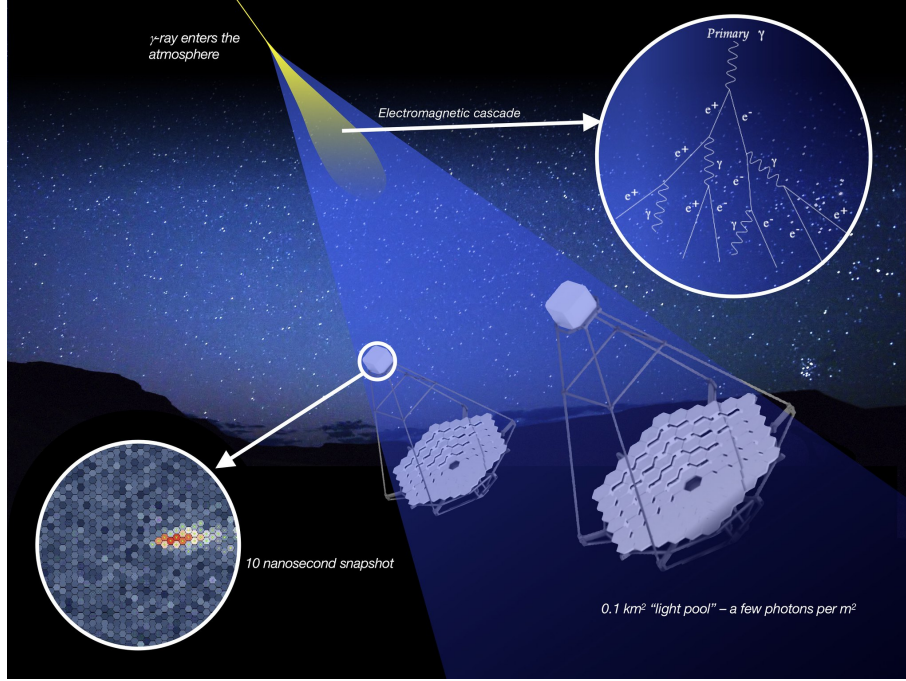


Figure 3.9: Diagram showing how CTA and other IACT capture the Cherenkov effect. The Cherenkov flashes caused by the particle shower are captured by snapshots on the telescope detectors. Comparing the direction of the snapshot on multiple telescopes allows the for the location and direction of the incident photon to be re-created (Credit: R. White (MPIK), K. Bernlohr (MPIK), DESY).

The Cherenkov flashes from the particle showers are captured by the detectors on CTA’s mirrors with snapshots, as shown in Fig. 3.9. The direction of the streak in this snapshot is dependent on the view each detector has of the shower and the subsequent light pool created by the flash (Bernlöhr 2009). Comparing the direction of the snapshot on other telescopes is what allows for the direction of the original photon to be recreated. This is where the direction all the different snapshots intersects in the field of view. Hence, more telescopes allows for more accurate tracking of the original photon and it also also for greater energy and angular resolution. These snapshots are also how CTA can ignore showers that are the result of cosmic ray interactions in the atmosphere. Cosmic rays creates much wider showers than VHE photons. This is because rather than pair production driving the shower, the cosmic ray collides with a nuclei in the atmosphere. One

of the products of the collision are pions, which either decay into gamma-rays or collide with other atmospheric particles. This cascade is much wider than that caused by VHE gamma-rays and thus, the shape of the snapshot of such showers is more complex than the narrow streak caused by VHE photon originating showers (Bernlöhr 2009).

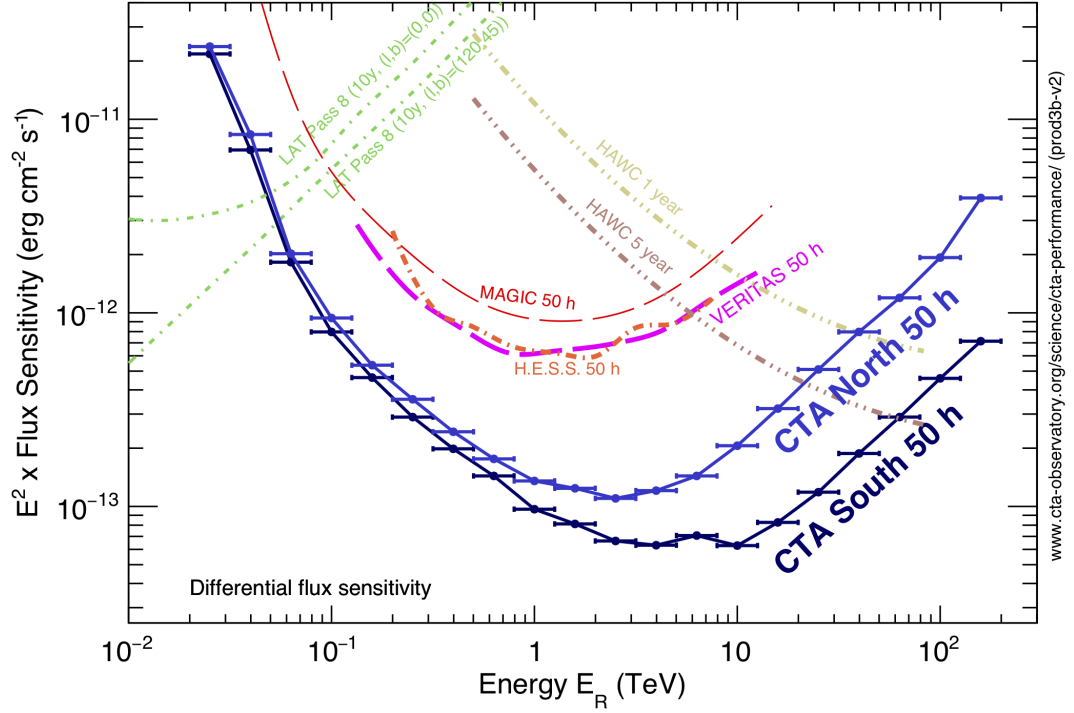


Figure 3.10: Differential sensitivity comparison between CTA, currently operational IACTs (MAGIC, VERITAS, H.E.S.S.), HAWC and Fermi-LAT. (Credit: CTA Consortium & Observatory).

The CTA will be capable of sensitivities an order of magnitude higher at 1 TeV than any of the current major IACTs (i.e. H.E.S.S., MAGIC and VERITAS). This is shown in the plot of the differential flux sensitivity of these observatories in Fig. 3.10. It will have better coverage of the sky than current telescopes because it will consist of two large array sites: one in the northern hemisphere on the island of La Palma, Spain and one in the southern hemisphere at Paranal, Chile. There will be three categories of telescopes used for the array: Small-Sized Telescopes (SST), Medium-Sized Telescopes (MST) and Large-Sized Telescopes (LST), see Fig. 3.11 for current designs. Between the two arrays, CTA will consist of over 100 telescopes where the LSTs provide sensitivity at the lowest energies and the SSTs at the highest. The array will detect gamma-rays at a total energy range 20 GeV – 300 TeV (Mazin 2019).

CTA will be able to address a wide range of topics in modern astrophysics and these topics can be grouped into three primary themes (The CTA Consortium 2019):

1. Understanding the Origin and Role of Relativistic Cosmic Particles.
2. Probing Extreme Environments.
3. Exploring Frontiers in Physics.

Under the theme of ‘Probing Extreme Environments’ CTA will provide a new view of HMXBs that have been detected at TeV energies and possibly discover new binaries at TeV energies. This includes both gamma-ray binaries and microquasars that have been detected at TeV energies as current IACTs can confirm detections from these systems but are unable to investigate variation on the timescale of the orbits or flaring of these systems. For example, the gamma-ray binary PSR B1259-63 has been detected at TeV energies by H.E.S.S. during periastron, however, H.E.S.S. has been unable to observe the system during the entire periastron passage so the variability of TeV emissions during this period is not fully known (Abramowski et al. 2013; Romoli et al. 2015). In the case of microquasars, SS433 was detected at TeV energies after nearly three years of observations by HAWC (Abeysekara et al. 2018) and the MAGIC detector has potentially detected TeV flaring from Cygnus X-1 (Zdziarski et al. 2009). With the proposed sensitivity of CTA, there is an opportunity to resolve the TeV emission from these sources with significantly less exposure time and for improved spectral modelling of TeV energies from these HMXB sources.

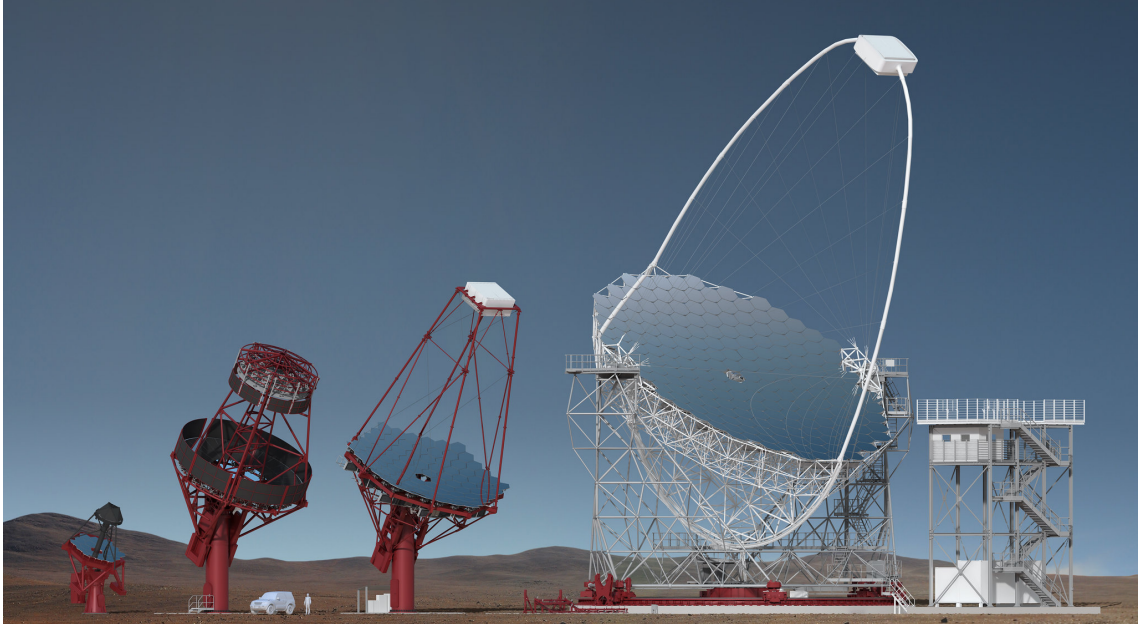


Figure 3.11: From left to right shows the SST, MST (two prototype designs are being tested) and LST for CTA (Credit: Gabriel Pérez Diaz, IAC).

3.4 Data Analysis Software

The work I will present in this thesis would not have been possible without the analysis, modelling and simulation software that were used as part of my research. Here I wish to provide some descriptions of the most important programs that were used, why they were used and some of the simpler principles behind how the software works.

3.4.1 Fermitools

Fermitools is the current analysis software used to analyse and model observational data from the Fermi-LAT (Fermi Science Support Development Team 2019). Due to the large PSF of Fermi-LAT (Fig. 3.5), data selection for Fermi analysis is often within a region of interest (ROI) of $\leq 15^\circ$. Using the Fermi source catalogue (Abdollahi et al. 2020), the analysis is performed with a spatial-spectral source model that includes the spatial and spectral information of all known sources within the selected ROI. Often sources within another few degrees outside the ROI are included as these can contribute to the modelling of sources within the ROI.

The first few years of observations with Fermi-LAT revealed a wealth of information about the gamma-ray sky at GeV energies. All-sky maps revealed diffuse GeV emission throughout the galactic plane as well as an isotropic diffuse background, which is thought to originate from extragalactic sources and dark matter annihilation (Di Mauro & Donato 2015). The all-sky map for the first 5 years of Fermi-LAT data is shown in Fig. 3.12. Modelling these backgrounds is crucial to Fermi-LAT data analysis and is constantly being revised and improved as the years of observation go on. As of writing, the latest background models are included in the Pass 8 (P8R3) IRFs.

The spatial-spectral model of all sources is fitted to the Fermi-LAT data using a maximum likelihood estimation. This is a method of estimating the parameters of a model given a set of data, as well as attributing gamma-rays detected to the relevant sources based on the direction of detections. The idea is that the free parameters of the spatial-spectral source model are tested to find the point in parameter space that maximizes what is called the likelihood function, this is the maximum likelihood estimation. The result of this estimation is that the spectral model parameters of the listed sources within the ROI are updated to fit the selected observational data. The source spectral models can vary from a simple powerlaw to a more complex exponential cut-off powerlaw. From the likelihood analysis, the photon or energy flux and the test statistic of each listed source can be calculated along with the fitted spectral model parameters. Running multiple likelihood analysis for data of different binning can be done to develop the lightcurve and/or spectrum for a selected source.

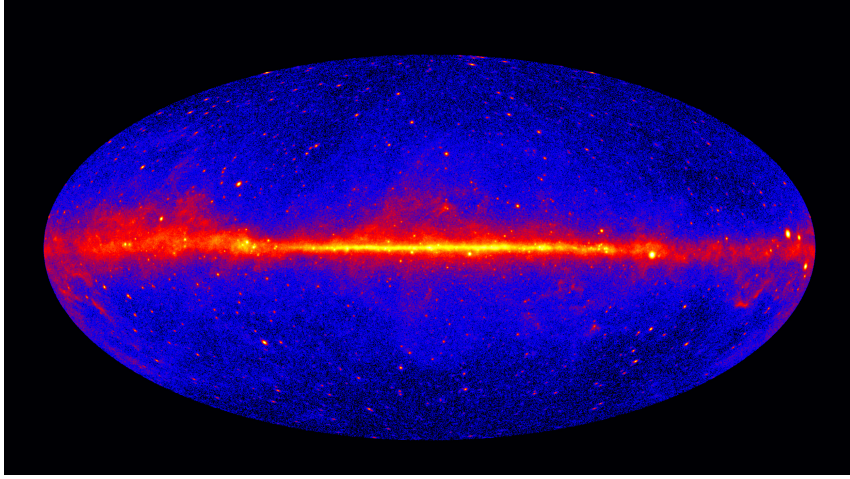


Figure 3.12: All-sky map for energies > 1 GeV made from the first 5 years of Fermi-LAT observations where the central band marks the plane of the Milky Way galaxy (Credit: NASA/DOE/Fermi LAT Collaboration).

3.4.2 SIXTE

Simulating the observations of X-ray telescopes is done with the Simulation of X-ray Telescopes (SIXTE) software package (Dauser et al. 2019). SIXTE is a generic, mission-independent, Monte Carlo simulation toolkit for X-ray astronomical instrumentation. It is used in conjunction with the Simulation Input (SIMPUT) software that stores information on targets to be observed in a detector independent format (Dauser et al. 2019). The software uses calibration files such as the PSF, Redistribution Matrix File (RMF) and Auxiliary Response File (ARF) in order to run efficient simulations at relatively high speeds. SIXTE can be used for simulations of current instruments such as XMM-Newton but is most used in the simulation of future telescope missions, such as Athena.

In order to run simulations with SIXTE, source(s) details need to be compiled in the SIMPUT file. Information that's required for any source includes position (RA, DEC), energy band, flux, spectral information and lightcurve information, if any periodicity is to be implemented. Defining the spectral information of a source can be done using built-in SIMPUT tools to define absorption, a powerlaw, a blackbody and/or a gaussian line for the iron $K\alpha$ line (6.4 keV). For sources with a more complex or variable spectrum, spectral models can be built in modelling software such as XSPEC (Dorman et al. 2003) or ISIS (Houck & Denicola 2000) and input into a SIMPUT file by manually creating a FITS file in the SIMPUT format. This can be done to make a source with different spectra at varying intensity during specified periodic phases.

With a complete SIMPUT file for the source of interest, SIXTE can simulate an observation of the source for a specified exposure time and an instrument based on

the specified calibration files. This creates a list of observed photon events. From here, SIXTE can be used to create an image based on the simulation or spectral files for X-ray spectral analysis of simulations. For future X-ray missions, such as Athena, modelling well-known X-ray sources and simulating observations in this manner allows for testing of the resolution and sensitivity of the instrument and gives an expectation of what new features of a system may be observed or new methods of observational study that may be possible.

3.4.3 CTOOLS

Ctools is a software package used for the analysis of Cherenkov telescope data (Knödlseider et al. 2016). Ctools can also be used to simulate observations for CTA in preparation for the array’s completion. Much like Fermitools, ctools requires the use of spatial-spectral source models for a large ROI in order to accurately model and spatially resolve all sources within an given ROI. In the case of IACTs, not exclusively CTA, this is also needed to account for the significant view of the the sky of which the array will be capable. In the case of simulating observations with CTA, these spatial-spectral source models can be used as input for simulations along with periodicity files for sources with a known periodicity.

Once an observation has been simulated for the selected list of sources, the procedure of the data analysis is similar to Fermitools. Event selection is used to select the relevant energy range, ROI, time-span etc and once more a maximum likelihood estimation is used to fit a source model to the simulated data selection. Ctools also includes tools to generate lightcurves and spectra from a fitted model rather than running multiple likelihood analyses for binned event selections as required using Fermitools. Simulations of CTA observations gives an idea as to what level of exposure is required to resolve the variability of transient sources such as gamma-ray binaries and microquasar.

3.5 Summary & Discussion

As the only current GeV astronomy, Fermi-LAT is a necessary instrument for observing and modelling the GeV emission from gamma-ray binaries. While the limited angular resolution of the mission makes imaging systems in GeV impractical, the constant surveying of the sky allows for a large collection of observational data from gamma-ray sources that is sufficient for studying the variability and spectrum. By comparison, current X-ray and TeV gamma-ray instruments do not have the capability to observe and resolve the spectral variability of HMXBs. Thus the development of the future missions the Athena X-ray telescope and the Cherenkov Telescope Ar-

ray provide a lot of promise to improve our capabilities to further study HMXBs. The Athena X-IFU will have energy resolution and sensitivity that may be able to resolve the change in fine spectral details in eclipsing HMXBs (see Ch. 5) and the CTA will have sensitivity that is orders of magnitude improved to current IACTs that it may be capable of making detections of transient sources that currently take years within hours (see Ch. 6).

Chapter 4

Fermi Analysis of PSR B1259-63

Over the last decade, the periastra passages of PSR B1259-63 (2011, 2014, 2017, 2021) have been intensely monitored at different energies which has revealed new features previously not observed. In this chapter, I present the findings from our group's analysis of the 2017 periastron, with which we developed a new model of the system and the application of this model to the initial findings of the 2021 periastron observations. As a part of my research, I conducted the analysis and modelling of the GeV data from Fermi-LAT from the 2017 periastron (Chernyakova et al. 2020) and assisted in the radio observation of the 2021 perisatron with ATCA (Chernyakova et al. 2021).

4.1 PSR B1259-63

PSR B1259-63 is a gamma-ray binary that has been intensely studied at high energies since the discovery of such radiation from the system (Kaspi et al. 1995). The system consists of a 47.8 ms radio pulsar orbiting a Be star LS 2883 in a highly eccentric orbit ($e \sim 0.87$) with a period of 1236.7 days or ~ 3.4 years (Johnston et al. 1992). Up until the discovery of the binary nature of the pulsar PSR J2032+1427 (Lyne et al. 2015), PSR B1259-63 was the only gamma-ray binary system with TeV emission in which the nature of the compact object was known.

The orbit of the pulsar brings it within ~ 0.9 AU of the Be star at periastron (Moldón et al. 2011). The circumstellar disc of the Be star is inclined with respect to the pulsar orbital plane by $10 - 40^\circ$ (Melatos et al. 1995), so the pulsar crosses and interacts with the disc twice during the periastron passage. The geometry of the system is shown in Fig. 4.1. During most of the orbit of the system, persistent X-ray emission is observed due to interaction between the Be star and pulsar wind (Chernyakova et al. 2009) as well as pulsed radio emission from the millisecond pulsar. However, within a few months centred on the periastron, unpulsed radio, enhanced X-ray, GeV and TeV emission is observed (Chernyakova et al. 2014;

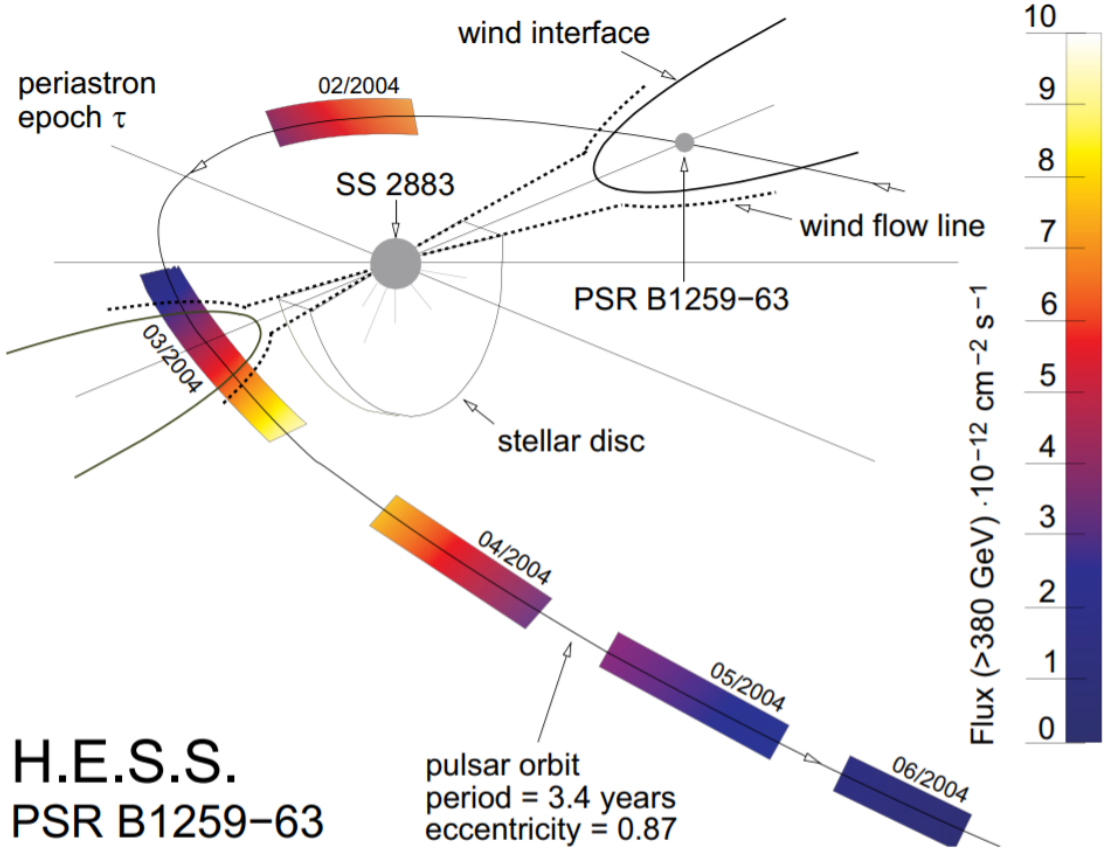


Figure 4.1: Sketch of the orbit of PSR B1259-63 around the periastron (Aharonian, F. et al. 2005). The colour gradient shows the integral TeV flux of H.E.S.S. observations from Aharonian, F. et al. (2005).

Caliandro et al. 2015). The disappearance of the pulsed radio emission is due to the pulsar being obscured by the Be circumstellar disc between the two crossings. The unpulsed radio and X-ray emission exhibits a two peak structure around periastron that appears to be a result of the pulsar crossing the circumstellar disc of the Be star, this structure can be seen from observations of previous periastra shown in Fig. 4.4 & 4.10. TeV emission may also have a two peak structure during the periastron passage, but more sensitive observations are required to confirm this (H. E. S. S. Collaboration et al. 2020). This is somewhat illustrated in the H.E.S.S. observations shown in Fig. 4.1.

The origin of the unpulsed radio, X-ray, GeV and TeV emission has been each attributed to radiation from relativistic electrons in previous modellings of the system. Relativistic electrons in the system originate from the pulsar winds and from particle accelerations caused by the shocks. The system of shocks created by the colliding winds accelerates the relativistic pulsar winds on one side and stellar outflow from the Be star on the other (see, Fig. 4.2). As described in Sect. 2.2, IC emission occurs due to the presence of relativistic electrons injected from the pulsar wind alone. With the presence of the shock, electrons travelling along the magnetic

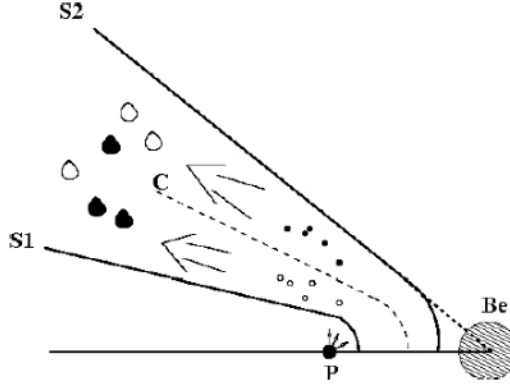


Figure 4.2: Sketch of the colliding winds and the stream of accelerated particles from the pulsar wind on one side and the stellar wind/circumstellar disc on the other. As seen in systems such as PSR B1259-63 (Credit: Chernyakova, M. INAM 2021).

field lines of the pulsar are redirected and accelerated by the shock. Non-relativistic particles from the Be star outflow are accelerated to relativistic speeds as a result of the shock on the adjacent side. While not travelling along the magnetic field lines, the relativistic electrons move through the magnetic field of the pulsar as they travel through the shock, resulting in synchrotron emission, as described in Sect. 2.1.

The unpulsed radio emission and enhanced X-ray emission is thought to be a result of synchrotron emission from accelerated electrons in the circumstellar disc and/or accelerated electrons from the pulsar winds (Ball et al. 1999). The observed TeV emission during the periastron is modelled as IC due to scatterings from the shocked pulsar winds and photons from the Be star (Kirk et al. 1999).

The GeV emission during the periastron passage have been of particular interest in the last decade due to the observations that have been made with the Fermi observatory. Since the beginning of the Fermi mission there have been four periastron passages that have been observed (2010, 2014, 2017, 2021). One could have assumed prior to these observations that the GeV emission would correlate with the X-ray and TeV peaks that have been observed during previous passages. However, in 2010, GeV flares were observed ~ 30 days after the periastron, which did not match flaring at other wavelengths. This flaring was found to repeat itself during the 2014 periastron, which seemed to confirm the repetitive nature of the GeV flares. Studies of the 2010 and 2014 periastra, such as Chernyakova et al. (2015), attributed the GeV flares to synchrotron emission. This would be similar to the Crab nebula where emission comes from the highest energy electrons accelerated at the maximal possible rate. However, when GeV flaring was observed once again in 2017, the peak flux was more than twice that of previous periastron peaks on a daily time scale; the flaring was delayed by ~ 10 days and began to return to pre-flare values around the same time as previous observations (> 70 days). Studies of the 2017 flaring period

by Tam et al. (2018) and Johnson et al. (2018) found variability during the short flares on the scale of 15 mins to 3 hours. The short 15 mins flares emit energy up 30 times greater than the spin-down luminosity of the pulsar, assuming isotropic emission.

The mechanics behind the periastron passage of PSR B1259-63 that leads to the 15 mins – 3 hrs GeV flaring, observed with the other broadband radiation emissions, cannot be explained with previous spectral studies. I present my analysis of the GeV flare in 2017 and the pre-flare of the 2011, 2014 and 2017 periastra, which was a part of a multiwavelength analysis with which we have developed a new model for the broadband emission of PSR B1259-63 during periastron that can account for the short and intense GeV flares (Chernyakova et al. 2020). We have also begun to apply this model to the most recent 2021 periastron with a preliminary analysis of a new multiwavelength observation campaign (Chernyakova et al. 2021). The details for when each of the periastra observed by Fermi-LAT occurred is shown in Table 4.1.

Table 4.1: Details on the time of each periastron and definitions of each GeV flare period (calculations based on Shannon et al. (2014)).

Date	Periastron t_P (MJD)	$t - t_P$ (Days)	Length of Flare (Days)
2010-12-14	55544.69	30	41
2014-05-04	56781.42	30	43
2017-09-22	58018.14	40	32
2021-02-09	59254.87	55	-

4.2 2017 Periastron Analysis

4.2.1 Modelling Fermi-LAT Data

The analysis of the Fermi-LAT data for the 2017 periastron was performed using Fermitools version 1.2.23 (released 11th February 2020). For the analysis of the 2017 periastron passage and the combined periastron data the analysis was carried out using the latest Pass 8 reprocessed data (P8R3) from the SOURCE event class. All gamma-ray photons used for this analysis were within the energy range 0.1 - 100 GeV and within a circular region of 15° around the region of interest (ROI) centred on PSR B1259-63 (see Fig. 4.3 for map of the region). The selected maximum zenith angle was 90° . The spatial-spectral model built in order to perform the likelihood analysis included the Galactic and isotropic diffuse emission components and the known gamma-ray sources within 20° of the ROI centre from the 4FGL catalogue

(Abdollahi et al. 2020). A likelihood analysis was applied twice to each observation data set to achieve the best model for that time span and energy range. For the first likelihood run, the normalization of every source within 15° of the ROI centre was left free, as was the spectral index of PSR B1259-63. The second run fixes the normalization of all sources outside 5° of the ROI centre to the value calculated from the first likelihood fit. The output model of this second likelihood analysis was then used for the lightcurve and spectrum generation. Normally this analysis would be done with a single likelihood run using a ROI $\sim 5^\circ$. However, I wanted to try this method of running the likelihood analysis twice to better refine the final model that would be used to build lightcurves and spectra.

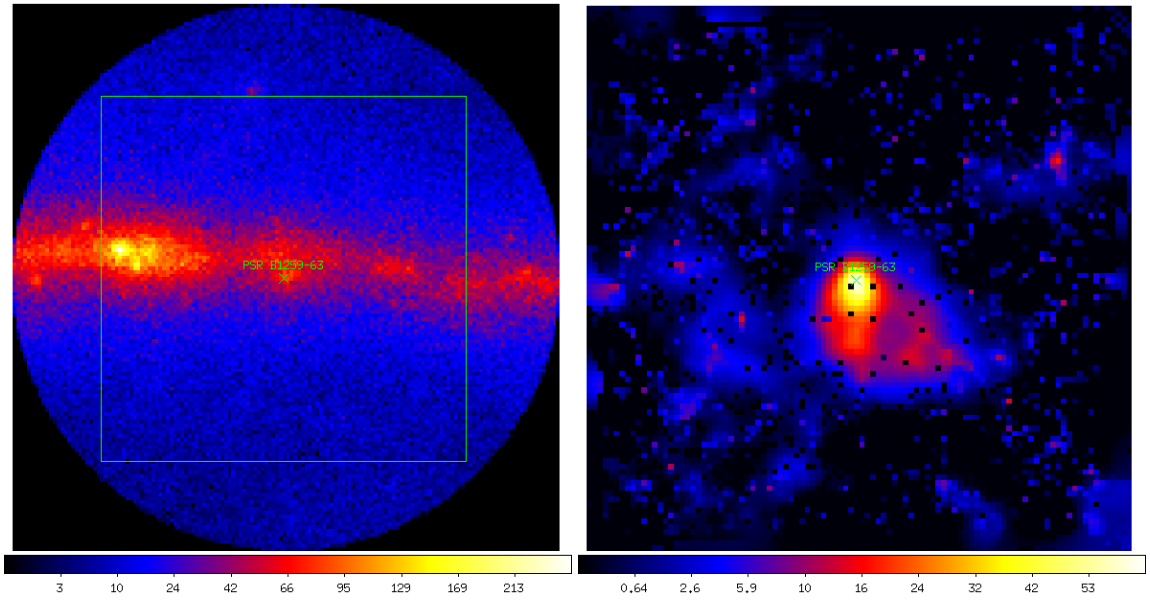


Figure 4.3: Maps of the region surrounding PSR B1259-63 using observational data from the 2017 periastron (57968 – 58118 MJD). Left: Binned counts map of the region where PSR B1259-63 is located with a 15° radius. Right: Test Significance map of the 20° region (see highlighted square in the left count map). This was calculated using a source model with all sources from the 4FGL catalogue within 20° of the location of PSR B1259-63.

The gamma-ray flux, light-curves and spectral results for PSR B1259-63 presented here were calculated using a binned likelihood fit using the BinnedAnalysis module from the FermiTools Python packages. PSR B1259-63 was modelled using a single powerlaw with the normalization left free and the index was fixed to the value from the preliminary analysis. Building lightcurves and spectra from Fermi data involves multiple likelihood runs on smaller binned sets of data to get the respective integrated flux for each time/energy bin. Such small selections of data means that the statistics are much lower, which is why the preliminary analysis on the total data selection to build the fitted source model is so important. When generating the light curves and spectra, any free sources (except PSR B1259-63) with a test significance

(TS) < 1 were removed from the fitted model, where $TS = \sigma^2$, i.e. 5σ confidence corresponds to $TS = 25$. If any bin had a poor detection of PSR B1259-63 ($TS < 1$ or $Flux < FluxError$) then the calculated flux was replaced with a 95% confidence upper limit on the photon flux above 100 MeV using the `IntegralUpperLimits` functions from `gtlike`. The spectral model output of the poor detection fit was used to calculate the upper limit values.

Table 4.2: Details of the time periods used for spectral analysis during the 2017 periastron. t_p = MJD 58018.1 corresponds to the time of 2017 periastron passage.

Data Set	Time period (MJD)	$t-t_p$ (days)
prfl1	55524.7 - 55544.7, 56761.4 - 56781.4, 57998.1 - 58018.1	-20 - 0
prfl2	55544.7 - 55564.7, 56781.4 - 56801.4, 58018.1 - 58038.1	0 - 20
avfl	58058.1 - 58090.1	40 - 72
pkfl	58059.1, 58074.1, 58076.1, 58088.1	41, 56, 58, 70

Data covering a time frame from 50 days before the periastron to 100 days after periastron were used to produce lightcurves of the 2017 periastron passage. This is a similar range of time with regard to the periastron that has been investigated in Chernyakova et al. (2014) and Chernyakova et al. (2015). The results of the lightcurve analysis were used to define the time periods for further spectral analysis. As seen in the top panel of Fig. 4.4, the weekly binned GeV light curves of the 2010, 2014 and 2017 periastra show differences in the shape of the post-periastron flaring period. The 2017 GeV light curve, with daily binning, is shown in Fig. 4.5. This light curve demonstrates strong day to day flux variability. The different colour highlights on this figure are used to show the data sets used for spectral analysis (see also Table 4.2). The results of this light curve analysis are in line with previous analyses of the 2017 periastron passage by Tam et al. (2018) and Johnson et al. (2018) where discrepancies are likely caused by the use of different catalogues and updated software.

For the spectral analysis we split the available data into several time periods (see Table 4.2). The period before the GeV flare (pre-flare), was divided into two: from 20 days before periastron, and from periastron until 20 days after (prfl1 and prfl2 data sets correspondingly). For these periods data from the 2010, 2014 and 2017 periastra were included to improve the statistics. For the flare analysis we use only data from the 2017 periastron to examine the spectra of the average flare period and the daily short flares that can be seen in the Fig. 4.5. The pre-flare spectra

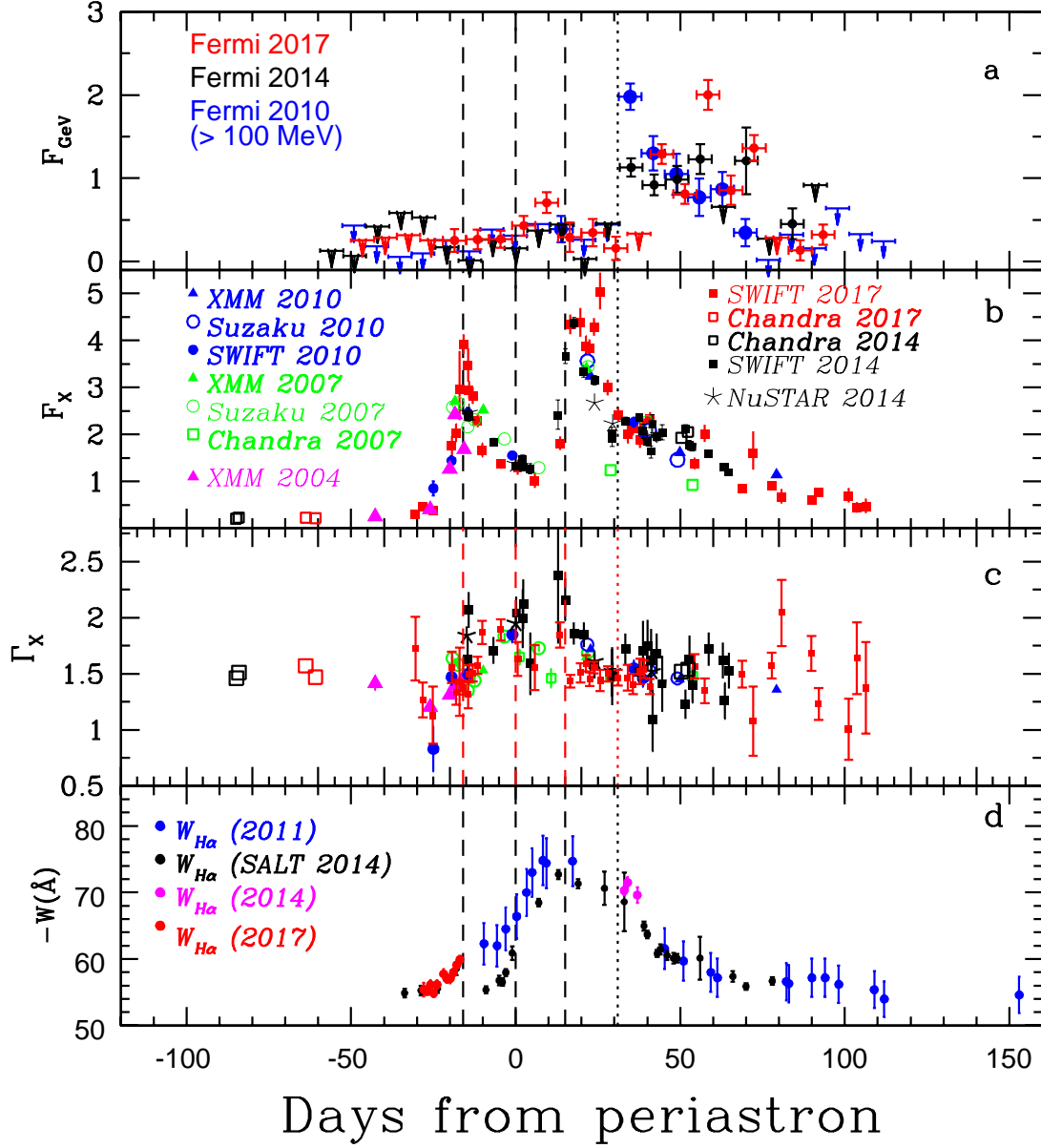


Figure 4.4: Evolution of multiwavelength PSR B1259-63 spectral characteristics over the different periastron passages. *Panel a:* Fermi-LAT flux measurements in the $E > 100$ MeV energy range with a weekly bin size. Flux is given in $10^{-6} \text{ cm}^{-2} \text{ s}^{-1}$. *Panel b:* 1-10 keV X-ray flux in units of $10^{-11} \text{ erg cm}^{-2} \text{ s}^{-1}$. *Panel c:* X-ray slope. *Panel d:* $H\alpha$ equivalent width.

before and after the periastron are compared in Fig. 4.8 and, along with the flare spectra, are also shown in Fig. 4.9. All time periods defined in Table 4.2 were also analysed in the 0.1 – 2.0 GeV energy range. We used a super exponential cut-off power law (PLSuperExpCutoff) model to match the shape of the GeV peak spectra, as this is a typical model for pulsars (Mirabal 2018); see Table 4.3 for the best-fit parameters. Spectral fitting was done twice, the first time with all the parameters free, and second time with γ_2 fixed to the value of the first fit to better constrain the other model parameters.

The spectral shape of the GeV emission turned out to be very different before and after the periastron, see Figure 4.8. Blue and red points correspond to the spectrum of the source averaged over 20 days before and after the periastron correspondingly. The spectrum before periastron (prfl1) is well described with a simple power law. The GeV emission after the periastron (prfl2) has a higher flux in the 0.1 – 2 GeV energy range and is characterised by a strong cut-off, see Table 4.3. This noticeable difference in spectral characteristics between different time periods of the preflare implies that around periastron there is a change of the spectrum of electron population responsible for the GeV production.

While there is a notable distinction in the characteristics between the time periods of the preflare, such a difference was not observed in the analysis of the flare periods. The spectra of both the average flare period (avfl) and the peaks of the flare (pkfl) are quite similar (see Figure 4.9 and Table 4.3), and differ mainly by the normalisation.

Further modelling of the spectra was conducted using the *naima* v.0.8.3 package (Zabalza 2015). *Naima* allows for computation of non-thermal radiation from relativistic particle populations, such as Bremsstrahlung, Synchrotron and IC. Initially, I modelled the flare and preflare data as a result of synchrotron and IC emission for the 2017 periastron using an electron spectrum with a exponential cutoff powerlaw. This is similar to spectral modelling of the system previously done in Chernyakova et al. (2015). The initial goal was to fit the spectral model in *naima* to the Fermi-LAT spectral data points to see if the spectral index corresponds to previous spectral studies. Fitting both the pre-flare and flare period of the periastron with this model, it was possible to acquire similar results for the spectral indices and magnetic field as previously acquired by Chernyakova et al. (2015). However, when modelling the spectrum of the short GeV flares, this modelling resulted in unrealistic values for the spectral parameters, such as indexes and magnetic field density. As the overall spectrum of the total GeV flare and the peak flares were found to be very similar, modelling of the high-energy spectrum required revision of the emission processes and the spectrum of the injected electrons.

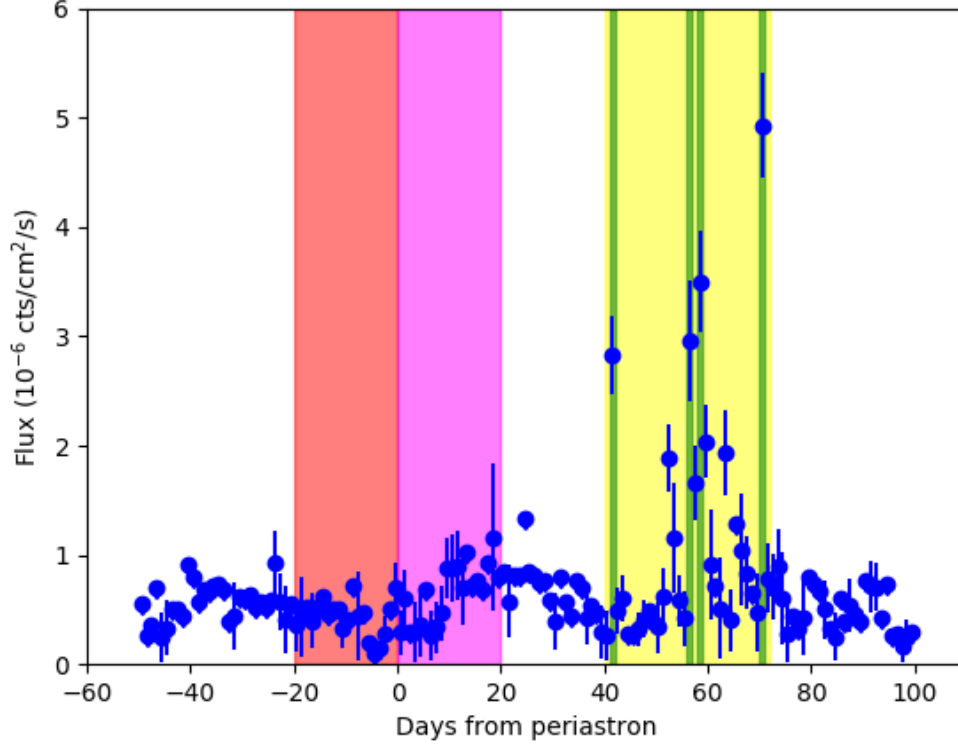


Figure 4.5: Daily-binned light curve of the 2017 periastron passage. The highlights indicate the time periods that were used for spectral analysis and modelling; the details are given in Table 4.2. The different periods are shown as: prfl1 = Red, prfl2 = Magenta, avfl = Yellow, pkfl = Green.

Table 4.3: Spectral model parameters from the binned likelihood analysis of different phases of the 2017 periastron from 0.1 - 2.0 GeV. The model used is the PLSuperExpCutoff where $dN/dE = N_0(E/E_c)^{\gamma_1} \exp(-(E/E_0)^{\gamma_2})$.

Data Set	γ_1	E_c (GeV)	γ_2	Photon Flux (10^{-6} cts/cm ² /s)
prfl1	-2.9 ± 0.3	—	—	0.26 ± 0.05
prfl2	-1.5 ± 0.4	0.50 ± 0.08	3.0	0.28 ± 0.04
avprfl	-2.4 ± 0.3	0.65 ± 0.10	5.0	0.34 ± 0.05
avfl	-2.4 ± 0.1	1.53 ± 0.23	3.0	1.11 ± 0.09
pkfl	-2.3 ± 0.1	1.86 ± 0.43	3.0	3.39 ± 0.38

4.2.2 Discussion of 2017 Modelling

As previously mentioned, gamma-ray binaries are known to be highly efficient systems and PSR B1259-63 is no exception. In the 2010 and 2014 periastrons the energy released during the GeV flare reached as high as 68% of the spin-down luminosity (Caliandro et al. 2015). By comparison, the GeV flare observed in 2017 began approximately 10 days later than previous flaring periods and consisted of shorter more intense flares on a daily scale, as seen in Fig. 4.5. Within these short flares there was a structure of sub-flares. Initially the flares were found on a scale of 3 hrs (Tam et al. 2018), but they were found to be as short as 15 minutes with power exceeding the spin-down luminosity by a factor of up to 30 (Johnson et al. 2018). This is only possible if the GeV flare is produced as a separate and highly isotropic component (Chernyakova et al. 2020).

Based on the analysis and modelling of the GeV flare of 2017 along with optical observations from the South African Astronomical Observatory (SAAO) 1.9 m telescope and X-ray observations from Swift X-ray Telescope (XRT), as seen in Fig. 4.4, our team presents a new model as published in Chernyakova et al. (2020). In this model, relativistic electrons are released isotropically from the pulsar. These electrons are unshocked and approximately monoenergetic. A portion of these electrons interact with the shock and are accelerated strongly near the apex of the shock or weakly in other regions of the shock. As a result, the shock effectively creates an “emission cone” where there are two distinct populations of electrons: (1) electrons of the unshocked and weakly shocked pulsar wind and (2) strongly shocked electrons. The geometry of this model is illustrated in Fig. 4.6, where the different electron populations are also highlighted.

The spectrum of unshocked electrons was selected to be a power law with the slope -2 in energy range $E_e = 0.6 - 1$ GeV. A small fraction of electrons are additionally accelerated at the strong shock near the apex to $E_e \sim 500$ TeV energies with the similar slope $\Gamma_e = -2$ on a characteristic timescale:

$$t_{\text{acc}} \approx 0.1 (E_e/1 \text{ TeV}) \eta (B_0/1 \text{ G})^{-1} \text{ s} \quad (4.1)$$

where B_0 is a magnetic field in the region and $\eta \geq 1$ is the acceleration efficiency (Khangulyan et al. 2008).

The rest of the electrons flying into the shock direction will be reverted to flow along the shock at the surface of stellar-pulsar wind interaction cone far from the apex, and could be additionally mildly accelerated on a weak shock, see the cyan region in Fig. 4.6. This leads to a power law tail in the spectrum of diverted electrons with a slope ~ -3 which continues above 1 GeV to at least $E_e \sim 5$ GeV. This slope is characteristic of particle acceleration on weak shocks (Bell 1978; Blandford &

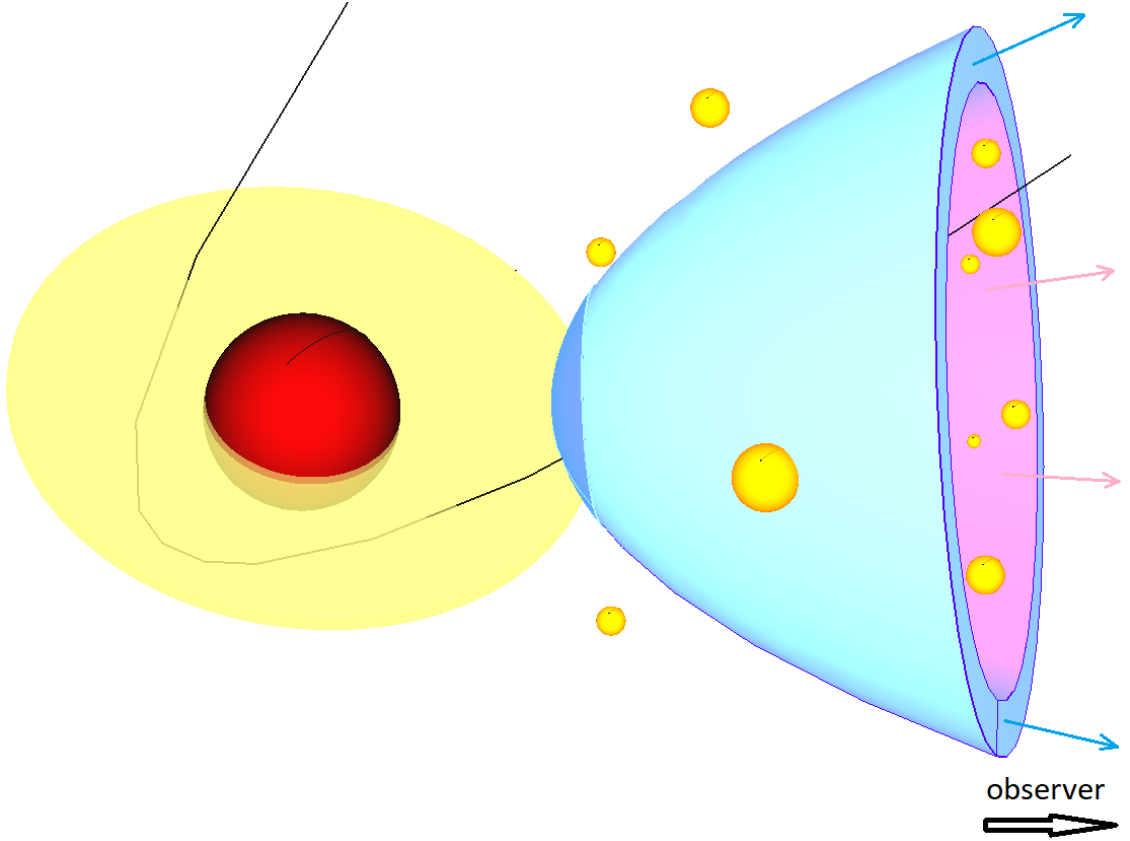


Figure 4.6: A sketch of the geometry of the proposed model (not to the scale) for the period of GeV flare (Chernyakova et al. 2020). Red sphere presents the Be star with the disc shown with yellow semi-transparent circle. Stellar/pulsar winds interaction cone is shown with cyan. PSR B1259-63 pulsar orbit is illustrated with black line. The unshocked pulsar electrons (magenta) are strongly accelerated in the region close to the cone’s tip (blue region; “strongly shocked electrons”) and weakly accelerated at the rest of the cone surface (cyan region; “weakly shocked electrons”). The flight directions of these electrons are shown with cyan/magenta arrows. The clumps of stellar wind are shown with yellow spheres.

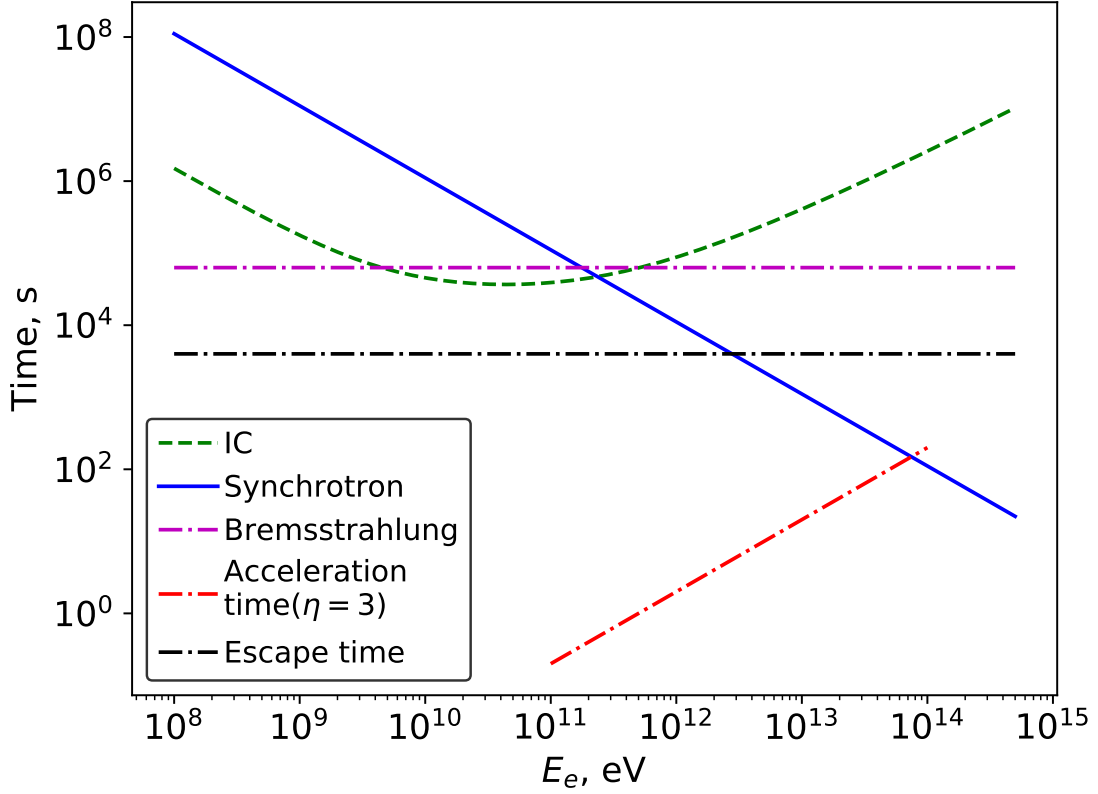


Figure 4.7: Comparison of the cooling times to acceleration and escape time for various radiation processes in the case of avfl model, see text for details.

Eichler 1987). Hereafter we will refer to these diverted electrons as weakly shocked electrons.

The spectra of both populations will be additionally modified by radiative (IC, synchrotron, bremsstrahlung), as described in Ch. 2, and non-radiative (adiabatic or escape) losses operating in the system. The comparison for the cooling times during the average flare period is shown in Fig. 4.7. This plot is based on calculation for the cooling times as described in Ch. 2. In this case, for electrons at TeV energies, which is the case for the strongly shocked electrons, the synchrotron cooling time is much lower than the escape time. Thus the shocked electrons spectrum will be significantly modified by these cooling losses. In our calculations the resulting electron spectrum was determined by numerically calculating the radiative losses of a continuously injected spectrum of electrons, until a steady solution has been obtained. The time that electrons spend in the emitting region, R/c , is about a few thousand seconds, and is long enough to substantially modify the injected spectrum due to synchrotron losses (in our calculations we took $t_{esc}=4000$ s, see Table 4.4).

It should be noted that the losses substantially modify the injected spectrum and thus properly accounting for such losses is important for modelling the PSR B1259-63 system. Additionally one has to account for the radiation efficiency of

the considered mechanisms. This is rather low for the majority of the considered processes and subsequently an increase of the total energy of the pulsar wind is required (in comparison to 100% efficiency case).

The synchrotron, bremsstrahlung and IC emission was calculated with the *naima* v.0.8.3 package (Zabalza 2015), which uses the approximations for the IC, synchrotron and bremsstrahlung emission from Aharonian & Atoyan (1981); Aharonian et al. (2010); Khangulyan et al. (2014); Baring et al. (1999).

According to our model, similar to previous works (Chernyakova et al. 2014, 2015; Chen et al. 2019), the X-ray and TeV components are explained as synchrotron and IC emission of the strongly shocked electrons. The GeV component in our model is a separate component due to the combination of the IC and bremsstrahlung emission of the less energetic, unshocked electrons interacting with the clumps of the matter from the Be-star wind/disc which penetrated through the shock. The study of the 2011 periastron by Abdo et al. (2011) had proposed bremsstrahlung due to dense clumps as a possible explanation for the observed GeV emission. However, under a 1-zone model, a counterpart to the GeV flare would be expected in the X-ray emission. As no X-ray counterpart was or has been observed, the GeV flares were modelled as enhanced synchrotron emission of the shocked electrons (Chernyakova et al. 2015). With our 2-zone model, bremsstrahlung becomes necessary to explain the 15 mins – 3 hrs flares observed and the lack of counterpart to the GeV flares is due to the separate emission zones.

The modelled spectral energy distributions (SEDs) along with the observed keV – TeV data are shown in Fig. 4.9. In this figure the synchrotron and IC emission of the strongly shocked electrons are shown with solid and dashed magenta curves correspondingly. The contributions of IC and bremsstrahlung emission of the unshocked and weakly shocked electrons are indicated with dashed and dashed-dot curves correspondingly, where the colours refer to the prf1 (blue) and prf2 (red) periods. The TeV points shown are taken from Aharonian, F. et al. (2005), and the coloured region at TeV energies represent the range of multi-years H.E.S.S. measurements reported in Fig. 2 of H. E. S. S. Collaboration et al. (2020). The shaded region at X-ray energies represents the range of fluxes observed by Swift in 2017 before (left panel), and after (right panel) the GeV flare.

To explain the observed luminosity one has to consider that for relativistic electrons both IC and bremsstrahlung radiation is strongly peaked in the forward direction and most of the energy radiated as a photon moving in the same direction as the initial electron. Now consider the direction of motion for electrons originating from an isotropic pulsar wind. A small number electrons travel to the apex of the shock, resulting the X-ray and TeV emission. All remaining electrons are either unshocked and travelling in the direction of observer or are weakly redirected by the

shock, once again in the direction of the observer (indicated in Fig. 4.6). The observed excess of energy in the GeV flares is therefore explained by the high fraction of unshocked/weakly shocked electrons moving in the direction of the observer and mostly radiating in the same direction.

The difference in true anomaly between days 40 and 80 after the periastron (period including all short flares) is about 20° . This angle is comfortably smaller than the apex angle of the shock $4\pi/30$ needed to explain the observed luminosity during the short flares in the case of 100% efficiency. This apex angle of the shock is simply defined as the total solid angle (4π) over the observed luminosity in units of the spin-sown luminosity (30 for the 15 mins flares). This is assuming an isotropic distribution of the initial pulsar wind and 100% efficiency. The cone of such a size is a result of the interaction of the isotropic pulsar wind with the isotropic Be star wind if the winds ram pressure ratio is $\frac{L_{sd}}{\dot{M}V_{wc}} = 0.05$ (Khangulyan et al. 2011).

In Fig. 4.9 we show Fermi-LAT spectra averaged over the total flare (green points), and over the peak of the flares only (red points). These spectra can be explained as a combination of IC and bremsstrahlung emission on the clumps with densities of $\sim 2 \times 10^{10} \text{ cm}^{-3}$ and $< 1 \times 10^9 \text{ cm}^{-3}$ correspondingly, see Table 4.4. Please note that in the Fig. 4.9 we show only the dominant component (IC for the average flare and bremsstrahlung for the peaks) in order to make the figure more readable. Also please note that the split of the IC and bremsstrahlung is very model dependent and requires detailed hydrodynamic simulations beyond the scope of this analysis. To explain the observed luminosity of the 15 minutes long flare one needs to assume a 1000 s long interaction with a clump of material with a density of $4 \times 10^{11} \text{ cm}^{-3}$.

The required densities of the clumps are higher than the average density of an undisturbed disc. At the same time the required average density both around the periastron and during the period of GeV flare is consistent with the unperturbed, smoothly decreasing disc density model in van Soelen et al. (2012), which gives a density at the base of disc of $n_e \approx 6 \times 10^{13} \text{ cm}^{-3}$. At the binary separation distance at 40 days from periastron the disc density will have decreased to $\sim 10^8 \text{ cm}^{-3}$ (within the disc). This, combined with the observed $H\alpha$ variation (Fig. 4.4), clearly indicates that the disc must be strongly clumped and disrupted near periastron. The difference in the 2017 Fermi-LAT light curve (rapid flares) from the 2010 and 2014 periastra, also suggests a more complicated disc behaviour, that was unfortunately not observable during the 2017 periastron (Fujita et al. 2020).

Recently a very hard TeV spectrum with the slope reaching values of $\Gamma \sim 2.5$ at certain orbital phases was reported in H. E. S. S. Collaboration et al. (2020), see shaded region in Fig. 4.9. Assuming that this emission is produced by IC in a strong Klein-Nishina regime the spectral slope of the corresponding electrons can be

Table 4.4: Details of the models. D is a distance from the Be star to the emission region (Chernyakova et al. 2020). Effective luminosity L of the pulsar wind electrons (without considering beaming effects) is measured in units of spin-down luminosity $L_{sd} = 8.2 \times 10^{35}$ erg/s.

Data Period	$t-t_p$, days	D, 10^{13} cm	n_{clump} , 10^{10} cm $^{-3}$	B, G	Γ_2	L/ L_{sd}
fl15		7.5	40	0.1	3	30
pkfl	41,56,58,70	7.5	2	0.1	3	30
avfl	40 – 72	7.5	0.1	0.1	3	30
prfl2	0 – 20	2.5	0.1	0.4	2.5	1
prfl1	-20 – 0	2.5	0.1	0.4	3	1

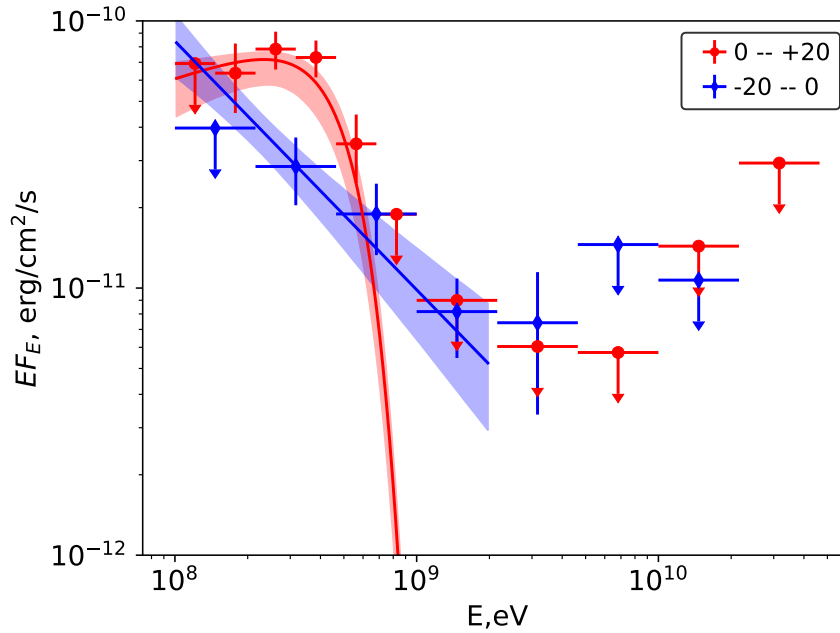


Figure 4.8: GeV emission of PSR B1259-63 during the periods twenty days before (blue points, prfl1) and after (red points, prfl2) the periastron. Blue and red curves show best fit models in 100 MeV – 2 GeV energy range, see Table 4.3. Shaded regions show 1σ confidence range for fitted models.

estimated to be $\Gamma_e \sim 2.5$, similar to the value used in the modelling presented here.

In the case that the electrons propagate through regions with a non-zero magnetic field their spectrum, at TeV energies, undergoes severe cooling due to synchrotron losses (see Fig. 4.7). This leads to the formation of a break in the electron spectrum with a typical softening after the break of $\Delta\Gamma_e = 1$. Thus, to match the observed H.E.S.S. spectrum, an initially extremely hard spectrum of electrons with a slope $\Gamma_{e,0} = 1.5$ with a break to $\Gamma_e = 2.5$ at TeV energies has to be considered.

The initial slope $\Gamma_{e,0} = 1.5$ corresponds in the proposed model to the spectrum of

the shocked electrons. This slope is substantially different from a “standard” $\Gamma_e = 2$ slope of Fermi-mechanism accelerated electrons. We would like to note, however, that very hard slopes up to $\Gamma \sim 1$ (at least at relatively broad energy range close to the spectral cut-off) were reported for diffusive shock acceleration on multiple shocks, see e.g. Melrose & Pope (1993); Bykov et al. (2013); Vieu et al. (2020). Such shocks can potentially form in PSR B1259-63 in a pulsar wind/Be star disc interaction region, assuming that the disc hosts multiple clumps.

GeV emission around the periastron period can be explained as IC emission of the unshocked electrons, see Figure 4.9. In this Figure we also show NuSTAR data points taken around 2014 periastron (Chernyakova et al. 2015). Within our model, softening of the X-ray slope around the periastron can be attributed to additional cooling losses due to the higher value of magnetic field and the increased photon energy density near the periastron. To explain higher intensity and much sharper cutoff of the GeV flux after the periastron, one needs to assume that the acceleration becomes more efficient and the slope of the electrons is equal to -2.5 above 1 GeV. The parameters of all the models are summarised in Table 4.4.

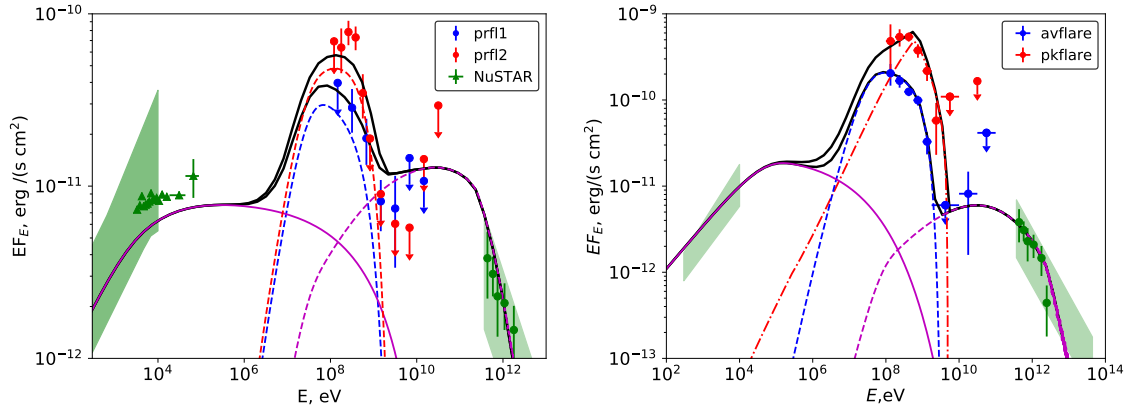


Figure 4.9: *Left:* Broad band spectrum emission of PSR B1259-63 during the 20 days before (blue points) and after (red points) the periastron period. Green X-ray points are NuSTAR observations of the 2014 periastron from (Chernyakova et al. 2015) *Right:* Broad band spectrum emission of PSR B1259-63 during the GeV flare. Blue points represent the flare averaged over the whole duration, and red points correspond to the sum of peak periods.

The TeV points shown are taken from Aharonian, F. et al. (2005), and the shaded regions at TeV energies represent the range of multi-years H.E.S.S. measurements reported in Fig. 2 of H. E. S. S. Collaboration et al. (2020). The shaded regions at X-ray energies represent the range of fluxes observed by SWIFT in 2017 before (left panel), and after (right panel) the GeV flare. In both panels dashed lines show an IC component, solid magenta line corresponds to synchrotron emission of strongly shocked electrons, dash-dotted line shows the bremsstrahlung component and black solid line corresponds to overall model emission.

4.2.3 Summary and Conclusions

The multiwavelength modelling of the 2017 periastron passage of PSR B1259-63 has provided a new understanding as to the origins of the transient GeV flares observed. The results of the multiwavelength analysis have been published as Chernyakova et al. (2020). This 2-zone model of bremsstrahlung, synchrotron and IC emission from both the shocked and unshocked electrons within the emission cone may be applicable to other gamma-ray binaries featuring a Be star and pulsar. As with previous studies, the X-ray and TeV emission at periastron was attributed to synchrotron and IC of the shocked pulsar winds respectively. Meanwhile the GeV flares were modelled with bremsstrahlung and IC emission from the unshocked pulsar winds interacting with clumps from the Be circumstellar disc penetrating the shock. The difference in the GeV flare intensity compared to previous periastra observed could be a result of denser clumps penetrating the shock. Our 2-zone modelling and the addition of bremsstrahlung emission will be important to consider modelling the high-energy spectrum of Be-pulsar gamma-ray binaries. The 2021 periastron provided an opportunity to apply our new model to the system once again.

4.3 2021 Periastron Observations

As of writing, the most recent periastron of PSR B1259-63 occurred on 2021-02-09 (MJD 59254.87). As shown in Fig. 4.10, a multi-wavelength observation campaign was organised to test our model proposed based on the analysis of the 2017 periastron. Optical observations were conducted with the South African Large Telescope (SALT), X-ray observations were conducted using Swift/XRT and the NICER instrument, and GeV data was collected from Fermi-LAT.

During this campaign, I participated in the observations of PSR B1259-63 with the Australian Telescope Compact Array (ATCA) to obtain a radio light curve spanning the periastron from 2021-02-19 to 2021-05-13 (83 days). The ATCA is a radio interferometer with six 22 m antennas providing a maximum baseline of 6 km, located in Narrabri, NSW, Australia. The observations of PSR B1259-63 were conducted in the 4-cm band using the Compact Array Broadband Backend (CABB) with centre frequencies of 5.5 GHz and 9 GHz, each with 2 GHz of bandwidth and 1 MHz frequency channels (Wilson et al. 2011).

We conducted observations of PSR B1259-63 for 3 hour windows every 2 days, as allowed by the telescope schedule. The primary calibrator for ATCA, B1934-638, was observed for 10 mins at the start of each observation. A secondary calibrator, J1322-5632, was also observed for 2 mins for every 20 mins on PSR B1259-63. As part of the preliminary analysis of the radio observations, the 5.5 GHz continuum

data was examined with plans to later perform a full spectral analysis of both the 5.5 GHz and 9 GHz frequencies.

4.3.1 Discussion of 2021 Preliminary Results

The 2017 periastron was marked by quite an unusual GeV flare compared to the 2010 and 2014 periastron. Once again, the 2021 periastron shows very unusual behaviour from the GeV flare but also from the X-ray observations. X-ray data shows the expected peaks during the disc crossings, although these peaks are noticeably lower than previous observations. However, we also observed a third peak in the X-ray data that began approximately 30 days after periastron. This timescale in previous years would correlate with the GeV flare, however the GeV flare did not begin in 2021 until ~ 55 days after periastron. This third peak has no clear counterpart at any other observed wavelength.

During the second X-ray peak there was a strong correlation observed between radio and X-ray data. However, this correlation fell away during the third X-ray peak. This has been further illustrated in the X-ray panel of Fig. 4.10 where the dashed line is the re-scaled radio data from the radio panel. The 2021 radio data seems to be in line with previous 4.8 GHz observations from 1997, 2000 and 2004.

The GeV flare was marked by a noticeable delay beginning at ~ 55 days after periastron, approximately 15 days later than the 2017 periastron. During the pre-flare period around the periastron, average flux seems consistent with values measured in 2011-2017. During the flare period of 55–108 days after periastron, weekly timescale values were comparable to the 2014 periastron, although peaks were more comparable to the 2011 and 2017 periastra. After this period a gradual decay has been observed in the GeV band.

Based on our proposed model described in the previous section and Chernyakova et al. (2020), we suggest that the abnormal emission at X-ray and GeV observed is generated by an "emission cone" formed by the interaction of the pulsar/Be star outflow.

The lower X-ray peaks during the disc crossing, along with the slightly lower $H\alpha$ equivalent width observed, may indicate that the density of the Be star's circumstellar disc is lower than previous periastra. This would cause the shock to occur further from the pulsar and would result in a weaker magnetic field within the region. A lower density disc, along with a likely lower polar outflow, would also result in a much larger opening angle of the emission cone than observed previously. The third X-ray peak could be the result of a large number of clumps above or below the disc. Such clumps could modify the flow of the strongly shocked relativistic electrons on the surface of the emission cone. This would effectively increase their escape time

from the system and lead to enhanced X-ray emissions. As previously described, GeV emission in our model is caused by unshocked electrons of the pulsar wind. These electrons propagate within the emission cone and thus would not be significantly affected by clumps interacting with the flow of strongly shocked electron on the surface of the cone.

On daily timescales, the GeV flare observed in 2021 had a peak flux of $\sim 5 \times 10^{-6}$ ph/cm²/s which is comparable to the 2017 periastron flare. This is based on GeV lightcurves shown in Fig. 4.11 which were developed as part of the preliminary analysis of the periastron data. There was also a number of shorter outbursts observed on a timescale of 5 mins to 3 hrs, similar again to 2017 where 15 mins flares observed at up to 30 times the spin-down luminosity. The peak of the short outbursts, as seen in the right panel of Fig. 4.11 has a flux of $\sim 18 \times 10^{-6}$ ph/cm²/s. This would require luminosity of 4.6×10^{36} erg/s which exceeds the spin-down luminosity of 8.2×10^{35} erg/s by a factor of 5–6. As our model proposed by the 2017 periastron analysis accounted for the aforementioned luminosity that exceeded the spin-down luminosity by a factor of 30, we therefore argue the observed short timescale variability in 2021 is consistent with our model with a larger opening angle of the emission cone.

4.3.2 Summary & Conclusions

Based on our preliminary analysis of the 2021 periastron of PSR B1259-63, the 2-zone model for the system can account for the unique behaviours observed in X-ray and GeV. Unlike previously observed periastra, there was a third peak observed in X-ray with no radio counterpart and the GeV flare period was delayed with lower peak luminosity than 2017. These characteristics can be explained by a lower density in the Be star disc during periastron compared to 2017. This results in a wider apex angle of the emission cone and less enhancement of the GeV flares. Clumps interfering with the surface of the shock could increase the escape time of electrons in the system, leading to a longer period of enhanced X-ray emission. These preliminary results and discussions have been published as Chernyakova et al. (2021). A more detailed analysis of the multi-wavelength data from this passage is in progress for later publication.

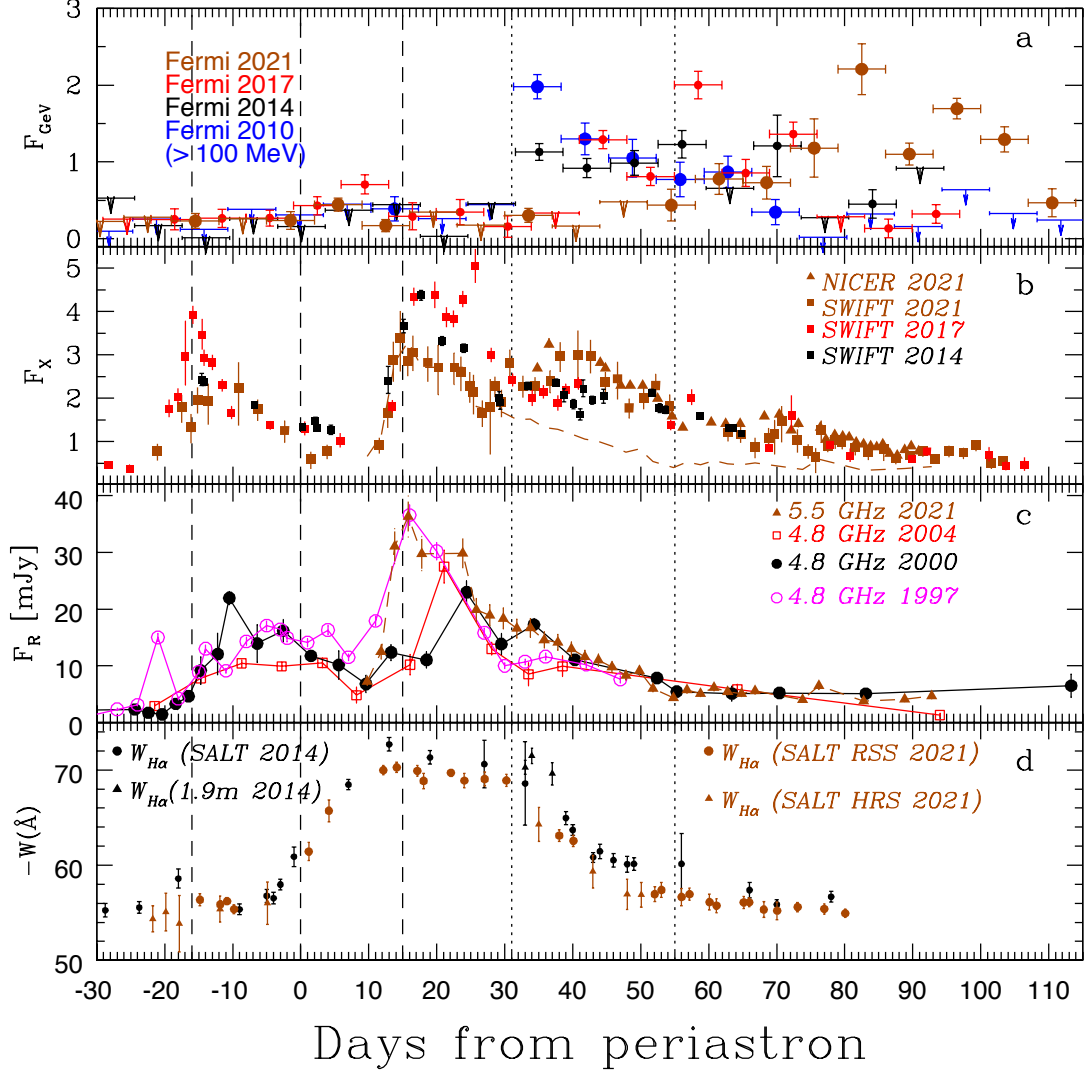


Figure 4.10: Evolution of PSR B1259-63 flux over the different periastron passages (Chernyakova et al. 2021). Dashed lines correspond to the periastron and to the moments of disappearance (first non-detection) and reappearance (first detection) of the pulsed emission, as observed in 2010 (Abdo et al. 2011). Dotted lines correspond to the first appearance of the detection in GeV band at a day time scale in 2010 and 2021. *Panel a:* flux measurements in the $E > 100$ MeV energy range with a weekly bin size. Flux is given in $10^{-6} \text{ cm}^{-2} \text{ s}^{-1}$. *Panel b:* absorbed 1-10 keV X-ray flux in units of $10^{-11} \text{ erg cm}^{-2} \text{ s}^{-1}$. Scaled 5.5-GHz radio data from 2021 are also shown in this panel with a gold dashed line for comparison. *Panel c:* radio flux densities in mJy. *Panel d:* $H\alpha$ equivalent width.

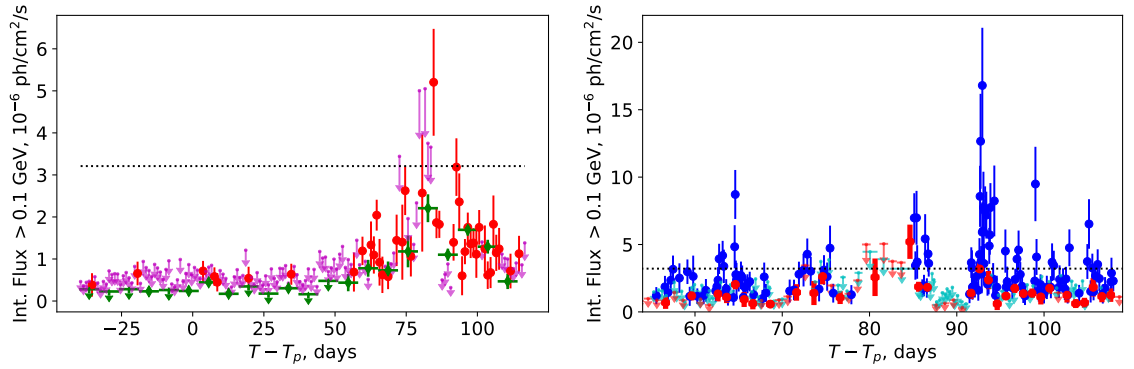


Figure 4.11: Left: Fermi-LAT weekly (green points) and daily (magenta upper limits and red points – detection's with $TS > 4$) light curves of PSR B1259-63 at energies 0.1–10 GeV. The dotted line present the flux corresponding to spin-down luminosity of PSR B1259-63 ($L_{sd} = 8.2 \cdot 10^{35}$ erg/s). Right: Blue points: Fermi-LAT light curve at > 0.1 GeV range for the period MJD 59310–59363 ((+55; +108) days after the periastron) with adaptive time binning (to have 9 photons per time bin in 1° radius circle around PSR B1259-63 position at 0.1 – 10 GeV). The light curve covers the period of the highest flux of the source in the GeV band. Red points correspond to a daily lightcurve, same as in the left panel (Chernyakova et al. 2021).

Chapter 5

Athena XIFU Simulations of Vela X-1

As the name suggest, HMXBs have been extensively studied at X-ray energies since their discovery. Since 1999, the orbital X-ray observatories, XMM-Newton and the Chandra X-ray Observatory, have been used for extensive spectral studies of known and newly discovered HMXBs. However, the limitations of the resolution and sensitivities of these telescopes are starting to be reached in the study of such systems. Observations of HMXBs require observations of tens of kiloseconds to resolve the spectrum at the level of $1 - 100$ mCrab which limits our current ability to study spectral variability on shorter timescales. Characteristics of these systems, such as emission line details and accretion geometry, are difficult to resolve from observations alone, due to these limitations. Studies can require extensive Monte Carlo simulations or hydrodynamic simulations to compare with observations in order to come to conclusions.

Vela X-1 is a widely known and well-studied wind-fed HMXB and commonly used as a reference source to test the effectiveness of planned X-ray instruments, e.g. Hitomi telescope (Kitamoto et al. 2014). As an eclipsing HMXB, the system is highly transient with drastic changes in the spectra and observed flux on a daily timescale and flaring observed on timescales of several ks. In this chapter I will present simulations conducted for the Athena X-IFU to test the effectiveness of observing such a variable source on timescales as short as several ks which would allow for study of discrete changes in the X-ray spectra, such as change in emission line profiles. To elaborate on these findings, I will also present simulated observations of photoionization regions, modelled with XSTAR, to test whether X-IFU will be capable of detecting the fine change in the shape of emission line profiles over the course of an eclipse and whether the geometry of the system may be obtainable via eclipse mapping with X-IFU observations.

Preliminary results simulating X-IFU observations of Vela X-1 were presented at

the 9th X-IFU Consortium Meeting on the 15th April 2019 and the Irish National Astronomers Meeting (INAM) on the 4th September 2019.

5.1 Vela X-1

Vela X-1 is considered to be the archetype HMXB consisting of a wind-accreting neutron star orbiting a massive companion star. It is a binary system where the neutron star is an X-ray pulsar with a pulse period of 283 s (McClintock et al. 1976) and the massive companion is a B-type supergiant HD 77581 (Hiltner et al. 1972), which powers the stellar wind with a mass-loss rate of approximately $(1 - 7) \times 10^{-6} M_{\odot} \text{yr}^{-1}$. The pulsar orbits the companion star with an orbital period of 8.964 days (Forman et al. 1973) in a low eccentricity orbit of $e \sim 0.09$ (Bildsten et al. 1997). Due to the highly inclined orbital plane of the system ($i > 79^{\circ}$), the pulsar is eclipsed by the massive companion from orbital phase $\phi \sim 0.9 - 0.1$ (Giménez-García et al. 2016). The X-ray luminosity averages at a scale of $\sim 10^{36}$ erg/s, which is expected from X-ray emission caused by accretion of the stellar wind driven by the gravitational field of a neutron star (Watanabe et al. 2006). Vela X-1 has an average X-ray flux of ~ 250 mCrab but has been observed with fluxes as high as 3.0 Crab as a result of flaring at 20-60 keV (Fürst et al. 2010).

The companion star has a radius of $30 R_{\odot}$ (R_{\odot} = solar radius) and has an orbital separation of $\sim 53 R_{\odot}$ (Quaintrell et al. 2003), thus the pulsar is constantly interacting with stellar wind outflow from the companion. The system is powered by this stellar wind-fed accretion as previously described in Sect. 1.1.2. The resulting accretion flow from the companion to the pulsar has a complex geometry, consisting of an accretion wake (Malacaria et al. 2016) and a photoionization wake (van Loon et al. 2001; Amato et al. 2021). As the line of sight of the observer passes through different regions, depending on the orbital phase, there is a observed change in absorption over the whole period. For example, observations at orbital phase $\phi \sim 0.50$ (inferior conjunction) observe an increase in the column density by an order of magnitude compared to observations at $\phi = 0.25$ (Watanabe et al. 2006; Doroshenko et al. 2013). The phases referenced are illustrated in Fig. 5.1.

The photoionized stellar wind surrounding the Vela X-1 pulsar has an abundance of emission lines that were modelled using an extensive analysis with Chandra by Watanabe et al. (2006). This analysis used three observations of Vela X-1 from the Chandra HETGS/ACIS-S that covers three different orbital phases of the system from February 2001 (Table 5.1). The variation in the spectrum continuum and emission lines intensity across the three orbital phases were used alongside a Monte Carlo-based simulation of 3D radiative transfer to simulate the X-ray photon interactions with the stellar winds. The results of this analysis provided an idea of the

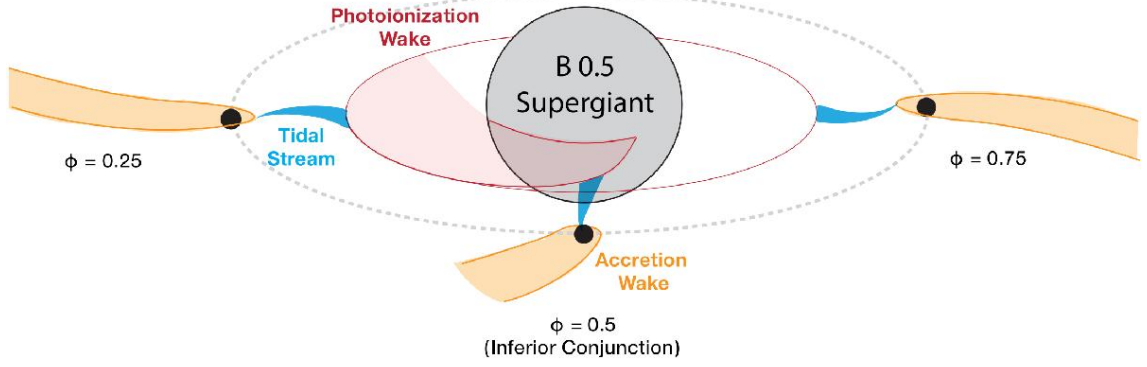


Figure 5.1: Sketch of the Vela X-1 showing the photoionization and accretion wake over three orbital phases (Malacaria et al. 2016). The position of the observer is such that the pulsar lies between the observer and the supergiant at $\phi = 0.5$ and the supergiant eclipses the pulsar and wakes at $\phi = 0.0$.

geometry of the photoionization region and the nature of the stellar wind accretion which continues to be studied (Grinberg et al. 2017).

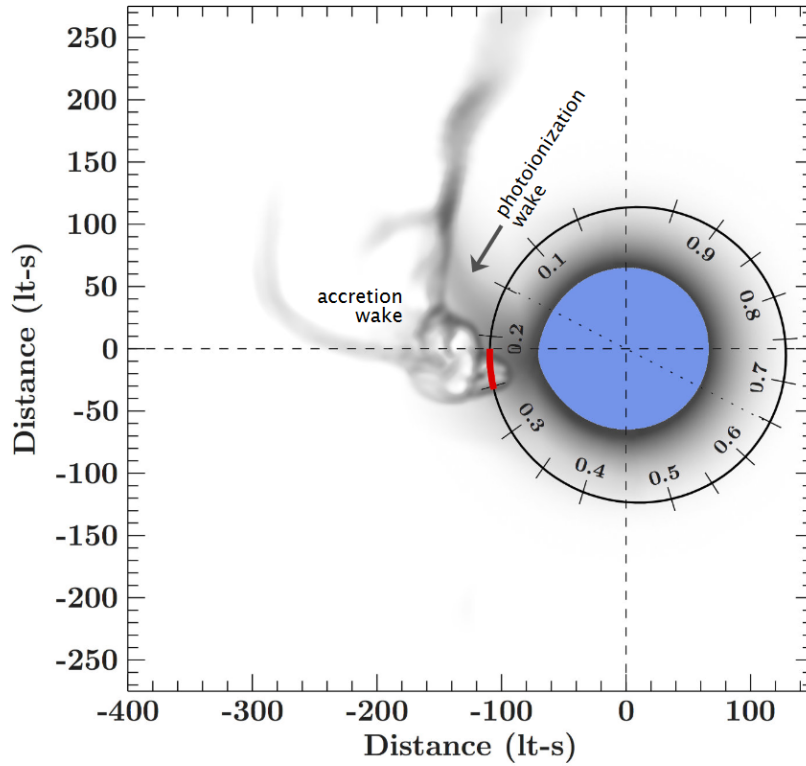


Figure 5.2: To-scale diagram of Vela X-1 (Grinberg et al. 2017) based on hydrodynamical simulations of the system by Manousakis (2011).

Since Vela X-1 is such a well studied system, it is an excellent candidate for testing the capabilities and effectiveness of future X-ray astronomy missions. The spectrum models for the different orbital phases were already used for simulations of Hitomi during the development phase (Kitamoto et al. 2014). Currently the Athena

X-ray telescope is under development, and Vela X-1 is an excellent source to use for simulations of the X-IFU observations. This is because of the fine emission line details and multiple emission regions that vary over the course of the orbit in the system. Testing the sensitivity X-IFU with regard to these features, especially for observations < 10 s ks, could present new opportunities to study the morphology of HMXBs with high phase resolution observations. It could also provide a way to investigate the spectrum of flaring in such systems, as has been observed in Vela X-1 on timescales of 2 ks by Odaka et al. (2013).

Table 5.1: Log of Chandra observations used by Watanabe et al. (2006) for modelling the line emissions of Vela X-1 at three orbital phases. Phases are defined such that inferior conjunction occurs at orbital phase 0.50 and superior conjunction (eclipse) occurs at phase 0.00.

Date	Orbital Phase	Phase Range	Exposure (s)
2001-02-11	0.00	0.980 - 0.093	83150
2001-02-05	0.25	0.237 - 0.278	29570
2001-02-07	0.50	0.481 - 0.522	29430

5.2 X-IFU Simulations of Vela X-1

To demonstrate the capabilities of X-IFU in the study of HMXBs, I present simulated observations of Vela X-1 using the Simulation of X-ray Telescopes (SIXTE, version 2.6.0) software package (Dauser et al. 2019). The models used for Vela X-1 were taken from the Chandra analysis by Watanabe et al. (2006) and the model was simulated using Simulation Input software package (SIMPUT, version 2.4.7).

Table 5.2: List of the continuum parameters used in X-IFU simulations of Vela X-1. Values for the column density and photon index are taken from Watanabe et al. (2006).

Orbital Phase	Relative Flux	nH (10^{22}cm^{-2})	Photon Index
0.95 – 0.05	0.0057	1.45	0.00
0.20 – 0.30	1.0000	1.45	1.01
0.45 – 0.55	0.6010	18.5	1.01
0.70 – 0.80	1.0000	1.45	1.01

The X-ray spectrum software XSPEC (Dorman et al. 2003) was used to recreate the spectral phase models from Watanabe et al. (2006). Vela X-1 was modelled with an absorbed (tbabs) powerlaw with multiple gaussian emission lines (26 lines during

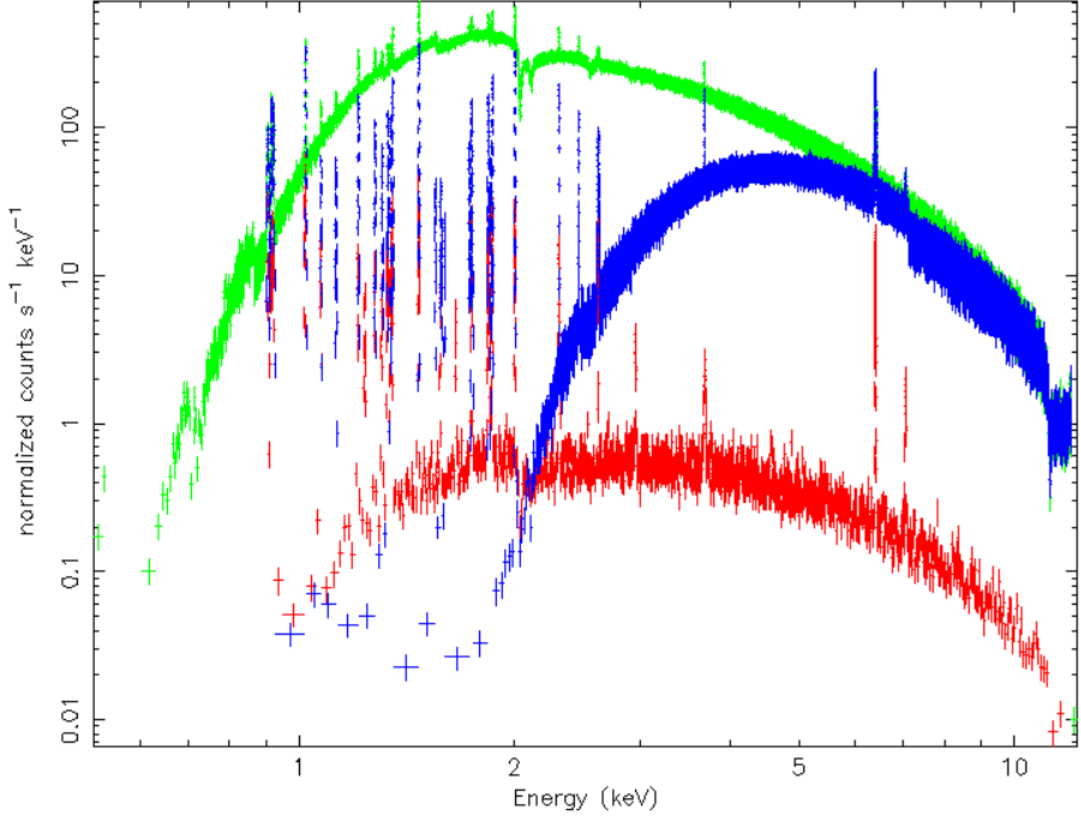


Figure 5.3: Simulated X-IFU 10 ks observation spectrum of Vela X-1 at three orbital phases. Red: $\phi = 0.00$, Green: $\phi = 0.25$, Blue: $\phi = 0.50$.

eclipse phase, 28 otherwise, see Tables 5.3 & 5.4 respectively). The reference flux of the Vela X-1 was selected to match the orbital phase with the highest observed flux, based on the phase spectral models. In this case, the highest flux is from orbital phase $\phi = 0.25$ where the flux is 3.048×10^{-9} erg/cm²/s (~ 53.4 mCrab) from 0.2 – 12.0 keV.

The three phases previously mentioned (0.00, 0.25, 0.50) were simulated with 10 ks observations and the latest RMF and ARF configurations, available by 2018-08-21, for X-IFU to compare with the previous Chandra observations. This simulation of the model of Vela X-1 from Watanabe et al. (2006) is similar to the simulations of the same model by Kitamoto et al. (2014) for Hitomi prior to the start of its mission. Comparison between previous Chandra HETGS observations of Vela X-1 and simulated observations with Athena X-IFU are shown in Fig. 5.5. The presence of the emission lines at softer X-rays (< 3 keV) and the shape of the continuum during the eclipse is much clearer in the X-IFU observation than in the original Chandra observation. Even during the brighter, non-eclipse phases, the presence of the emission lines is much clearer from the X-IFU simulated observations. Particularly during orbital phase $\phi = 0.25$, where emission lines are not immediately distinguishable from the continuum in the Chandra observations, but are far more

apparent with X-IFU. The X-IFU simulations used significantly shorter observation times than the Chandra observations (X-IFU: 10 ks, HETGS: 29 ks & 83 ks) while still resolving the details in the spectrum. This comparison demonstrates the superior capabilities of X-IFU in resolving fine details in the X-ray spectrum with shorter exposure times than current instruments. This prompted investigation into whether observations < 10 ks could still resolve the fine details, such as emission lines, to test the potential sensitivity of X-IFU.

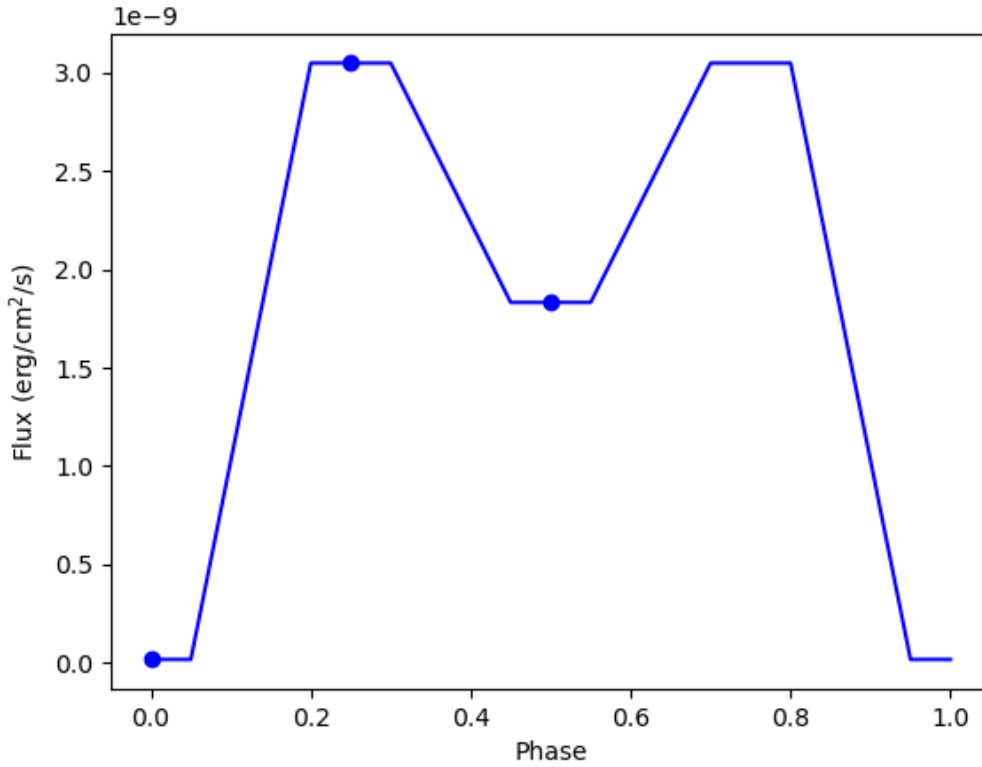


Figure 5.4: Phasecurve of Vela X-1 used for the initial X-IFU simulations for a period of 774490 s and flux in the energy range of 0.2 – 12.0 keV. Blue points represent the main simulated phases (0.00, 0.25, 0.50).

The initial simulations of 10 ks observations demonstrated the high spectral resolution of X-IFU. To further test the sensitivity, additional observations on shorter timescales were simulated to see whether it was still possible to resolve emission lines. Simulations were also made at additional phases. Phases simulated outside the defined phase bins have a flux based on linear interpolation of the relative flux between phase bins defined in SIMPUT (see Fig. 5.4). However, as previously mentioned, Vela X-1 has been observed to have high variability on the timescale of ~ 2 ks. As well as that, to track the variation of the emission lines over the course of the eclipse in detail would require observations on the scale of several ks. This is not possible with current instruments as a 83 ks observation was required from Chandra

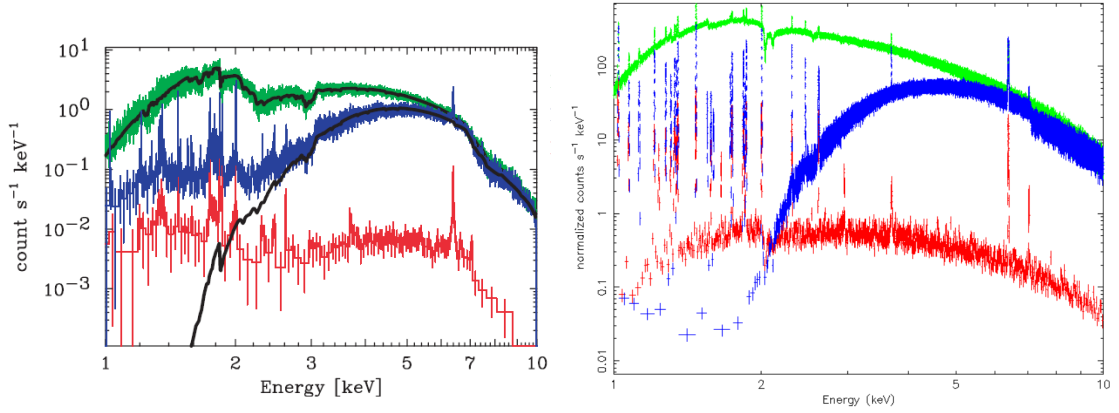


Figure 5.5: Comparison of Chandra observations and Athena simulations in 1.0 – 10.0 keV energy range. Left: X-ray spectrum of Vela X-1 from the Chandra HETGS with 83 ks (eclipse) and 29 ks observations from Watanabe et al. (2006). Right: Simulated X-IFU spectrum of the same models from 10 ks observations. Colours indicate the orbital phase: Red=0.00 (Eclipse), Green=0.25, Blue=0.50.

to resolve the spectrum during the eclipse (Watanabe et al. 2006). This is greater than 10% of the period of Vela X-1 and thus covers the entire eclipse time of the system. To investigate the sensitivity of X-IFU on these shorter timescales, simulated observations were made of 1 ks, 2 ks and 5 ks observations. The initial 10 ks simulations were also used to compare with the shorter observation simulations. The iron $K\alpha$ line was selected as the feature of the spectrum to test the sensitivity because it can be seen at all simulated phases of the orbit and is a prominent feature of the spectrum in HMXBs.

To measure the resolution of the $K\alpha$ line at the different phases and observation lengths, the spectra were fitted from 6.3-6.5 keV with the absorbed powerlaw continuum and a single gaussian line at the position of the $K\alpha$ line (6.396 keV). This is the same as the model used to build the spectrum as used in the SIMPUT files. The fitted model returns the width of the measured line with an error value. The iron $K\alpha$ line observed with the different exposure times can be seen in Fig. 5.6. It was expected that for each of the different observation times, the fitted width of the line would be within error of the input line width. However, the error calculated in the fit would vary depending on the quality of the data, which is dependent on the exposure time. Based on this assumption, if the calculated error of the line width is much greater for in one simulation than another, it can be assumed that X-IFU’s ability to resolve the spectral details are limited on the data with greater error. The fitted line width and the error is plotted with respect to the phase and

the observations lengths in Fig. 5.7.

Table 5.3: Emission lines present in the eclipse (phase = 0.00) spectral model from Watanabe et al. (2006).

Line Energy (keV)	Sigma (eV)	Normalization ($ph/cm^2/s$)
0.90406	0.8	9.0e-05
0.91493	11.0	4.7e-05
0.92077	0.9	5.3e-05
1.02075	1.0	8.5e-05
1.07241	0.8	1.91e-05
1.2098	1.3	1.43e-05
1.23618	1.6	5.9e-06
1.27592	0.9	8.7e-06
1.3064	1.3	6.6e-06
1.33122	2.3	2.03e-05
1.34238	1.2	6.3e-06
1.35057	1.5	2.58e-05
1.47068	1.2	2.63e-05
1.57719	1.3	6.0e-06
1.65752	1.0	2.8e-06
1.74247	1.7	1.96e-05
1.83924	2.9	2.11e-05
1.85271	1.1	2.8e-06
1.86299	1.6	2.34e-05
2.00339	1.7	2.32e-05
2.31035	2.2	1.76e-05
2.61857	0.6	1.38e-05
2.95657	3.4	4.9e-06
3.69431	8.6	9.3e-06
6.3958	7.2	1.7e-04
7.0512	7.2	2.21e-05

5.3 XSTAR Eclipse Simulations

5.3.1 XSTAR Emission Lines

XSTAR is a program that calculates the physical conditions and emission spectra of photoionised gas (Kallman & Bautista 2001). To test the capabilities of X-IFU in detecting emission lines that are not observable with current instruments and possibly being used to map the geometry of the eclipse, I used the XSTAR Atomic Database (Mendoza et al. 2020) to define the lines that exist within a photoionization region of comparable scale to a HMXB, in this case Vela X-1. In HMXBs, a photoionisation region is formed as a result of accretion from the massive compan-

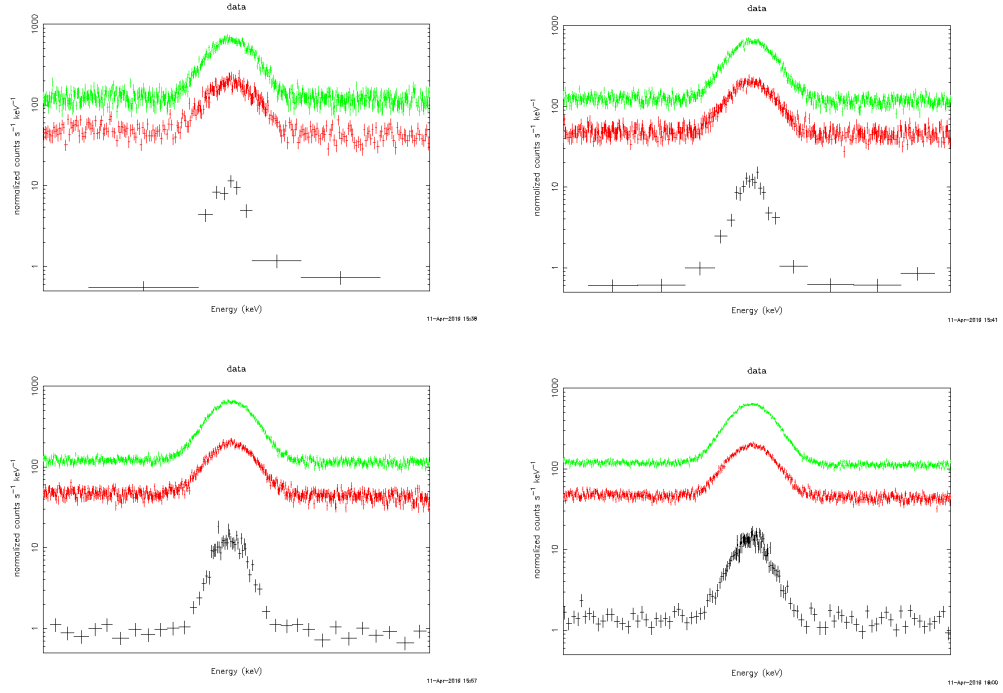


Figure 5.6: Comparison of the spectral quality of the Iron $K\alpha$ line in the Vela X-1 spectrum from 6.3-6.5 keV with different exposure times (Black: $\phi = 0.00$, Red: $\phi = 0.25$, Green: $\phi = 0.50$). Top-Left: 1 ks, Top-Right: 2 ks, Bottom-Left: 5 ks, Bottom-Right: 10 ks.

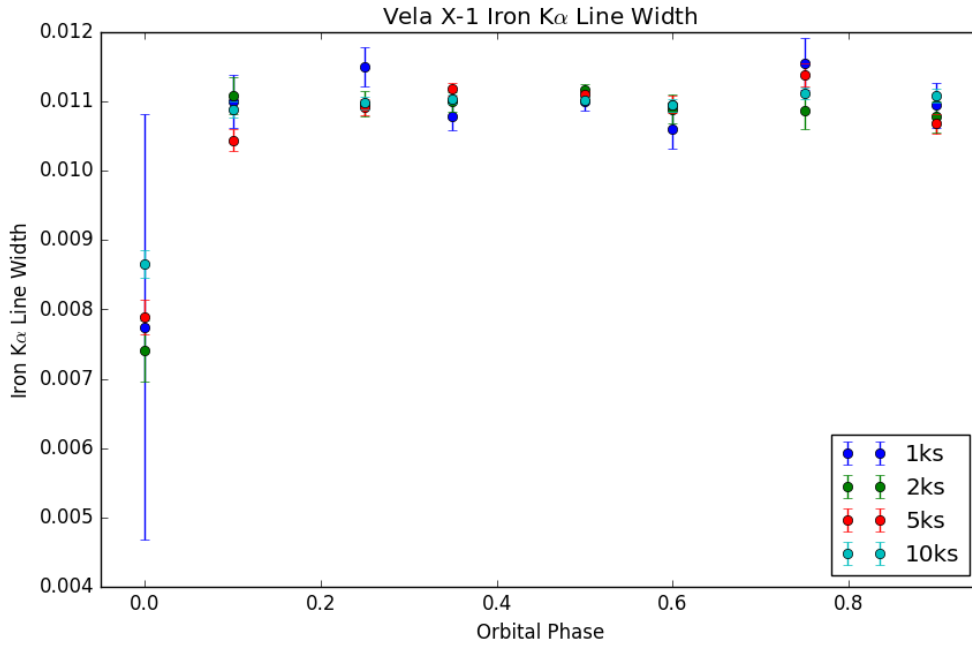


Figure 5.7: Comparison of the fitted width error of the $K\alpha$ Iron line in the simulated X-IFU Vela X-1 spectra with different exposure times.

Table 5.4: Emission lines present in the non-eclipse (phase = 0.25, 0.50) spectral model from Watanabe et al. (2006).

Line Energy (keV)	Sigma (eV)	Normalization ($ph/cm^2/s$)
0.90556	1.8	3.71e-04
0.91625	1.4	4.91e-04
0.92246	0.8	2.89e-04
1.02242	0.6	4.4e-04
1.07432	0.1	5.8e-05
1.12732	1.5	7.4e-05
1.2116	1.0	1.33e-04
1.27783	1.1	8.4e-05
1.30808	1.1	5.0e-05
1.33213	1.0	9.1e-05
1.34346	0.7	7.3e-05
1.35279	1.0	1.47e-04
1.47282	1.2	2.35e-04
1.55231	0.6	1.8e-05
1.57976	2.0	3.9e-05
1.599	0.7	1.3e-05
1.72998	0.4	3.4e-05
1.74447	2.4	1.46e-04
1.84136	2.2	1.41e-04
1.85537	0.8	3.1e-05
1.86614	1.4	1.36e-04
2.00634	1.2	2.38e-04
2.31112	0.2	1.03e-04
2.46197	0.6	6.8e-05
2.622	4.0	1.77e-04
3.6905	0.4	8.8e-05
6.3965	11.0	3.4e-03
7.0512	7.2	2.496e-04

ion onto the compact source. Previous observations and analysis of the Vela X-1 using Chandra have revealed 26 – 28 emission lines in the X-ray band depending on the observed orbital phase. It is possible that there is a significant number of unobserved emission lines due to the limited resolution of current instruments. To apply XSTAR output to X-IFU simulations, the total emissivity of the lines needs to be calculated.

For the purpose of testing X-IFU simulations, XSTAR is used to describe a spherical gas cloud surrounding an X-ray pulsar, like Vela X-1, which causes the photoionisation of the cloud. The output from XSTAR contains information on the radii of the photoionisation layers and a list of all the lines within each respective layer. The emissivity of the lines is given in volumetric flux $F_V(r)$ ($erg/cm^3/s$). This volumetric flux is not usable to build X-ray spectral models for simulations as

that requires the observed photon flux ($ph/cm^2/s$) of the individual lines (using the gaussian line model in XSPEC). In order to calculate the photon flux of the emission lines in the XSTAR model, I start by getting the luminosity of the lines.

To get the total luminosity L of any line throughout the region, the emissivity needs to be integrated with respect to the volume of the photoionisation region (Eq 5.1).

$$L = \int F_V(r) dV \quad (5.1)$$

To calculate the integrated luminosity L of each line numerically, the region is divided into a number small cubes of equal volume, n^3 . Each cube has a radial position r (Eq 5.2) with a volume dV based on Eq 5.3 and volumetric emissivity based on the XSTAR model. Binning used in the calculations depends on the number of shells in the XSTAR model and radial difference between each shell. The computational time was also a factor in choosing the binning of the volume as increased binning could drastically affect the computation time. The integrated luminosity of any emission line in the model is calculated by the sum of the product of the volume and emissivity of each cube as described in Eq 5.4. This can be done for all emission lines in the given XSTAR model.

$$r_i = \sqrt{(x_i^2 + y_i^2 + z_i^2)} \quad (5.2)$$

$$dV = V_{Total}/n^3 \quad (5.3)$$

$$L = \sum_{i=1}^{n_{xyz}} (F_V(r_i) * dV) \quad (5.4)$$

In the case of eclipsing binary systems, the observed output of the emission lines varies depending on the orbital phase of the system. In order to factor eclipsing into the emission line calculations, the luminosity calculation used here accounts for the effect an eclipsing body will have on all emission lines, depending on the observed orbital phase. If a spherical body of radius $R_{eclipse}$ eclipses the photoionization region then any of the emission cubes that overlap with the position of the eclipsing body will contribute nothing to the emission output. When summing the luminosity of each cube (Eq 5.4) the position of the cube is checked with respect to the origin of the eclipsing body. If the distance d (Eq 5.5) from the cube to the origin of the eclipsing body is less than $R_{eclipse}$, with respect to the observer, then the that cube is eclipsed and the luminosity of that cube counts as 0 towards the total luminosity (Eq 5.6).

$$d = \sqrt{(x - x_{eclipse})^2 + (y)^2} \quad (5.5)$$

$$R_{eclipse} > d \Rightarrow L = 0 \quad (5.6)$$

Once the luminosity of the lines is calculated, the flux F_ν of any given line from the spherical region can be calculated as long as the distance from the observer D is known (Eq 5.7). In the case of Vela X-1 the distance is known to be approximately 2.42 kpc (Bailer-Jones et al. 2018). To use this flux to build a model of the spectrum in XSPEC for simulating X-IFU observations, the flux needs to be converted to photon flux ($ph/cm^2/s$). For emission lines, the photon flux is calculated based on the energy of the line E_l (Eq 5.8).

$$F_\nu = \frac{L}{4\pi D^2} \quad (5.7)$$

$$F_{ph} = \frac{F_\nu}{E_l} \quad (5.8)$$

The modelling of the emission lines also requires the width of the lines. For the purpose of the simulations presented here, the full width at half maximum value of the line derived from Doppler broadening (Eq 5.9) is used as approximation of the emission line width input ΔE_l (Eq 5.10). To use the values for the XSPEC spectrum models, the line energy and width is converted to keV.

$$\Delta f = \sqrt{\frac{8kT \ln 2}{mc^2}} f_0 \quad (5.9)$$

$$\Delta E_l = h(f_0 + \Delta f) - h(f_0 - \Delta f) \quad (5.10)$$

5.3.2 Simulations of XSTAR Models

The line emissivity calculations used on XSTAR models were used to build X-ray spectral models of a hypothetical photoionization region in a binary system, similar to Vela X-1. The continuum of these models used the absorbed powerlaw continuum of Vela X-1, as reported by Watanabe et al. (2006), with the emission line positions, widths and normalizations of the XSTAR line calculations. As described in the previous section, the emission line normalization accounts for an eclipse of the photoionization region, in this case using the same periodicity as Vela X-1 in this eclipse. As a result, the phases defined in the SIMPUT file were increased in comparison to the initial simulations using Watanabe et al. (2006) models. This was done to better account for the gradual change instead of relying on the flux

interpolation of SIXTE (see Table 5.6). To determine what phase range of a given XSTAR model was being eclipsed, 2D distribution maps of the photoionization region luminosity were calculated for a selection of emission lines (see Fig. 5.9 for an example). The luminosity at any point on the maps is calculated by summing all the luminosity cubes, as described in Section 5.3.1, along the line of sight. These maps were used in order to visualise the intensity gradient of any given line, showing at which phases the eclipse influences the emission line total luminosity.

The first results presented here are the result of simulations using an XSTAR model with parameters that are detailed in Table 5.5. The size of the modelled region relates to the equation for the ionization parameter ξ (see Eq 1.16), such that if the equation is rearranged, the radius of the most inner sphere of the region is given by Eq 5.11.

$$R_{inner} = \sqrt{L/n\xi} \quad (5.11)$$

The number of shells within this modelled region, line populations, abundances etc. is calculated by XSTAR based on the additional parameters such as the column density, temperature and elemental abundances. Abundances were set at solar values for the purpose of this study. The parameters in Table 5.5 corresponds to a spherical region comparable in size to HD 77581 so that the eclipse in the line calculations is apparent (see maps in Fig. 5.9 for example). However, there is no total eclipse of the photoionization region with this model. Photoionization regions modelled with XSTAR does not provide a one to one comparison to similar regions in wind-fed HMXBs as it does not account for the more complex geometry. In the case of Vela X-1, the accretion wake is not a perfectly spherical cloud and there is the additional photoionization wake and tidal stream which may be the source of some emission lines (see Fig. 5.1 & 5.2). As such, these results do not represent an accurate model of prediction for Vela X-1 but rather a proof of concept for observing the gradual change in the intensity of emission lines in the X-ray spectrum in an eclipsing binary such as Vela X-1 and other HMXBs.

Spectra of the simulated observations of the modelled XSTAR lines are shown in Fig. 5.8. The total line population from this XSTAR model initially resulted in spectra with flux noticeably higher than the kind of flux observed from Vela X-1. This was largely due to my own trouble still learning how to better refine the XSTAR model to the characteristics desired for this analysis. This is elaborated on in Appendix A. In order to reduce the intensity of the lines in this model to a more desirable level, the absorption component of the XSTAR model was also applied to the X-ray spectral model. This results in lower line intensities and lines ≤ 1 keV were effectively removed. This, however, only adds to this model not being comparable to real systems. While first analysis if this model provided promising

insights tracking the change of emission lines (see Fig. 5.14), the XSTAR model was revised to better match eclipsing HMXBs where the accretion region is possibly completely obscured during the eclipse.

Table 5.5: Key parameters of the XSTAR model used for X-IFU simulations. All elemental abundances were left at the default value.

Parameter	Value (Units)
Temperature	1×10^7 K
Density	6×10^{10} cm $^{-3}$
Luminosity	1.6×10^{36} erg/s
Column Density	1×10^{23} cm $^{-2}$
Ionization Parameter	1×10^6 erg*cm/s

Table 5.6: Details of the phase-dependent spectrum for XSTAR models as defined in the SIMPUT used for X-IFU simulations. Relative flux was based on the orbital phase with the highest flux ($\phi = 0.25$ & 0.75).

Orbital Phase	Relative Flux	nH (10^{22} cm $^{-2}$)	Photon Index
0.00	0.0078	1.45	0.00
0.01	0.0084	1.45	0.00
0.02	0.0101	1.45	0.00
0.03	0.0114	1.45	0.00
0.04	0.0119	1.45	0.00
0.20	1.0000	1.45	1.00
0.30	1.0000	1.45	1.00
0.45	0.6058	18.5	1.00
0.55	0.6058	18.5	1.00
0.70	1.0000	1.45	1.00
0.80	1.0000	1.45	1.00
0.96	0.0119	1.45	0.00
0.97	0.0114	1.45	0.00
0.98	0.0101	1.45	0.00
0.99	0.0084	1.45	0.00

5.3.3 Revising XSTAR Model and Simulation Parameters

While the first simulation results using XSTAR models showed promise in spectral reconstruction, I wanted to revise the modelling so that the theoretical geometry of the simulations more closely matching the characteristics of Vela X-1. In particular by making the spherical ionization region of the XSTAR model more comparable to the accretion wake in Vela X-1. The parameters for the revised XSTAR model

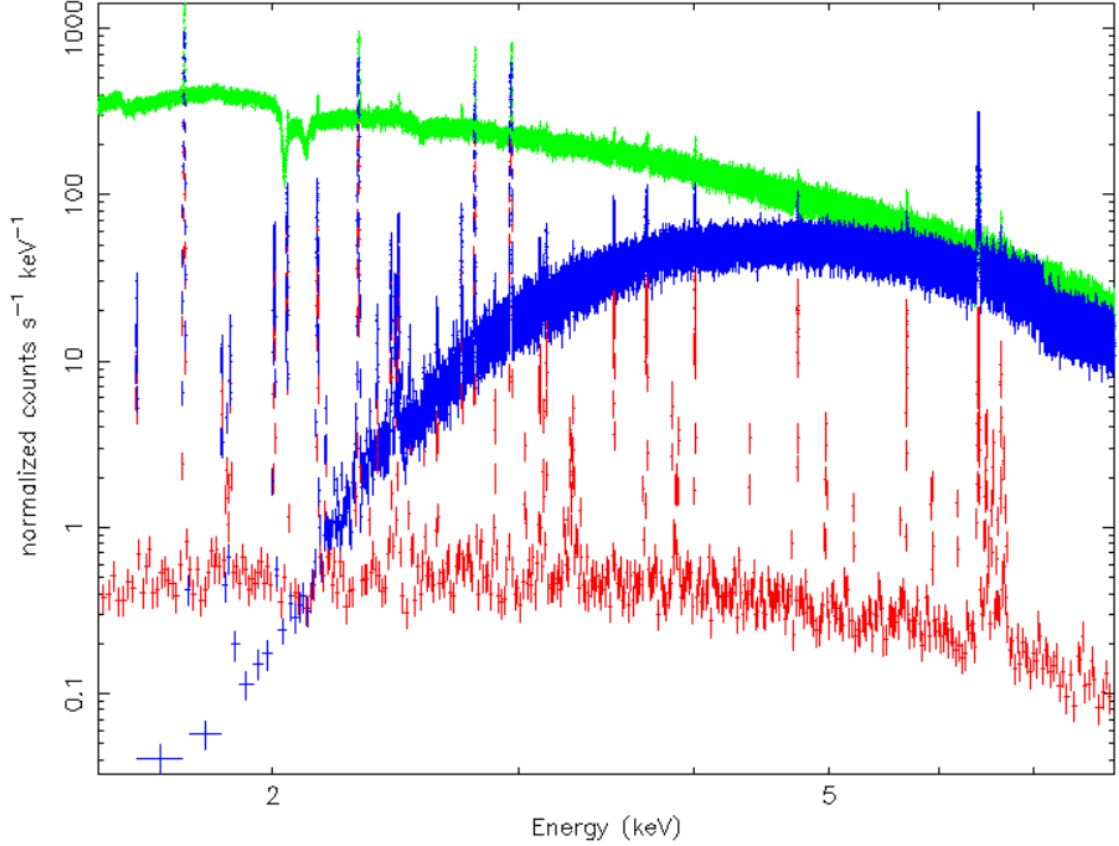


Figure 5.8: Spectra from simulated 5 ks observations with X-IFU of the XSTAR model lines. Due to the high column density applied to the line models in XSPEC, lines at lower energies are not visible. Spectra are shown in the energy range 1.5 – 8.0 keV. Red: $\phi = 0.00$, Green: $\phi = 0.25$, Blue: $\phi = 0.50$.

were based on the study of the stellar wind environment in Vela X-1 by Malacaria et al. (2016). The final values used are shown in Table 5.7. The result is a spherical photoionization region on the scale of 10^{12} cm. This size scale has also been found to be the size of the accretion wake in Vela X-1 according to simulations by Manousakis (2011), which is what the sketch in Fig. 5.2 is based on. As a result, the model of the eclipse of the photoionization region now completely blocks line emission for a time during the eclipse. Using the 2D luminosity distribution maps of this new model, the total eclipse of the photoionization region was found to be from orbital phases 0.97 – 0.03, using the geometric parameters known for Vela X-1. A visualization of the eclipse can be seen in Fig. 5.10.

The details on how the modelled continuum varies throughout the orbit in these simulations are shown in Table 5.8. The centre of the modelled photoionization region is covered by the eclipse from the orbital phases 0.90 – 0.10. Assuming that the pulsar is at the centre of this region from the point of view of the observer, the continuum is modelled based on the eclipse continuum derived from Watanabe et al. (2006) during this phase range. The spectra at three separated phases using

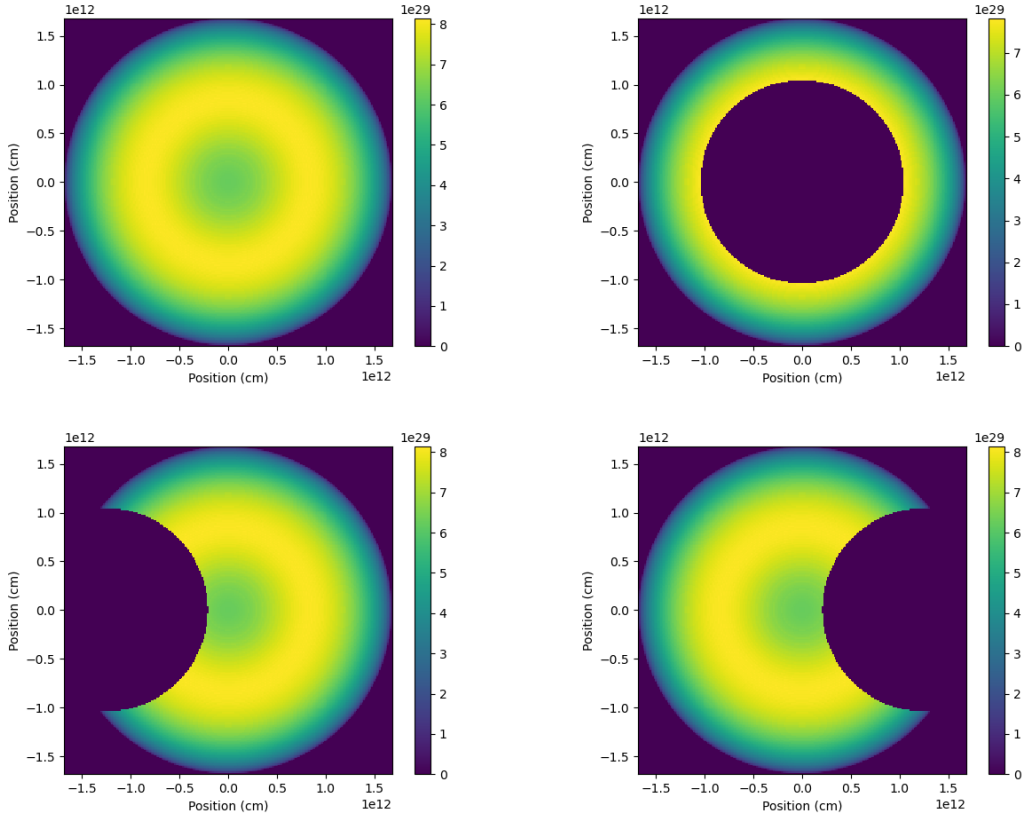


Figure 5.9: Plots of the integrated luminosity of the emission lines of the XSTAR models, using the Al XII line. Top-Left: Luminosity map with no eclipse. Top-Right: Eclipse at superior conjunction ($\phi = 0.00$). Bottom-Left: Partial eclipse ($\phi = 0.98$). Bottom-Right: Partial eclipse ($\phi = 0.02$).

the revised XSTAR model and continuum models are shown in Fig. 5.11. As the lines are completely hidden during the eclipse phase (0.00) this was not shown in the comparison, instead using the phase at 0.05 where the continuum uses the eclipse model and the lines are still heavily eclipsed. The lines in the XSTAR model used for these revised simulations are noticeably brighter than in any previous observations of Vela X-1. This indicates that more realistic modelling is needed, likely accounting for more accurate elemental abundances in the model, as has been documented for Vela X-1 by Giménez-García et al. (2016). However, the more realistic eclipse modelling can provide insight onto how emission lines vary in Vela X-1 on scales of a few thousand seconds.

At ~ 6.4 keV there is an iron line complex which is used to observe the gradual change in the line profiles over the course of multiple 5 ks simulated observations (see Fig. 5.12). With X-IFU showing sufficient sensitivity and resolution to observe this gradual change in X-ray emission line profiles, it is possible that X-IFU may be used in order to distinguish the various morphology associated with different emission lines. In Fig. 5.13 there are a few luminosity maps associated with different emission

Parameter	Value (Units)
Temperature	5×10^6 K
Density	1.5×10^{11} cm $^{-3}$
Luminosity	1.6×10^{36} erg/s
Column Density	1.85×10^{23} cm $^{-2}$
Ionization Parameter	1×10^5 erg*cm/s

Table 5.7: Key parameters of the XSTAR model used for X-IFU simulations to better replicate the accretion wake of Vela X-1. All elemental abundances were left at the default value.

lines from revised XSTAR model, which shows how drastically the morphology of the emission lines can vary, depending on the ion of origin, within these regions of photoionization.

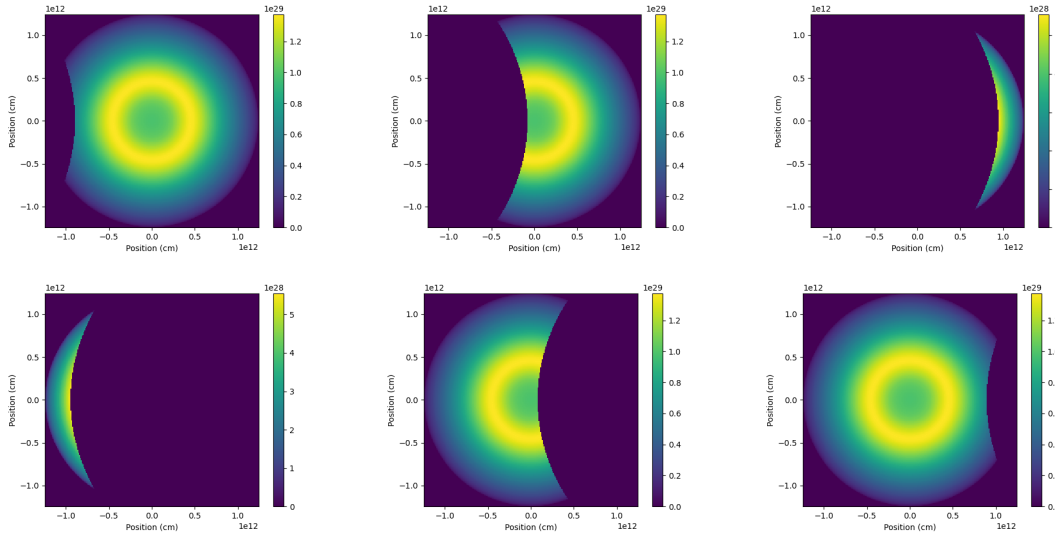


Figure 5.10: Plots of the integrated luminosity of the emission lines of the updated XSTAR model, using a Fe XVIII line. Top-Left: $\phi = 0.85$. Top-Middle: $\phi = 0.90$. Top-Right: $\phi = 0.95$. Bottom-Left: $\phi = 0.05$. Bottom-Middle: $\phi = 0.10$. Bottom-Right: $\phi = 0.15$.

5.4 X-IFU Simulations Discussion

The results of simulating observations of Vela X-1 using the spectral models from Watanabe et al. (2006) provide a good demonstration of the advantage Athena X-IFU will have over current instruments with regards to the sensitivity of the instrument. Comparison of the observations from Watanabe et al. (2006) and the simulated observations of the models from the same study, with lower observations times, using X-IFU (see Fig. 5.5) shows that the shape of the continuum and the presence of the emission lines can be clearly detected with significantly shorter

Table 5.8: Details of the variable spectrum for XSTAR models as defined in the SIMPUT used for X-IFU simulations. Relative flux was based on the calculated flux of the models in XSPEC.

Orbital Phase	Relative Flux	nH ($10^{22}cm^{-2}$)	Photon Index
0.00	0.0037	1.45	0.00
0.03	0.0037	1.45	0.00
0.04	0.0044	1.45	0.00
0.05	0.0133	1.45	0.00
0.06	0.0294	1.45	0.00
0.07	0.0496	1.45	0.00
0.08	0.0718	1.45	0.00
0.09	0.0939	1.45	0.00
0.10	0.9264	1.45	1.00
0.11	0.9453	1.45	1.00
0.12	0.9616	1.45	1.00
0.13	0.9748	1.45	1.00
0.14	0.9850	1.45	1.00
0.15	0.9922	1.45	1.00
0.20	1.0000	1.45	1.00
0.30	1.0000	1.45	1.00
0.45	0.6707	18.5	1.00
0.55	0.6701	18.5	1.00
0.70	0.9984	1.45	1.00
0.80	0.9984	1.45	1.00
0.85	0.9909	1.45	1.00
0.86	0.9838	1.45	1.00
0.87	0.9737	1.45	1.00
0.88	0.9606	1.45	1.00
0.89	0.9445	1.45	1.00
0.90	0.9258	1.45	1.00
0.91	0.0935	1.45	0.00
0.92	0.0715	1.45	0.00
0.93	0.0494	1.45	0.00
0.94	0.0293	1.45	0.00
0.95	0.0133	1.45	0.00
0.96	0.0044	1.45	0.00
0.97	0.0037	1.45	0.00

observations. In particular, the Chandra observation of the eclipse was 83 ks in order to resolve the spectrum, while the 10 ks observation with X-IFU resolved the spectrum with excellent clarity, which would allow for multiple observations during the eclipse window. This would allow for higher phase resolution observations that observe how the spectrum varies over the eclipse on at least a 10 ks timescale.

Since such clarity was achieved with 10 ks observations with X-IFU, the sensitivity was further tested with the fitting of the $K\alpha$ present in the simulated spectrum at

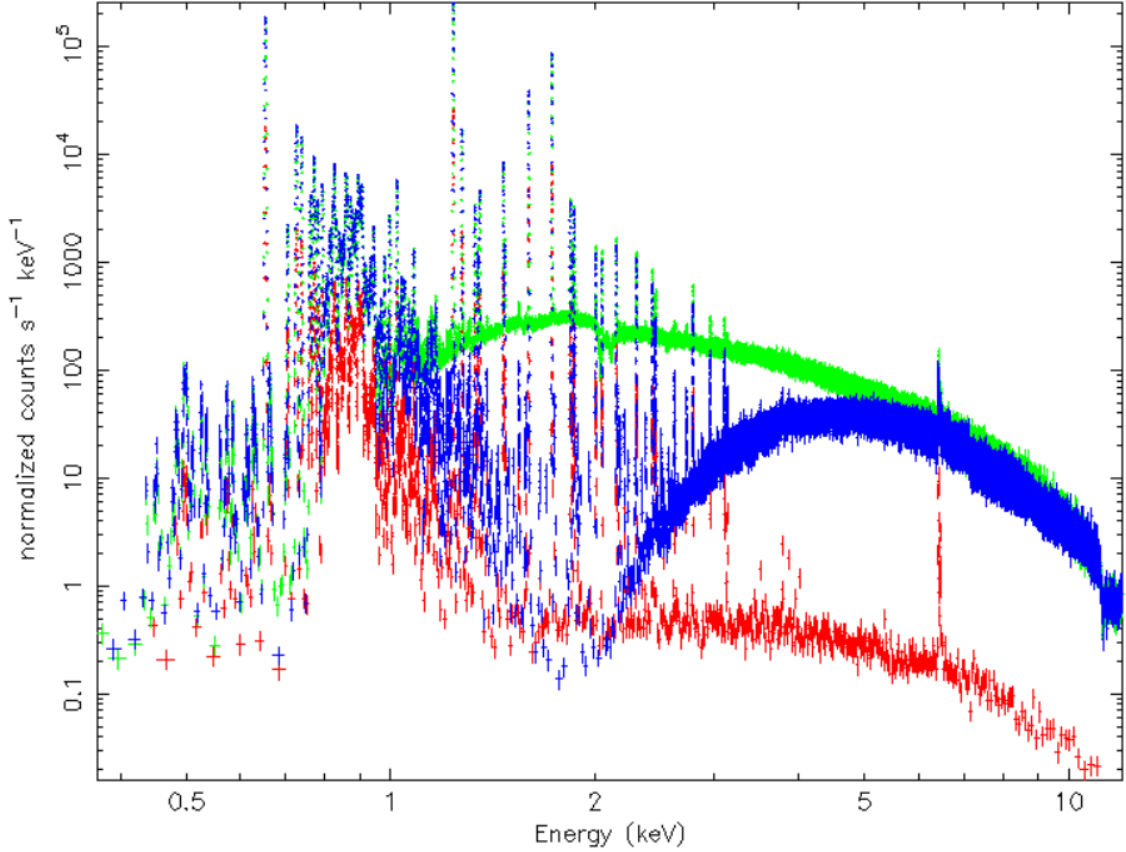


Figure 5.11: Spectra of 5 ks observations using lines from XSTAR models. Red: $\phi = 0.05$, Green: $\phi = 0.25$, Blue: $\phi = 0.50$.

shorter timescales. Figure 5.7 shows the fitted values of the iron $K\alpha$ line width and the associated error calculated from XSPEC model fittings at different simulated phase observations with 4 different exposure times. For simulated observations of ≥ 2 ks, the error of the fitted line width on the iron $K\alpha$ line was consistently small and within the range of the width value in the input spectrum. However, for 1 ks observations, the measured error was significantly bigger during the eclipse phase. This suggests that for dim sources or low flux states of transient sources, X-IFU may not as accurately resolve the fine spectral details with such sort observations. The fitted error of the 1 ks observations was consistent with the other timescales outside of eclipse phase so such a timescale may still be viable for bright sources and/or bright spectral states. Between the 1 ks observations outside of eclipse and 2 ks observations at all tested phases, this is a good indication that X-IFU will be capable of further investigating short timescale flares observed in systems like Vela X-1, as seen previously by Odaka et al. (2013).

The simulated observations of spectra using the first calculated XSTAR lines were done using 5 ks observations. This allows for observations that are shorter than the 0.01 phase resolution (~ 7.7 ks) during the eclipse, as detailed in Table 5.6.

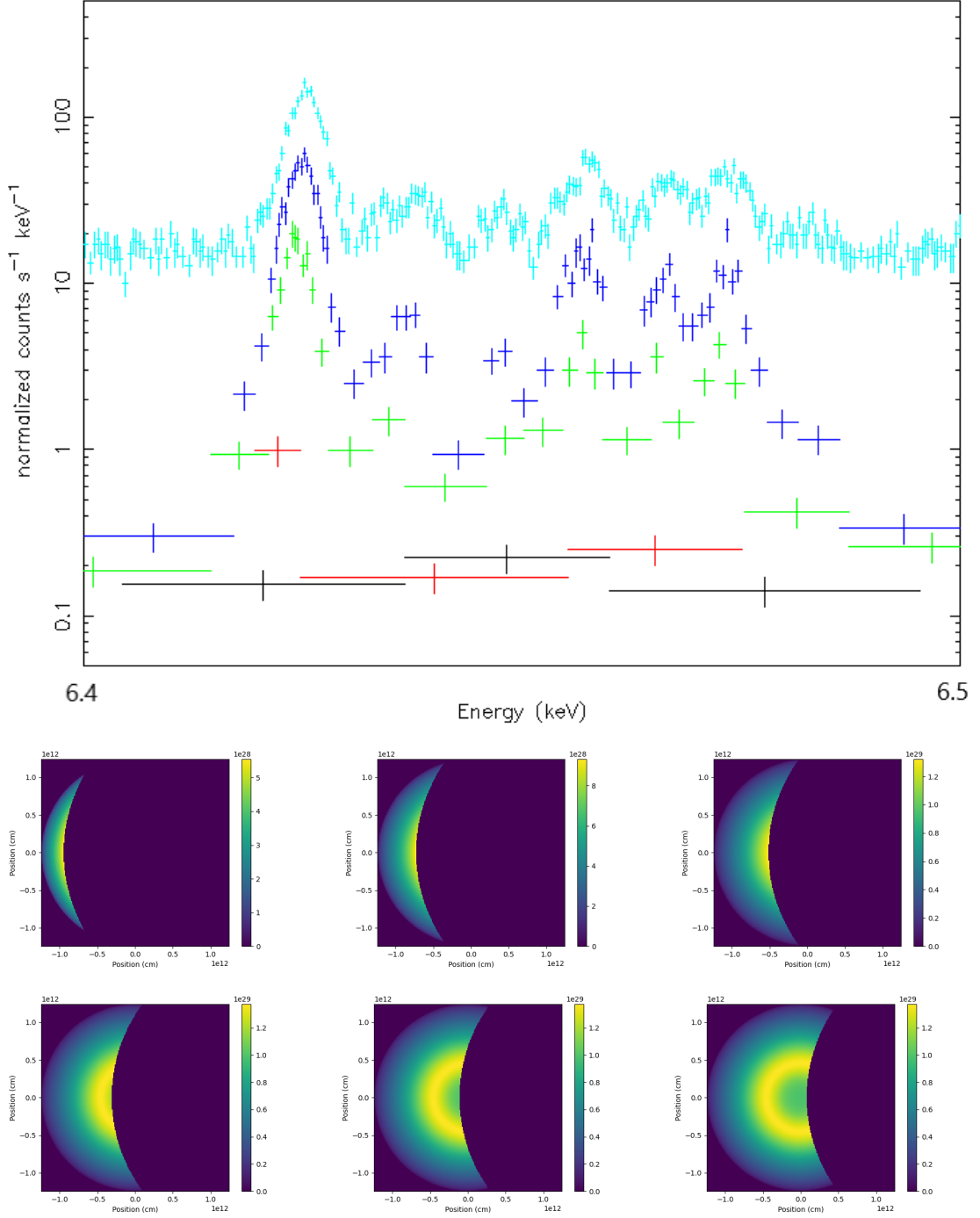


Figure 5.12: Top: Spectra of 5 ks observations using lines from XSTAR models. Centre-Left: $\phi = 0.05$. Centre-Middle: $\phi = 0.06$. Centre-Right: $\phi = 0.07$. Bottom-Left: $\phi = 0.08$. Bottom-Middle: $\phi = 0.09$. Bottom-Right: $\phi = 0.10$.

Based on the previous analysis testing different observation times on the iron line, 5 ks should be more than sufficient to resolve the changes in line profiles, which will allow for eclipse mapping of the photoionization region through these observations. The line used in the XSTAR model to test the observations of variance was the Al XII (H-like) line at 1.598 keV, as this was the brightest line in this XSTAR model. Over

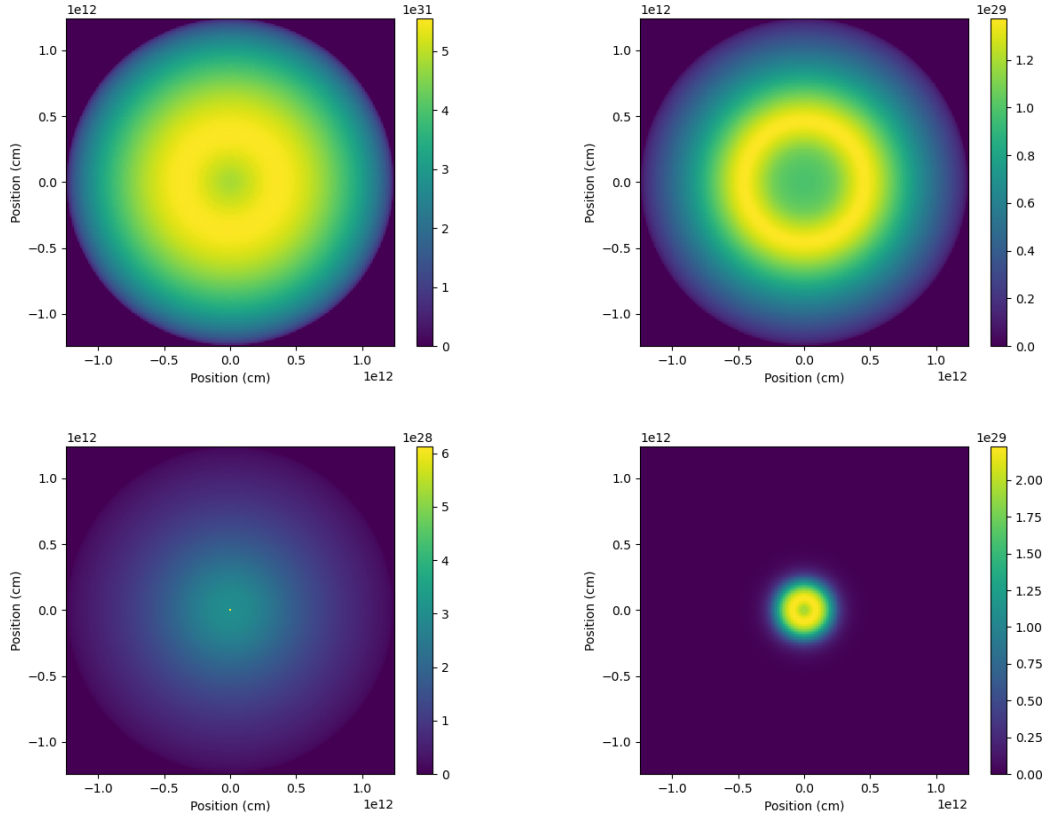


Figure 5.13: Example of the radial luminosity of different lines as defined by the XSTAR model. Top-Left: O VIII, 0.637 keV. Top-Right: Fe XVIII, 6.422 keV. Bottom-Left: Cl XVII, 2.962 keV. Bottom-Right: Fe XXV, 6.664 keV.

the course of several simulated observations during the eclipse, the Al XII line was fitted in XSPEC to calculate the observed photon flux of the line, which is the normalization parameter of the gaussian line model. The results of measuring the change in the normalization of the Al XII emission line is shown in Fig. 5.14. The input value for the normalization of the Al XII (H-like) line falls within the fitted confidence range for all 7 simulated observations shown. This further supports the that X-IFU will be capable of mapping the change in fine spectral details such as emission line profiles over the course of an eclipse. Such sensitivity could allow X-IFU to be used to map the morphology of different emission lines in such photoionization regions, creating distribution maps similar to presented here in Fig. 5.13, except creating them based on the observed changes in line intensity.

The revised XSTAR model with input parameters similar to the accretion wake of Vela X-1 provides better insight to the ability of X-IFU to observe transient emission lines. With a modelled region of the same scale as the accretion wake of Vela X-1, it also allows for a chance to demonstrate the potential for eclipse mapping of binary systems with X-IFU. In Fig. 5.12, the spectra of the iron line complex at 6.4 keV is shown with a series of 5 ks observations as the photoionization region emerges

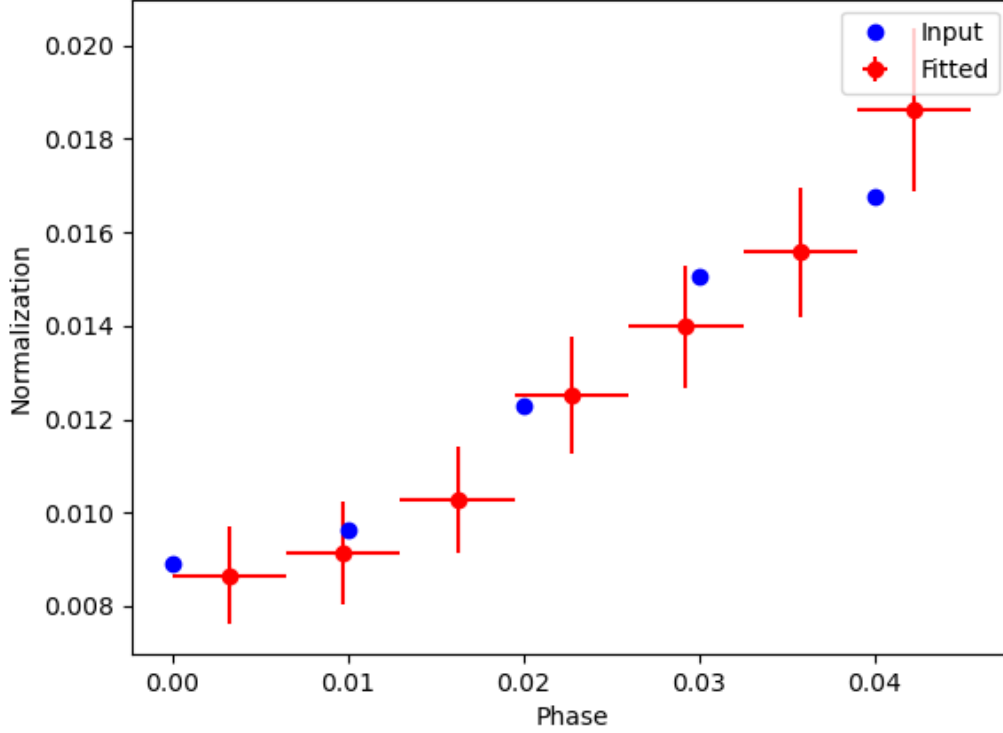


Figure 5.14: Plot of the input and measured line normalization for the Al XII line at 1.598 keV from 5 ks simulations. Errorbars represent the 90% confidence range of the fitted normalization values.

from the total eclipse. Even within a few ks outside eclipse, where only the edge of the region is visible, the emission lines start to become apparent in the spectrum. It should be noted, as previously mentioned, that the overall line intensities of this model are larger than has been observed in Vela X-1. As such it may be optimistic to say that X-IFU will be capable to observe spectral details so soon after an eclipse, but given the strong sensitivities demonstrated on the ks timescale observations I would argue it is still a possibility.

Similar to what was studied in the first XSTAR model used for analysis, this revised XSTAR model was also used to investigate more quantitatively how X-IFU will observe the gradual change in emission line profiles. However, fitting the X-ray spectrum in XSPEC was not used this time. Rather the events from the simulated 5 ks observations were used to take the total counts in a narrow energy range that corresponds to an emission line and comparing this with the input flux of the line. The results of tracking the change in line profiles based on the counts is shown for the O VIII line (0.653 keV), the brightest line in this model, and the previously discussed iron line complex (6.4–6.5 keV) in Fig. 5.15. The change in the counts in the narrow energy ranges of the emission lines correlates very well with the profile of the input

flux. There is a noticeable discrepancy at the last phase point on the plots. This is a result of a dramatic change in the spectral continuum during that observation phase. In the modelling of the orbit, it corresponds to when the centre of the region, and thus the pulsar, emerge from the eclipse and the continuum intensity increases to match the non-eclipse continuum models from Watanabe et al. (2006). Hence, there is a notable change in the counts observed during that orbital phase. As the counts follows the input line profile so closely prior to this discrepancy, I propose that this further supports the ability of X-IFU to observe these gradual spectral changes, which could be applied to eclipse mapping the accretion/photoionization regions of HMXBs such as Vela X-1.

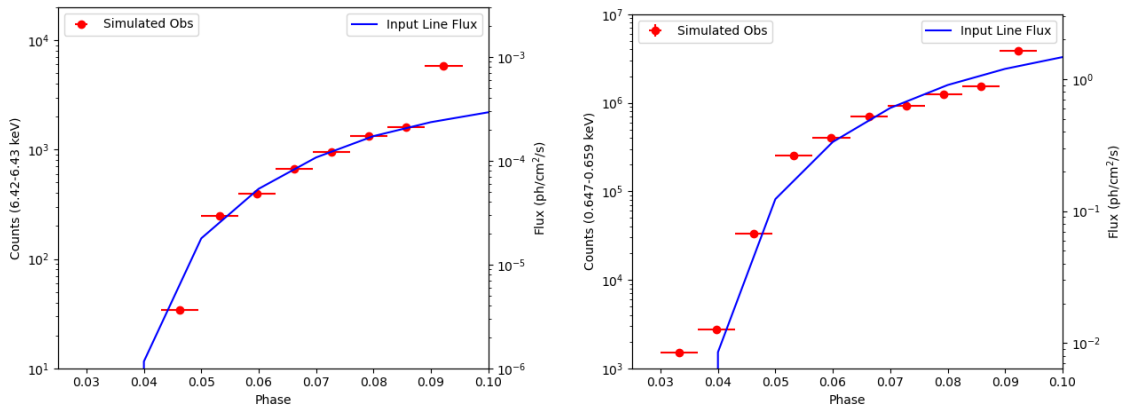


Figure 5.15: Plots of the event counts in narrow emission lines (red points) and the input flux (blue line) at different orbital phases with simulations of the revised XSTAR model. Left: Fe lines from the emission line complex at 6.4–6.5 keV. Right: O VIII line at 0.653 keV, one of the brightest lines in the model.

5.5 Summary & Conclusions

Simulated observations with X-IFU based on previous modelling of Vela X-1 by Watanabe et al. (2006) and lines derived from XSTAR models provide a demonstration of the resolving power of Athena X-IFU and its potential use in observing HMXBs. Based on simulations with SIXTE and SIMPUT, using the latest IRFs, RMF, and ARF for Athena X-IFU, it will be capable of resolving spectral details such as emission lines with observations as short as 2 ks. Such sensitivity is of prime importance for further study of HMXBs, where intense flaring has been observed on such timescales in systems such as Vela X-1 (Odaka et al. 2013). Multiple observations on the scale of a few ks during a modelled eclipse with line input from XSTAR shows very promising results that X-IFU will also be able to track how emission line profiles change during events such as an eclipse. This could provide a new method of mapping the geometry of eclipsing HMXBs, to observe if the emis-

sion region is totally eclipsed and to map the morphology of photoionization regions that are formed as a result of accretion in these systems. I intend to further refine the simulations presented in this chapter and to prepare the results for publication in the future.

Chapter 6

Sensitivity of CTA on HMXBs

As previously discussed in Ch. 1 (Fig. 1.8), there are currently two models for HMXBs systems that are also classified as gamma-ray binaries; firstly is Be star-pulsar binaries and secondly is microquasars. These are considered gamma-ray binary candidates due to the presence of relativistic jets, which are capable of accelerating particles to very high energies that can result in gamma-ray emission. However, while all systems currently classed as gamma-ray binaries have been detected at TeV energies, only one system that is a known microquasar has been confidently detected at TeV.

As of writing, the only microquasar that has been solidly detected at TeV energies is SS433. This detection required years of observations. Cygnus X-1 is a microquasar that had a possible detection at TeV (Zdziarski et al. 2009), but this has yet to be solidified. Even in the case of gamma-ray binaries that have been detected regularly at TeV energies, current instruments do not have the sensitivity to resolve transient emission on the same timescale as counterparts at other wavelengths, such as X-ray and GeV.

Using SS433 as the example, I present simulations of CTA observations to test the sensitivity of the array and provide possibility of further study of microquasars and other HMXBs with Target of Opportunity (ToO) observations. The goal is to determine on what timescales may CTA be able to detect sources like SS433 and similar systems, while also providing an idea of the level of variance CTA could detect. This analysis is a part of an ongoing CTA consortium paper to explore the feasibility of detecting galactic transients with the CTA that is currently ongoing.

6.1 SS433

SS433 is a binary system that was the first detected microquasar containing a supergiant star that is overflowing its Roche lobe with matter accreting onto a compact object. The compact source is likely a 10-20 M_{\odot} black hole (Gies et al. 2002) orbit-

ing a $\sim 11 M_{\odot}$ A3-7 star with a periodicity of 13.1 days and an orbital separation of $\sim 56 R_{\odot}$ (Hillwig et al. 2004). An accretion disc is formed around the black hole (Shakura & Sunyaev 1973) which drives two relativistic jets ejecting from the system at a velocity of $0.26c$ and precess every 162.4 days (Margon & Anderson 1989; Eikenberry et al. 2001). SS433 is located within the supernova remnant W50 and the interaction between the jets and the surrounding region has been observed in radio and X-ray (Seward et al. 1980; Dubner et al. 1998).

While for many years no gamma-ray emission was detected from SS433, predictions were made for gamma-ray radiation from the jets (e.g. Heinz & Sunyaev 2002). In recent years, however, SS433 has been detected at both GeV energies, with Fermi-LAT, and TeV energies, with the High Altitude Water Cherenkov Experiment (HAWC).

6.1.1 GeV Detections with Fermi-LAT

The presence of GeV emission in the region of SS433 was first confirmed by Bordas et al. (2015) analysing five years of Fermi-LAT data. Further analysis since by Sun et al. (2019); Rasul et al. (2019); Xing et al. (2019) have corroborated this discovery with analyses using > 9 yrs of Fermi-LAT data. These analyses are very model dependent and can lead to very different conclusions on the position and extension of the source. In Rasul et al. (2019) authors report evidence at the 3σ level for the modulation of the GeV emission with the precession period of the jet. The results suggest that at least some of SS433's gamma-ray emission originates close to the base of the jet. A TS map of the Fermi-LAT data of SS433 by Rasul et al. (2019) is shown in Fig. 6.1.

6.1.2 TeV Detection with HAWC

Abeysekara et al. (2018) reported results of HAWC Observatory observations of SS433 collected between November 2014 and December 2017 (see Fig. 6.2). In 1017 days of measurements with HAWC, an excess of gamma-rays with a post-trials significance of 5.4σ has been observed in a joint fit of the eastern and western interaction regions of the jets of SS433. The quality of the data only allows upper limits to be set on the angular size of the emission regions, namely 0.25° for the east hotspot and 0.35° for the west hotspot at 90% confidence level. The VHE gamma-ray flux is consistent with a hard E^{-2} spectrum, though current data from HAWC are not of sufficient significance to constrain the spectral index. The reported HAWC flux at 20 TeV is $2.4 \times 10^{-16} \text{ TeV}^{-1} \text{cm}^{-2} \text{s}^{-1}$ at the eastern lobe (e1), and $2.1 \times 10^{-16} \text{ TeV}^{-1} \text{cm}^{-2} \text{s}^{-1}$ at the western lobe (w1). HAWC detects gamma-rays from the interaction regions up to at least 25 TeV, which up to now, is the highest

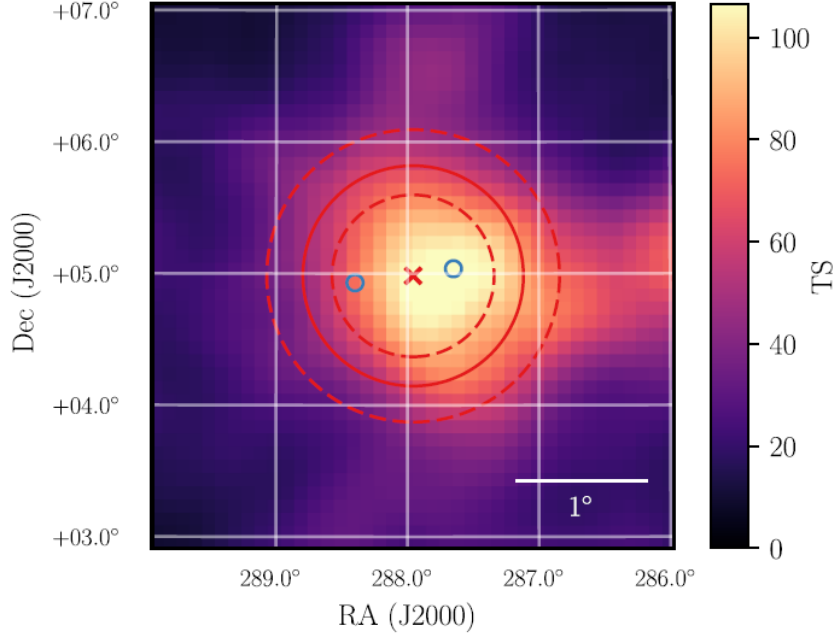


Figure 6.1: TS map centred on SS433. Map is based on analysis of 9 yrs of Fermi-LAT data by Rasul et al. (2019). Blue circles represent the lobe positions according to Abeysekara et al. (2018), the red cross represents the position of SS433 and the red circles represent the optimised extension (solid circle) with the 1σ uncertainty (dashed circles).

energy measured from microquasars. While Rasul et al. (2019) suggests that some of the detected GeV emission originates at the base of the jets, the TeV observations show little indication of emission from the base of the jets. However this could be due to the limits of the sensitivity of HAWC. A central emission source of TeV in SS433 may be detectable using CTA.

6.2 CTA Simulations

To test the capability of CTA to detect emission from SS433, I simulated the source with both the East and West lobes as extended sources of VHE from 0.1 - 100.0 TeV. Observations of 10, 30 and 50 hours exposure were simulated and the TS and flux of each lobe were calculated for both the North and South site, using the prod3b-v2 IRFs (Maier et al. 2019). These simulations were repeated for different extension levels on each of the lobes (see Table 6.1 for extension values simulated) as the true extension of the lobes is currently unknown and could not be determined from the HAWC detection. These simulations will provide a demonstration as to whether CTA will be able to detect the lobes of the lobes of SS433 within a timescales of just 2 days as opposed to the 1017 days required by HAWC. It will also indicate how the significance of the detection may vary depending on the extension of the lobes.

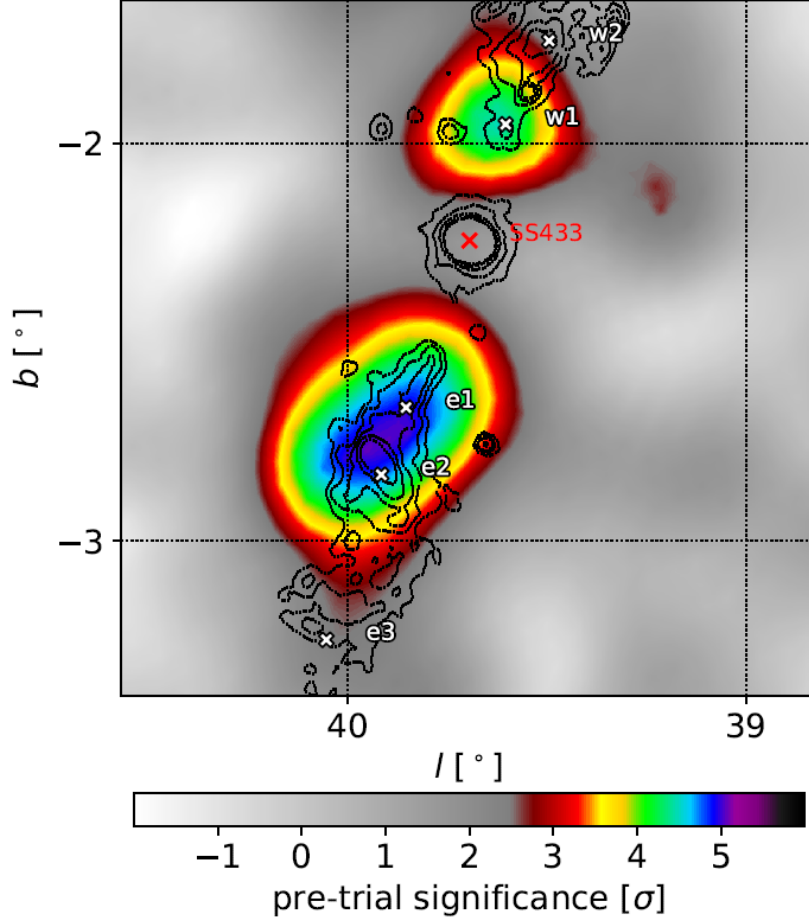


Figure 6.2: TeV image of the SS433 region based on 1017 days of HAWC data from Abeysekara et al. (2018). The east and west lobes observed in X-ray are indicated (e1, e2, w1 & w2) and the location of the binary source (red cross).

Table 6.1: Extension models used for the East and West lobes of SS433 in CTA simulations.

Model	σ_w	σ_e
1	0.001	0.001
2	0.0625	0.0875
3	0.175	0.125
4	0.26	0.1875

The results of simulating the lobes of SS433 are shown in Table 6.2 for the North IRFs and Table 6.3 for the South IRFs. For lobes with extensions approximating to a point source (Model 1), detections as high as $TS \sim 184$ were obtained from 10 hrs observation simulations. This is a good indication that for near point-like sources, CTA will be able to make detections on timescales as short as several hours.

However, for more extended sources, 10 hrs will not be sufficient. Lobes with high extension (Model 4) returns $TS < 10$ for both the North and South IRFs at

10 hrs. With simulated observations of 50 hrs the high extension model is best detected by the South IRF. North IRF returns $TS < 10$ on the West lobe where the South IRF returns $TS > 25$ for both East and West. This suggests that even for highly extended sources, CTA will be capable of good detections on timescales of 1-2 days, especially with observations by the South site array.

Table 6.2: Comparison of the detectability of the western and eastern lobes of SS433 for various source extensions and exposure times using the North site IRFs (prod3b-v2).

Model	TS_{10hrs}^{West}	TS_{10hrs}^{East}	TS_{30hrs}^{West}	TS_{30hrs}^{East}	TS_{50hrs}^{West}	TS_{50hrs}^{East}
1	52.0	76.8	229.1	303.7	354.3	477.2
2	38.9	10.9	121.9	105.2	152.0	114.5
3	7.9	9.4	23.7	57.6	57.1	100.2
4	2.4	8.2	6.3	20.1	9.4	37.5

Table 6.3: Comparison of the detectability of the western and eastern lobes of SS433 for various source extensions and exposure times using the South site IRFs (prod3b-v2).

Model	TS_{10hrs}^{West}	TS_{10hrs}^{East}	TS_{30hrs}^{West}	TS_{30hrs}^{East}	TS_{50hrs}^{West}	TS_{50hrs}^{East}
1	137.4	184.6	738.8	821.9	886.3	1261.4
2	59.2	73.6	178.4	384.2	273.1	401.0
3	11.1	31.3	76.3	104.3	79.5	226.7
4	2.6	7.2	44.4	60.3	34.7	115.9

To test the possibility of CTA to detect a central source and its possible variability, I simulated the local region of SS433 with the diffuse background and nearby MGRO source where SS433 consists of both the aforementioned lobes and a central point source. It is assumed that the flux of this central source is approximately half that of the western lobe. Both the lobes and the central source were also assumed to have a spectral index of $\gamma = -2.0$ as observations from HAWC found the spectrum of the lobes to be consistent with this value. The lobes were given an extension that matches Model 2, see Table 6.1. Batches of 100 simulations were run using the north and south site IRFs at multiple different exposure times ranging from 30 minutes to 50 hours. The flux was calculated after every simulation and the total data was compiled into histograms for each exposure time to determine the error range of the detections. As SS433 could be viewed from both the north and south site, the results of error measurements from both sites were compared to the difference in sensitivity for a source like SS433 (see Fig. 6.3).

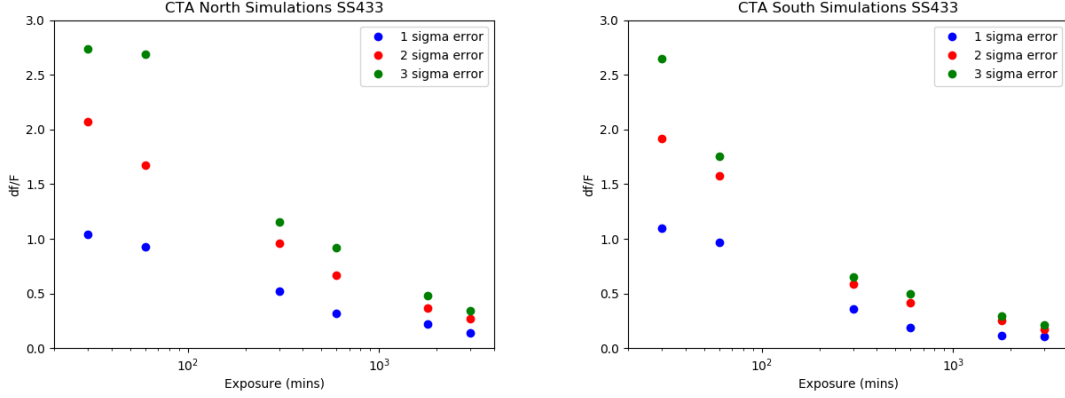


Figure 6.3: Comparison of the flux error ratio from 100 simulations at different exposure times using the North and South IRFs.

Based on these simulations, the south site will be capable of more sensitive detections, which makes sense given the increased number of telescopes in the south site design. From the south simulations, observations of 300 mins (5 hrs) or greater allows for detections with a flux error ratio of < 1 up to a range of 3σ error. However, the average TS value for observations in the 5 hrs and 10 hrs simulations were < 25 which corresponds to a $< 5\sigma$ detection. Thus a more solid detection of a possible central source in SS433 will likely require observations of > 30 hrs, which is still dramatically less than the 1017 days of HAWC observations required to detect the lobes. The detection of a central point source in SS433 would allow us to constrain the microquasar model for gamma-ray binaries as the jets are thought to be the best source for VHE emission from these sources. However, it's possible that particle acceleration at the base of the jets near the accreting compact source may also cause VHE emission.

The region surrounding SS433 does not contain many other TeV sources and could be described as an uncrowded region. Conversely sources such as the gamma-ray binary LS 5039 are located in a region with multiple nearby TeV sources (crowded region). Using the previous setup, simulations were run of a source modelled like the central SS433 source located at the position of LS 5039 to determine if the presence of other sources will affect the results. Histogram plots of the measured flux of these simulations in a uncrowded and a crowded region are shown in Fig. 6.4. It was found that results of the observed flux of the central source and the error of the observed flux were consistent for the crowded and uncrowded regions. This does, however, require an accurate model of the crowded region, which is a given in the simulation setup. Catalogue of TeV sources during first operation of CTA will be imperative to accurately model sources within these crowded regions of the sky.

The procedure used to test the effectiveness of CTA on dim transient sources like SS433 can also be used with sources of arbitrary intensity to determine what level of

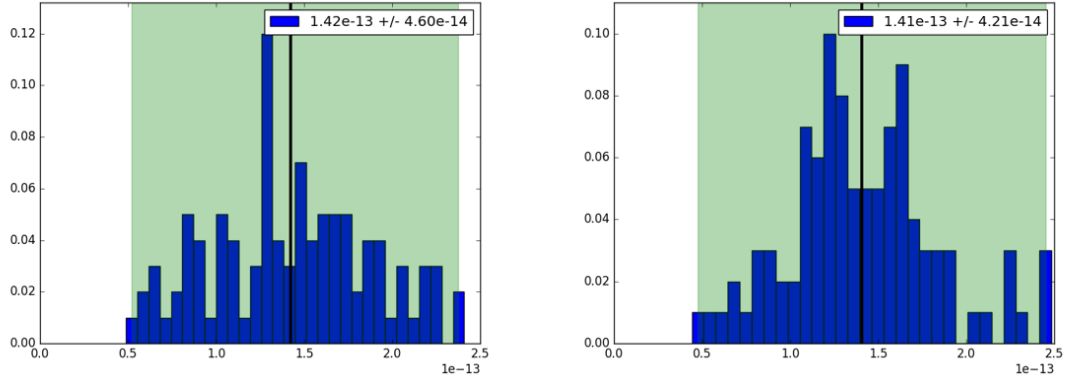


Figure 6.4: Histograms of the measured flux based on 100 CTA simulations of the central source of SS433 in a uncrowded region (left) and a crowded region (right). The top right of each plot gives the average flux and the 1σ error of the flux from the 100 simulations. The green shading represents the 3σ range of the simulations.

variability can be observed at shorter exposures. The results of simulating sources in the same position and region of SS433 with different fluxes (> 1 TeV) can be seen in Fig 6.5. Similar to the simulations of the lobes of SS433, the South IRFs produce better results with improved detections on the lobes (Table 6.3) and a lower ratio between the input flux and the 1σ error range on the central source. Based on the simulations run at different fluxes, sources with a photon flux $< 1 \times 10^{-13}$ ph/cm²/s will require observations > 10 hours in order to detect any expected variability within 25% of the source flux. However, for sources with a flux $\geq 1 \times 10^{-13}$ ph/cm²/s, CTA may be able to detect variability as low as $\sim 10\%$ using observations from 5–10 hours. At a photon flux $\geq 3 \times 10^{-12}$ ph/cm²/s the 1 sigma ratio gets as low $\sim 5\%$ for observations 0.5 – 1.0 hour long so even low variability may be detectable from relatively bright sources with very short observations.

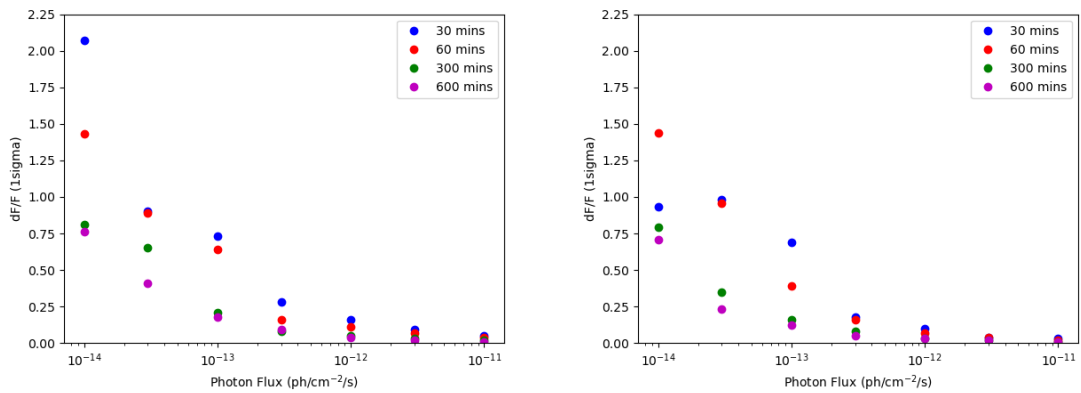


Figure 6.5: Comparison of the flux 1 sigma ratio from 100 simulations at different photon fluxes using the North and South IRFs.

6.3 Summary & Conclusions

Simulated observations of the lobes originating from the relativistic jets of SS433 provides a demonstration of what level of detection can be expected observing this source with CTA. The detection of the lobes from HAWC could not sufficiently determine the extension of the lobes so multiple extension models were tested, with all models detectable with the south site IRFs and ≥ 30 hrs observations.

Modelling a possible central point source at TeV within SS433 led to an analysis of what degree of variability CTA will be able to detect from transient galactic sources. A central source that is a factor of 2 lower in TeV intensity than the lobes will also be detectable with ≥ 30 hrs observations, while also being capable of observing and resolving variability as low as 10% of the observed flux. The ability of CTA to be able to detect such sources with such sensitivity will not only allow for improved observations of the variability in transient systems, but also detect new TeV systems that are currently not detectable. It will also potentially refine the microquasar model for gamma-ray binaries by investigating SS433 and other candidates such as Cygnus X-1 and Cygnus X-3.

Chapter 7

Conclusions and Future Projects

7.1 New Insight of PSR B1259-63

Our multiwavelength study of the 2017 periastron of PSR B1259-63 contributed to a new model that explains the origins of the GeV flares, especially on timescales of 15 mins – 3 hrs, around periastron. While previous studies modelled the GeV flares as synchrotron emission from shocked electrons, which also caused X-ray emission, this could not account for the short timescale GeV flares observed in 2017. To account for these flares, we propose a 2-zone model as a result of the shock during the periastron passage. According to this model, the enhanced X-ray and TeV emission observed during the periastron period, peaking during the interactions with the Be disc, which can be explained by synchrotron and IC emission of the strongly shocked near the apex electrons of the pulsar wind, respectively. The GeV emission is a result of IC emission of the unshocked/weakly shocked electrons and bremsstrahlung emission of these same electrons interacting with the clumps of the disc, resulting in the short 15 mins – 3 hrs flares. The luminosity of the GeV flares can be understood if we assume that the isotropic pulsar wind is redirected by the shock in an emission cone that creates a beaming effect towards the observer during flares. The results of this study were published in Chernyakova et al. (2020).

From the preliminary analysis of the multiwavelength observations of the 2021 periastron, published at Chernyakova et al. (2021), we argue that our model can explain the radio, optical, X-ray and GeV observations, despite the changes observed from the 2017 periastron. While the X-ray peaks during the disc crossings were lower than previous observations, there was a third X-ray peak observed with no corresponding peak observed in radio. Short GeV flares were observed once again, however the flare period was delayed compared to previous periastra and the peaks flare luminosity was reduced. Under our model, the assumption of lower densities in the outer Be star’s disc (compared to previous periastra) results in a larger opening

angle of the emission cone that corresponds to the lower observed luminosity of the GeV flare. The interference of clumps along the surface of shock could increase the escape time of particles within the shock which could explain the third X-ray peak observed after the crossings of the disc. This will be further investigated in a more in-depth analysis of the data that is currently ongoing in which I intend to conduct a more detailed spectral analysis and modelling of the GeV spectra and flares, similar to what I did in the study of the 2017 periastron.

This new insight into the origin of the GeV flares of PSR B1259-63 may be applicable to other gamma-ray binaries as well. In the case of most known gamma-ray binaries, the composition of the system is unknown. If application of this model can be shown to match observations or predictions for other systems, as I am interested to investigate myself, it may point to those systems also falling under the Be-pulsar model of gamma-ray binaries.

7.2 Modelling Eclipsing HMXB with Athena X-IFU

The simulated observations I have conducted with X-IFU of Vela X-1 and XSTAR models demonstrates the potential resolving power and sensitivity of Athena X-IFU and its application in observing HMXBs. Spectral modelling of Vela X-1 with Chandra HETG by Watanabe et al. (2006) required observations of 29 ks or 83 ks, depending on orbital phase, in order to adequately resolve the spectra. My initial simulations of X-IFU, with exposure times of 10 ks, resulted in highly resolved spectra at all orbital phases tested. This includes the eclipse phase of the orbit where the observed flux drops by two orders of magnitude. The iron $K\alpha$ line at 6.396 keV was used to test the sensitivity of X-IFU on observations shorter than 10 ks. Fitting the simulated observations of the iron $K\alpha$ with found that even observations as short as 2 – 5 ks could still resolve fine spectral details such as emission lines at all orbital phases, including the eclipse phase. This suggests X-IFU will be capable of resolving variability from HMXBs on the scale of several ks as observed in Vela X-1 by Odaka et al. (2013).

Emission lines from XSTAR models were used to calculate and model the gradual change in emission line profiles over the course of an eclipse. Making multiple simulated 5 ks observations of this modelled eclipse with X-IFU indicates that X-IFU will be able to track the gradual change in the spectral profile of eclipsing HMXBs like Vela X-1. This could provide a new way to map the emission regions of HMXBs as the sensitivity of X-IFU will allow for observations that can resolve multiple phases of the eclipse. The morphology of photoionization and emission regions such

as accretion discs, accretion wakes, photoionization wakes and Strömgren spheres could be determined by multiple observations of several ks to observe the gradual change in the X-ray spectrum during an orbit. I intend to revisit the XSTAR models used for eclipse modelling and to write up the findings for publication in the near future.

With the experience I have gained using SIXTE and SIMPUT to simulate X-IFU observations, I would be interested in continuing to work on the study of what new insights may be possible in HMXBs and other transient X-ray sources. Particularly other eclipsing HMXB with a different accretion system to Vela X-1, such as Cen X-3, which is an eclipsing HMXB with a lower period than Vela X-1 and evidence of an accretion disc.

7.3 Demonstration of the Sensitivity of CTA

My simulations of CTA observations of SS433 provides a demonstration of the high sensitivity of which CTA will be capable. This has contributed to the larger study of CTA's use on Galactic transients by the CTA consortium. Persistent observations of SS433 by HAWC required 1017 days to detect TeV emission from the lobes with a confidence of 5.4σ (Abeysekara et al. 2018). By comparison, CTA South site configuration was capable of achieving a $TS > 25$ (confidence $> 5\sigma$) with 30-50 hrs simulated observations for SS433 lobes modelled with high extension values (West=0.26, East=0.1875). Lower extension models for the lobes resulted in high confidence detections with observations as low as 10 hrs. This suggests CTA will be able to make detections that currently take years in a matter of days and longer observations may be used to resolve any variability from the lobes at TeV energies.

The potential sensitivity of CTA was further demonstrated by simulating a possible central emission source in SS433. While this was not observed by HAWC, this is a possible component of microquasars as a model for gamma-ray binaries. As the flux of such a source is unknown, a range of arbitrary fluxes were modelled. This range of fluxes was also used to investigate the level of variation CTA may resolve from transient sources at exposures from 30 mins – 10 hrs. CTA shows promise to make detections of a source with a flux that has a factor of 2 lower than the lobes. This is achieved while being able to resolve variability of $\sim 10\%$ of the observed flux with a 1σ confidence with observations as short as 10 hrs. This suggests that even currently undetected TeV sources will be detectable with observations on a daily scale and possibly shorter depending on the intensity of the source.

As the CTA consortium study is still ongoing, I intend to continue with my contributions simulating transient sources with CTA, including recent work on the CTA Galactic Plane Survey. However, as CTA is due to begin operation in 2025,

I am eager to be able to work on observational data from CTA. In particular on gamma-ray binaries and microquasars such as PSR 1259-63 for the 2027 periastron and SS433 to compare with my own simulation study.

Appendix A

Using XSTAR

In Ch. 5, I used XSTAR models as a part of my eclipse modelling for X-IFU simulations. A large part of the challenge I experienced during this project was learning how to use XSTAR. While it's extremely simple to run, additional arguments when running the program and the format of the results is not apparent for a first time user. This issue is somewhat compounded by the XSTAR manual which is available online, but is sparse on details in some sections and not up to date in others. I wish to provide a few tips with using XSTAR for first time users to hopefully make the learning experience a little bit faster than my own.

First off, an important point for running the program. By default if you run XSTAR with no arguments, it will output 4 files containing the spectral data, continuum, emission line luminosity and ionic abundances. Depending on your need of XSTAR, this may be all you require. However, if you require more detailed information from the output, such as the complete line population and radial emissivity as I did, an additional argument “lwrite=1” is required. The name of this hidden parameter may change depending on the latest version of XSTAR.

It's also important to note how the parameters of an XSTAR output vary with the input parameters. As briefly described in Ch. 5, the inner radius of the XSTAR model is defined based on the ionization parameter calculation (rearranged in Eq. A.1, same as shown in Ch. 5).

$$R_{inner} = \sqrt{L/n\xi} \quad (\text{A.1})$$

Therefore the luminosity, density and ionization parameter define the inner radius of the modelled region. The outer radius and number of distinct shells of the modelled region is a bit more complicated. These values are somewhat defined by the same parameters for the inner radius such that the luminosity, density and ionization parameter could be changed and still result in the same inner radius but different outer radius. However, there are two input parameters that each have a noticeable

effect on the output outer radius and number of shells, which is the column density and temperature. The size of the outer radius increases proportionally while the number of shells increase inversely with the temperature. It is essential to be aware of and consider how the XSTAR output varies when revising the input parameters of your model.

Final thing I want to discuss when it comes to using XSTAR is the units and scaling of input and output parameters. It's important to note that input parameters such as the temperature, luminosity and ionization parameter have scaled units. For example the temperature input is 10^4 K, luminosity 10^{38} erg and the ionization parameter is $\log \xi$ (the unit for ξ is $\text{erg} \cdot \text{cm} / \text{s}$). Similarly, columns in the output files may have scaled units that need to be accounted for when using the output values. This scaling is not always listed in the header of the column but documentation in the manual should mention any relevant unit scaling. In particular, any columns for luminosity or specific luminosity ($\text{erg} / \text{s} / \text{erg}$) has a scaling of 10^{38} . The issue of this scaling being miss in some columns may have been addressed in recent software updates.

These were some of the quirks of using XSTAR that I believe helps knowing in advance to use the software effectively. Like with most programs, you can learn a lot of this through trial and error as I did, but it's always easier if you can avoid a few of the error steps to begin with.

Bibliography

- Abdo, A. A., Ackermann, M., Ajello, M., et al. 2011, *The Astrophysical Journal*, 736, L11
- Abdo, A. A., Ackermann, M., Ajello, M., et al. 2009, *Science* (80-.), 326, 1512
- Abdollahi, S., Acero, F., Ackermann, M., et al. 2020, *ApJS*, 247, 33
- Abeysekara, A. U., Albert, A., Alfaro, R., et al. 2018, *Nature*, 562, 82
- Abramowski, A., Acero, F., Aharonian, F., et al. 2015, *Mon. Not. R. Astron. Soc.*, 446, 1163
- Abramowski, A., Acero, F., Aharonian, F., et al. 2013, *Astron. Astrophys.*, 551, A94
- Aharonian, F. 2005, *Science*, 309, 746–749
- Aharonian, F. A. 2004, Very high energy cosmic gamma radiation : a crucial window on the extreme Universe
- Aharonian, F. A., Akhperjanian, A. G., Bazer-Bachi, A. R., et al. 2007, *A&A*, 469, L1
- Aharonian, F. A. & Atoyan, A. M. 1981, *Ap&SS*, 79, 321
- Aharonian, F. A., Kelner, S. R., & Prosekin, A. Y. 2010, *Phys. Rev. D*, 82, 043002
- Aharonian, F., Akhperjanian, A. G., Aye, K.-M., et al. 2005, *A&A*, 442, 1
- Albert, J. 2006, *Science*, 312, 1771–1773
- Amato, R., Grinberg, V., Hell, N., et al. 2021, *Astronomy & Astrophysics*, 648, A105
- Atwood, W., Albert, A., Baldini, L., et al. 2013, Pass 8: Toward the Full Realization of the Fermi-LAT Scientific Potential
- Atwood, W. B., Abdo, A. A., Ackermann, M., et al. 2009, *Astrophys. J.*, 697, 1071

- Bailer-Jones, C. A. L., Rybizki, J., Fouesneau, M., Mantelet, G., & Andrae, R. 2018, *The Astronomical Journal*, 156, 58
- Ball, L., Melatos, A., Johnston, S., & Skjæ Raasen, O. 1999, *ApJ*, 514, L39
- Baring, M. G., Ellison, D. C., Reynolds, S. P., Grenier, I. A., & Goret, P. 1999, *ApJ*, 513, 311
- Bell, A. R. 1978, *MNRAS*, 182, 147
- Bernlöhr, K. 2009, *AIP Conf. Proc.*, 1085, 874
- Bertschinger, E. 1987, *ApJ*, 316, 489
- Bildsten, L., Chakrabarty, D., Chiu, J., et al. 1997, *ApJS*, 113, 367
- Blandford, R. & Eichler, D. 1987, *Phys. Rep.*, 154, 1
- Blumenthal, G. R. & Gould, R. J. 1970, *Rev. Mod. Phys.*, 42, 237
- Bordas, P., Yang, R., Kafexhiu, E., & Aharonian, F. 2015, *Astrophys. J. Lett.*, 807, L8
- Bruel, P., Burnett, T. H., Digel, S. W., et al. 2018, *Fermi-LAT improved Pass 8 event selection*
- Bykov, A. M., Gladilin, P. E., & Osipov, S. M. 2013, *MNRAS*, 429, 2755
- Caliandro, G. A., Cheung, C. C., Li, J., et al. 2015, *The Astrophysical Journal*, 811, 68
- Carciofi, A. C. 2011, in *Active OB Stars: Structure, Evolution, Mass Loss, and Critical Limits*, ed. C. Neiner, G. Wade, G. Meynet, & G. Peters, Vol. 272, 325–336
- Carroll, B. W. & Ostlie, D. A. 2007, *An introduction to modern astrophysics*; 2nd ed. (San Francisco, CA: Addison-Wesley)
- Castor, J. I., Abbott, D. C., & Klein, R. I. 1975, *ApJ*, 195, 157
- Chaty, S. 2007, in *Frontier Objects in Astrophysics and Particle Physics*, ed. F. Giovannelli & G. Mannocchi, 329
- Chaty, S. 2011, *Nature*, formation and evolution of High Mass X-ray Binaries
- Chen, A. M., Takata, J., Yi, S. X., Yu, Y. W., & Cheng, K. S. 2019, *A&A*, 627, A87

- Chernyakova, M., Abdo, A. A., Neronov, A., et al. 2014, *Monthly Notices of the Royal Astronomical Society*, 439, 432–445
- Chernyakova, M. & Malyshev, D. 2020, *Gamma-ray binaries*
- Chernyakova, M., Malyshev, D., Mc Keague, S., et al. 2020, *Monthly Notices of the Royal Astronomical Society*, 497, 648–655
- Chernyakova, M., Malyshev, D., van Soelen, B., et al. 2021, Multi-wavelength properties of the 2021 periastron passage of PSR B1259-63
- Chernyakova, M., Neronov, A., van Soelen, B., et al. 2015, *Mon. Not. R. Astron. Soc.*, 454, 1358
- Chernyakova, M., Uchiyama, Y., Takahashi, T., et al. 2009, *AIP Conference Proceedings*
- Collaboration, T. F. L. 2012, *Science*, 335, 189–193
- Collon, M. J., Vacanti, G., Barrière, N. M., et al. 2019, in *International Conference on Space Optics — ICSO 2018*, ed. Z. Sodnik, N. Karafolas, & B. Cugny, Vol. 11180, *International Society for Optics and Photonics (SPIE)*, 789 – 799
- Corbet, R. H. D. 1986, *MNRAS*, 220, 1047
- Corbet, R. H. D., Cheung, C. C., Kerr, M., et al. 2011, *The Astronomer’s Telegram*, 3221, 1
- Corbet, R. H. D., Chomiuk, L., Coe, M. J., et al. 2019, *The Astrophysical Journal*, 884, 93
- Corbet, R. H. D., Chomiuk, L., Coe, M. J., et al. 2016, *Astrophys. J.*, 829, 105
- Dauser, T., Falkner, S., Lorenz, M., et al. 2019, *A&A*, 630, A66
- Di Mauro, M. & Donato, F. 2015, *Phys. Rev. D*, 91, 123001
- Dorman, B., Arnaud, K. A., & Gordon, C. A. 2003, in *Am. Astron. Soc. HEAD Meet. #7*, id.22.10, 22.10
- Doroshenko, V., Santangelo, A., Nakahira, S., et al. 2013, *A&A*, 554, A37
- Dovciak, M., Matt, G., Bianchi, S., et al. 2013, *The Hot and Energetic Universe: The close environments of supermassive black holes*
- Dubner, G. M., Holdaway, M., Goss, W. M., & Mirabel, I. F. 1998, *AJ*, 116, 1842

- Dubus, G. 2013, *The Astronomy and Astrophysics Review*, 21
- Dubus, G., Guillard, N., Petrucci, P.-O., & Martin, P. 2017, *Astronomy & Astrophysics*, 608, A59
- Eikenberry, S. S., Cameron, P. B., Fierce, B. W., et al. 2001, *ApJ*, 561, 1027
- El Mellah, I., Sundqvist, J. O., & Keppens, R. 2019, *Astronomy & Astrophysics*, 622, L3
- Fermi Science Support Development Team. 2019, *Fermitools: Fermi Science Tools*
- Forman, W., Jones, C., Tananbaum, H., et al. 1973, *ApJ*, 182, L103
- Fransson, C. & Fabian, A. C. 1980, *A&A*, 87, 102
- Fujita, Y., Nagai, H., Akahori, T., Kawachi, A., & Okazaki, A. T. 2020, *Publications of the Astronomical Society of Japan*, 72
- Fürst, F., Kreykenbohm, I., Pottschmidt, K., et al. 2010, *Astron. Astrophys.*, 519, A37
- Gies, D. R., Huang, W., & McSwain, M. V. 2002, *ApJ*, 578, L67
- Giménez-García, A., Shenar, T., Torrejón, J. M., et al. 2016, *A&A*, 591, A26
- Grimm, H.-J., Gilfanov, M., & Sunyaev, R. 2003, *Astron. Astrophys.*, 391, 923
- Grinberg, V., Hell, N., El Mellah, I., et al. 2017, *A&A*, 608, A143
- H. E. S. S. Collaboration, Abdalla, H., Adam, R., et al. 2020, *A&A*, 633, A102
- Heinz, S. & Sunyaev, R. 2002, *A&A*, 390, 751
- Hillwig, T. C., Gies, D. R., Huang, W., et al. 2004, *ApJ*, 615, 422
- Hiltner, W. A., Werner, J., & Osmer, P. 1972, *ApJ*, 175, L19
- Houck, J. C. & Denicola, L. A. 2000, in *Astronomical Society of the Pacific Conference Series*, Vol. 216, *Astronomical Data Analysis Software and Systems IX*, ed. N. Manset, C. Veillet, & D. Crabtree, 591
- Irwin, K. D., Hilton, G. C., Wollman, D. A., & Martinis, J. M. 1996, *Appl. Phys. Lett.*, 69, 1945
- Johnson, T. J., Wood, K. S., Kerr, M., et al. 2018, *Astrophys. J.*, 863, 27
- Johnston, S., Manchester, R., Lyne, A., et al. 1992, *Astrophys. J. Lett.*, 387, L37

- Kaastra, J., Finoguenov, A., Nicastro, F., et al. 2013, The Hot and Energetic Universe: The missing baryons and the warm-hot intergalactic medium
- Kallman, T. & Bautista, M. 2001, The Astrophysical Journal Supplement Series, 133, 221
- Kaspi, V. M., Tavani, M., Nagase, F., et al. 1995, ApJ, 453, 424
- Katarzyński, K., Ghisellini, G., Tavecchio, F., Gracia, J., & Maraschi, L. 2006, Mon. Not. R. Astron. Soc. Lett., 368, L52
- Khangulyan, D., Aharonian, F., & Bosch-Ramon, V. 2008, MNRAS, 383, 467
- Khangulyan, D., Aharonian, F. A., Bogovalov, S. V., & Ribó, M. 2011, ApJ, 742, 98
- Khangulyan, D., Aharonian, F. A., & Kelner, S. R. 2014, ApJ, 783, 100
- Kirk, J. G., Ball, L., & Skjæraasen, O. 1999, Astroparticle Physics, 10, 31
- Kitamoto, S., Enoto, T., Safi-Harb, S., et al. 2014, ASTRO-H White Paper - Accreting Pulsars, Magnetars, and Related Sources
- Knödseder, J., Mayer, M., Deil, C., et al. 2016, Astron. Astrophys., 593, A1
- Kretschmar, P., Fürst, F., Sidoli, L., et al. 2019, New Astronomy Reviews, 86, 101546
- Kudritzki, R.-P. & Puls, J. 2000, ARA&A, 38, 613
- Lamers, H. J. G. L. M. & Cassinelli, J. P. 1999, Line driven winds (Cambridge University Press), 187–254
- Lucy, L. B. & Solomon, P. M. 1970, ApJ, 159, 879
- Lyne, A. G., Stappers, B. W., Keith, M. J., et al. 2015, Mon. Not. R. Astron. Soc., 451, 581
- Maier, G., Arrabito, L., Bernlöhr, K., et al. 2019, Performance of the Cherenkov Telescope Array
- Malacaria, C., Mihara, T., Santangelo, A., et al. 2016, A&A, 588, A100
- Malyshev, D., Zdziarski, A. A., & Chernyakova, M. 2013, Mon. Not. R. Astron. Soc., 434, 2380
- Malzac, J. & Belmont, R. 2008, in VII Microquasar Work. Microquasars Beyond, 007

- Manousakis, A. 2011, PhD thesis, iD: unige:18752
- Manousakis, A. & Walter, R. 2015, *Astronomy & Astrophysics*, 575, A58
- Margon, B. & Anderson, S. F. 1989, *ApJ*, 347, 448
- Massa, D. 1975, *PASP*, 87, 777
- Mazin, D. 2019, *The Cherenkov Telescope Array*
- McClintock, J. E., Rappaport, S., Joss, P. C., et al. 1976, *ApJ*, 206, L99
- Meegan, C., Lichti, G., Bhat, P. N., et al. 2009, *Astrophys. J.*, 702, 791
- Meidinger, N., Eder, J., Eraerds, T., et al. 2017, *The Wide Field Imager Instrument for Athena*
- Melatos, A., Johnston, S., & Melrose, D. B. 1995, *MNRAS*, 275, 381
- Melrose, D. B. & Pope, M. H. 1993, *Proceedings of the Astronomical Society of Australia*, 10, 222
- Mendoza, C., Bautista, M. A., Deprince, J., et al. 2020, *The XSTAR Atomic Database*
- Mirabal, N. 2018, FSSC: Fermi Data ” Data analysis ” analysis threads ” source model definitions for gtlike
- Mirabel, I. F. & Rodríguez, L. F. 1998, *Nature*, 392, 673
- Mirabel, I. F. & Rodriguez, L. F. 1999, *Annu. Rev. Astron. Astrophys.*, 37, 409
- Moldón, J., Johnston, S., Ribó, M., Paredes, J. M., & Deller, A. T. 2011, *ApJ*, 732, L10
- Nandra, K., Barret, D., Barcons, X., et al. 2013, *The Hot and Energetic Universe: A White Paper presenting the science theme motivating the Athena+ mission*
- Odaka, H., Khangulyan, D., Tanaka, Y. T., et al. 2013, *Astrophys. J.*, 767, 1
- Okazaki, A. T. & Negueruela, I. 2001, *A&A*, 377, 161
- Pajot, F., Barret, D., Lam-Trong, T., et al. 2018, *J. Low Temp. Phys.*, 193, 901
- Porter, J. M. & Rivinius, T. 2003, *PASP*, 115, 1153
- Quaintrell, H., Norton, A. J., Ash, T. D. C., et al. 2003, *A&A*, 401, 313
- Quast, M., Langer, N., & Tauris, T. M. 2019, *A&A*, 628, A19

- Rasul, K., Chadwick, P. M., Graham, J. A., & Brown, A. M. 2019, *Monthly Notices of the Royal Astronomical Society*, 485, 2970
- Reig, P. 2011, *Ap&SS*, 332, 1
- Romoli, C., Bordas, P., Mariaud, C., et al. 2015, in *Proc. Sci.*, Vol. 30-July-20
- Rybicki, G. B. & Lightman, A. P. 1986, *Radiative Processes in Astrophysics*
- Savonije, G. J. 1978, *A&A*, 62, 317
- Seward, F., Grindlay, J., Seaquist, E., & Gilmore, W. 1980, *Nature*, 287, 806
- Shakura, N. I. & Sunyaev, R. A. 1973, *A&A*, 500, 33
- Shannon, R. M., Johnston, S., & Manchester, R. N. 2014, *Mon. Not. R. Astron. Soc.*, 437, 3255
- Shipman, H. L. 1979, *ApJ*, 228, 240
- Sparavigna, A. C. & Marazzato, R. 2010, *Observing stellar bow shocks*
- Sun, X.-N., Yang, R.-Z., Liu, B., Xi, S.-Q., & Wang, X.-Y. 2019, *Astronomy & Astrophysics*, 626, A113
- Tam, P.-H. T., He, X., Pal, P. S., & Cui, Y. 2018, *Astrophys. J.*, 862, 165
- Tarter, C. B., Tucker, W. H., & Salpeter, E. E. 1969, *ApJ*, 156, 943
- The CTA Consortium. 2019, *Science with the Cherenkov Telescope Array (WORLD SCIENTIFIC)*, 364
- van Loon, J. T., Kaper, L., & Hammerschlag-Hensberge, G. 2001, *A&A*, 375, 498
- van Soelen, B., Meintjes, P. J., Odendaal, A., & Townsend, L. J. 2012, *MNRAS*, 426, 3135
- Vieu, T., Gabici, S., & Tatischeff, V. 2020, *arXiv e-prints*, arXiv:2003.03411
- Völk, H. J. & Bernlöhr, K. 2009, *Experimental Astronomy*, 25, 173
- Watanabe, S., Sako, M., Ishida, M., et al. 2006, *Astrophys. J.*, 651, 421
- Wille, E., Bavdaz, M., Oosterbroek, T., et al. 2015, in *Optics for EUV, X-Ray, and Gamma-Ray Astronomy VII*, ed. S. L. O'Dell & G. Pareschi, Vol. 9603, *International Society for Optics and Photonics (SPIE)*, 149 – 154
- Wilson, W. E., Ferris, R. H., Axtens, P., et al. 2011, *MNRAS*, 416, 832

- Xing, Y., Wang, Z., Zhang, X., Chen, Y., & Jithesh, V. 2019, *The Astrophysical Journal*, 872, 25
- Zabalza, V. 2015, *naima*: a Python package for inference of relativistic particle energy distributions from observed nonthermal spectra
- Zdziarski, A. A., Malzac, J., & Bednarek, W. 2009, *Monthly Notices of the Royal Astronomical Society: Letters*, 394, L41–L45